Studies on Key Reactions in Iron-Making Process Mediated by Oxalic Acid

ファチャダ, サンタワジャ

Studies on Key Reactions in Iron-Making Process Mediated by Oxalic Acid

by

Phatchada Santawaja

Department of Applied Science for Electronics and Materials

Interdisciplinary Graduate School of Engineering Sciences

Kyushu University, Japan

2020

ACKNOWLEDGEMENTS

CONTENTS

CONTENTS

CHAPTER 5

PROOF OF IRON-MAKING PROCESS MEDIATED BY OXALIC ACID

CHAPTER 6

GENERAL CONCLUSIONS AND FUTURE CHALLENGES

APPENDIX

DISSERTATION SUMMARY

The iron- and steel-making is considered as one of the most important processes in industries because iron and steel are essential materials in modern society. Nevertheless, it is also recognized as one of the most energy-intensive process and CO_2 emitter. CO_2 is heavily generated from the conventional blast furnace (BF) that is a reactor of primary step in the iron-making process. The use of coke as the fuel and reductant in BF is the main cause of the huge CO_2 emission and high energy consumption. To cope with this environmental problem, there have been many efforts to technically improve energy efficiency of BF, and alternative processes such as direct reduction (DR) and smelting reduction have been introduced to the iron-making. However, there have been still no significant decreases of CO_2 emission and energy consumption in this industry due to its reliance on the fossil-fuel-based high temperature processes.

Therefore, the primary aim of this study is to propose a more sustainable iron-making process which has a potential to be free from fossil fuel and high temperature by employing unique chemical properties of oxalic acid including its affinity for complexation with iron ions. The proposed iron-making process, called iron-making process mediated by oxalic acid, consists of four key reactions: (1) dissolution of iron oxide with oxalic acid to prepare an aqueous solution of iron(III) oxalate, (2) photochemical reduction of iron(III) oxalate to iron(II) oxalate that is precipitated and recovered as solid from the solution, (3) pyrolytic reduction of iron(II) oxalate to produce metallic iron, and (4) synthesis of oxalic acid from CO_2 generated in the reactions of (1)-(3). The first three steps of the proposed process do not require a high temperature while enable the production of quality iron with chemical reaction selectivities caused by oxalic acid. When all CO_2 generated during the iron-making are used for the synthesis of oxalic acid at the last step, overall reaction of the process can be stoichiometrically

described by $Fe_2O_3 + 3H_2 \rightarrow 2Fe + 3H_2O$, which is carbon free. In this dissertation study, the first three steps of the process have been experimentally investigated to demonstrate the proposed iron-making method and its performance as an iron-making process.

This thesis consists of six chapters. Brief summaries of each chapter are presented in the followings;

Chapter 1 of this thesis introduces the background, motivations, and objectives of this work. The current status of industrial iron-making processes including both conventional and alternative iron-making processes is briefly reviewed. Then, the concept of iron-making process mediated by oxalic acid is explained in detail.

Chapter 2 shows the study on the dissolution of iron oxides with oxalic acid, which is the first step of the proposed iron-making process. To be an iron-making method, reactions in the proposed method are required to occur at high reaction rates. The iron dissolution step, in particular, is required to prepare a high concentration of the iron oxalate aqueous solution. In this study, therefore, the dissolution of iron oxides highly loaded in the oxalic acid aqueous solution (up to 1.3 mol-Fe/L) is investigated. The dissolution is carried out in the absence of light and with no addition of other chemical reagents. Factors affecting the dissolution, such as iron oxide types, temperature, and the concentrations of oxalic acid and iron oxides, are varied in order to optimize the dissolution conditions and reveal chemistry of the dissolution. The results show that the rate of dissolution is affected by the type of iron oxides. Fe_3O_4 shows a distinguished fast dissolution due to the facile and fast release of catalytic iron(II) oxalate, followed by α-Fe_2O_3 and FeOOH. Due to high acidity of the solution and high dissolution temperature, non-reductive dissolution is suggested to be a predominant dissolution mechanism, which is demonstrated by the presence of dissolved Fe^{3+} as major iron species in the leachate. Increasing temperature not only improves the dissolution efficiency but also

enhances the rate of oxalic acid dissociation. The dissolution temperature around 90 °C is suggested to be an optimum temperature to provide the fast Fe dissolution without boiling the solution. More importantly, the results reveal that iron concentration in the prepared iron oxalate solution can be well above 0.5 mol/L regardless of the iron oxide types. Furthermore, a required minimum ratio of oxalic acid to iron (OxA/Fe) to completely dissolve the loaded iron oxide at 92 °C is found to be 1.82.

Chapter 3 reports the study on the second step of the iron-making method, which is the photochemical reduction of iron (III) oxalate to recover iron as a solid form of iron(II) oxalate dihydrate. The results of experiments using simulated sunlight show that the rate of conversion is approximately proportional to the light intensity (photon flux density: PFD), whereas sources of iron in iron(III) oxalate solution and the depth of solution do not show significant influence on the rate of conversion. When the LED lights are used, it is confirmed that light in the wavelength of 365-550 nm can induce the photochemical reduction. Moreover, it reveals that, apart from the light intensity, the wavelength region of light also plays an important role in the rate of reaction: light near UV-region has a high impact on the conversion rate. Natural sunlight also reduces the iron(III) oxalate aqueous solution to iron(II) oxalate dihydrate precipitate, but it requires more time to complete the reaction due to the weather condition dependency. The iron(II) oxalate precipitates obtained from experiments under all conditions are indexed to be pure $FeC_2O_4 \cdot 2H_2O$, but they are slightly different from each other in terms of their structures, crystallinities, and crystal sizes, which probably results from the rate of conversion.

Chapter 4 describes the pyrolytic reduction of the iron(II) oxalate dihydrate to produce metallic iron, which is the last step of the proposed iron-making. Various atmospheres, namely, N_2, 50%-H_2/N_2, 50%-CO_2/N_2, 50%-CO/N_2, and 50%-air/N_2, are used to investigate the thermal behaviors of iron(II) oxalate dihydrate. The results show that the gas composition influences

the thermal decomposition of $FeC_2O_4 \cdot 2H_2O$. Under $50\%H_2/N_2$ atmosphere, the metallic iron forms from $FeC_2O_4 \cdot 2H_2O$ even below 500 °C. Moreover, the iron(II) oxalate dihydrate precipitates obtained from the previous dissolution and photochemical reduction steps are used as the precursor for metallic iron, and the results prove that all precipitates can be converted to α-Fe under this condition.

In chapter 5, the findings in chapters 2-4 are applied to the proof of iron-making from iron feedstocks containing other elements. The demonstration experiment of the proposed process achieves satisfactory results: three different iron sources were successfully converted into metallic iron at a low processing temperature of 500 °C. The conditions of iron dissolution step and the presence of impurity elements in the feedstock primarily determine the overall yield and purity of the produced iron. By using the proposed process, a major portion of impurities, such as Al, Si, P, and S were removed. Therefore, a recovery of metallic iron with high purity is achievable. On the other hand, the presence of Ca, Mg and Mn, affects the process performance as well as the quality of iron product by the consumption of oxalic acid during the dissolution.

Chapter 6 summarizes the findings described in the preceding chapters, and the future challenges of this process are also described.

CHAPTER 1

General Introduction

1.1 Current status of iron-making process

1.1.1 Conventional iron-making process

Iron and steel are materials indispensable to modern society which have been widely used in various industries or even in households. Consequently, global crude steel production rose by 3.9% from 1.71 Gt in 2018 to 1.78 Gt in 2019, and continued growth is projected in the years to come. [1] The iron and steel industry is, however, one of the most energy-intensive industrial sectors and also the industries affecting the global environment. The major by-product from iron and steel production is CO_2, which is renowned as the cause of global warming issue. [2-7] According to the International Energy Agency (IEA) report in 2019, the CO_2 emissions from this industry amounted to approximately 2.0 Gt, accounting for about 24% of the total amount emitted directly from industries [8], as presented in Figure 1-1.
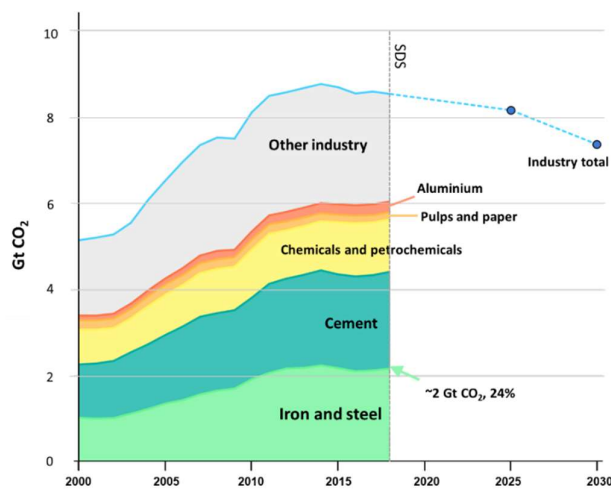
Figure 1-1. The IEA report of direct CO_2 emission in 2019 (*adapted from ref [8]*)

CHAPTER 1

The majority of generated CO_2 in the iron and steel industry comes from the iron-making process which serves as the primary step for producing the steel. The conventional iron making process generally employs a blast furnace (BF) (**Figure 1-2**).
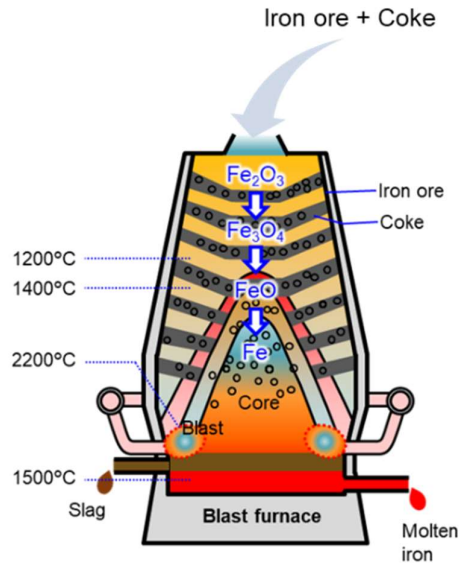
Figure 1-2. Schematic of a blast furnace (BF)

The BF is a sophisticated technology that is used to produce a massive amount of iron continuously from iron ores by using a huge shaft furnace. CO_2 emissions are unavoidable during this process as the technology relies on fossil fuels, coal in particular, for reducing iron oxides in the iron ore and providing heat to maintain a furnace temperature of up to 2,200 °C. [6,9] Although the BF used in Japanese industries, the third biggest steelmaking country in the world [10], are renowned for being one of the world-leading clean technologies, CO_2 emission from iron and steel industry accounts for nearly 15% of the total domestic CO_2 emission. [11]

Among all energy services and industrial processes, the iron and steel industry, which inevitably relies on fossil fuels, is considered to be in the category of "difficult-to-eliminate emissions". [7] Therefore, the development of alternative iron-making technology is thus vital to the global goal of building a sustainable society.

1.1.2 Alternatives iron-making process

According to the environmental concern, nowadays, extensive R&D efforts have been invested in alternative approaches to iron-making from the iron ore. They are largely classified into two types: direct reduction (DR) and smelting reduction processes. [2-6,9,12-14] A comparison of some current iron making technologies are summarized in **Table 1-1.** [6]

Table 1-1. A comparison of some current iron making technologies. *(Adapted from Ref. 6)*

Iron making technologies	Reduction agent and energy source			Form of iron that can be used				Required O$_2$	Required coal gasification	Commercialization status
	Non-coking coal	coke	NG	Sinter	Pellet	Lump ore	Fine ore			
Blast furnace		X		X	X					Commercial
COREX process	X			X	X	X		X		Commercial with very low adoption rate[*]
FINEX process	X						X	X		
Tecnored	X				X	X				Pilot[$]
ITmk3	X				X	X				Demonstra-tion[#]
Coal-based MIDREX process	X				X	X		X	X	

Note: *: The technology is proven and is being commercialized but has a very small market share.
$: The technology is being tested at an industrial-scale pilot plant.
#:The technology is being demonstrated and tested at the industrial scale in more than one plant but has not yet been commercially proven.

In DR process, the iron oxides in iron ore are reduced by using reducing gas (H$_2$ and CO) produced from natural gas or coal in reactors such as shaft furnaces and fluidized bed reactors. The reduction occurs at temperatures below a melting point of iron, producing so-called direct reduced iron (DRI) or sponge iron. The reduction of iron ore, in case that iron oxide in ore presents as Fe$_2$O$_3$, occurs in three steps in sequent : Fe$_2$O$_3$ $\rightarrow$ Fe$_3$O$_4$ $\rightarrow$ FeO $\rightarrow$ Fe. The required temperature of this process is typically above 900℃ depending on the reduction condition. Although the operating temperature for producing DRI is lower than that of produced hot metal from BF process, it still requires high temperature causing a huge energy

consumption which is another concerning issue of iron-steel industry. The example of commercial direct reduction process is a coal-based MIDREX process which purges natural gases to convert iron oxide into DRI, and the standard process flow of MIDREX process is shown in **Figure 1-3**. On the other hand, smelting reduction produces molten iron like a BF using a two-step process consisting of the solid-state reduction, followed by smelting reduction. The developed technologies based on the smelting reduction, e.g., COREX, FINEX, ITmk3 and Hismelt, have been commercialized or are under demonstration. [3,6,15]
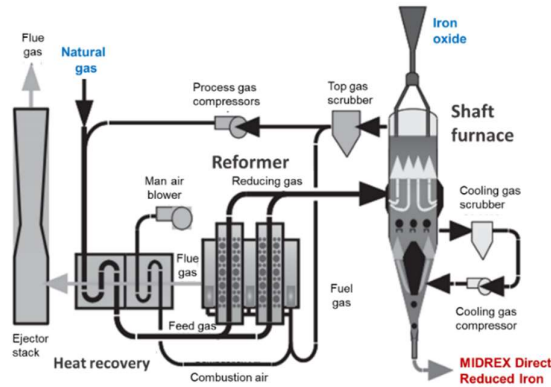
Figure 1-3. A standard process flow of MIDREX process *(Adapted from ref. 5)*

The main advantages of these alternative iron-making processes over BF include the lack of a need for coke, lower CO_2 emissions, and lower capital/operation costs. However, they do not address the fundamental problems posed by the use of a BF because of their reliance on fossil fuels and harsh operating conditions. From this viewpoint, there are limited studies on potential sustainable iron-making methods. For example, Akiyama et al. reported a low temperature iron-making method using ammonia as the reducing agent. [16,17] Pursuing better process design to achieve sustainability for large-scale and complex iron-making is acutely challenging, but, if successful, the shift to a new system will have a hugely positive and global impact on the environment.

1.2 Motivations and objectives of this study

Due to the environmental impacts, a large amount of CO_2 emission, and the biggest energy consumption in the steelmaking brought by blast furnace (BF) which is the conventional iron-making process, this method has been improved by various methods to address the problems. Besides, some alternative approaches have been introduced like direct reduction (DR) and smelting reduction processes, as mentioned previously. Nevertheless, there has been still no significant decrease in the emission since most of the alternative iron-making technologies still rely on fossil fuel and require a high operating temperature.

Therefore, the aims of this study is to propose a novel iron-making process by using oxalic acid as a medium. The process applies the unique chemical properties of oxalic acid and its affinity for complexation with iron, which could allow this process to be the fossil-fuel-free production with high-purity iron at low temperatures, and have potential to be no CO_2 emission. The proposed iron-making process comprises four processes namely; 1) the dissolution of iron oxide with oxalic acid to prepare an aqueous solution of iron(III) oxalate; (2) the photochemical reduction of iron(III) oxalate to Fe(II) oxalate precipitate; (3) the pyrolytic reduction of iron(II) oxalate to produce the metallic-iron; and (4) oxalic acid synthesis from the generated CO_2. The concept of the proposed process and details in each reaction will be described in the following sections. This dissertation highlights the production of the metallic iron by using the proposed iron-making process and exclusively focuses on the first three steps of the proposed: dissolution of iron oxides with oxalic acid (Chapter 1), photochemical reduction (Chapter 2) and pyrolytic reduction (Chapter3) in order to determine the parameters affecting the process performance. Thus, oxalic acid synthesis from the generated CO_2 is outside the scope of this study. Moreover, to reveal the potential of the proposed process, the lab-scale demonstrations by using three different types of iron sources are also investigated (Chapter 5).

CHAPTER 1

1.3 Concept of the iron-making process mediated by oxalic acid

  The concept of the proposed iron-making process in this study is shown schematically in **Figure 1-4**, and an outline of the process flow is presented in **Figure S1-1.**
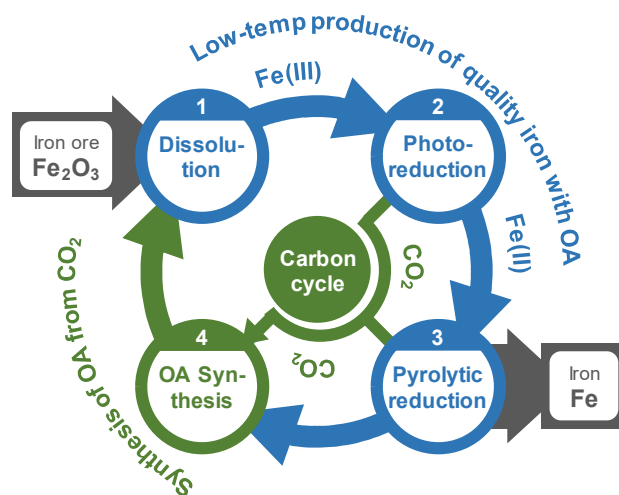
Figure 1-4. Concept of iron-making process proposed in this study. OA: oxalic acid.
Reprinted with permission from Santawaja et al. 2020. Copyright 2020 American Chemical Society.

  The iron-making consists of three steps: (1) dissolution of iron from iron ore using oxalic acid to obtain Fe(III) oxalate in an aqueous solution (Eq. 1); (2) photochemical reduction of Fe(III) oxalate to Fe(II) oxalate (Eq. 2); and (3) pyrolytic reduction of Fe(II) oxalate, obtained as a solid in the previous step, to metallic iron (Eq. 3). The reactions in the second and third steps generate CO and CO_2, which are recovered and used as feedstock for oxalic acid synthesis (Eq. 5) in combination with a water-gas shift (WGS; Eq. 4). As represented by eq. 6 for the overall reaction in the process, the combination of these reactions enables the iron-making without carbon in stoichiometry.

Iron dissolution: $Fe_2O_3 \text{ (s)} + 3H_2C_2O_4 \text{ (aq)} \rightarrow Fe_2(C_2O_4)_3 \text{ (aq)} + 3H_2O$ Eq. 1

Photochemical reduction: $Fe_2(C_2O_4)_3 \text{ (aq)} + 4H_2O \rightarrow 2FeC_2O_4 \cdot 2H_2O \text{ (s)} + 2CO_2 \text{ (g)}$ Eq. 2

Pyrolytic reduction: $FeC_2O_4 \cdot 2H_2O \text{ (s)} + H_2 \rightarrow Fe \text{ (s)} + CO \text{ (g)} + CO_2 \text{ (g)} + 3H_2O$ Eq. 3

6

WGS: $\qquad$ $CO + H_2O \rightarrow CO_2 + H_2$ $\qquad$ Eq. 4

Oxalic acid synthesis: $\quad$ $2CO_2 + H_2 \rightarrow H_2C_2O_4$ $\qquad$ Eq. 5

Net reaction: $\qquad$ $Fe_2O_3 + 3H_2 \rightarrow 2Fe + 3H_2O$ $\qquad$ Eq. 6
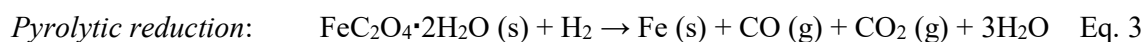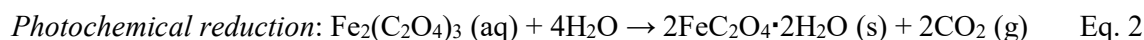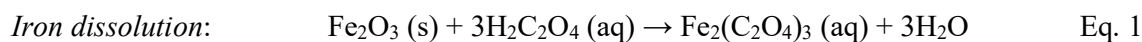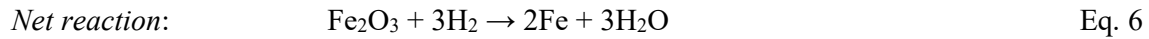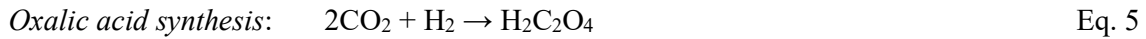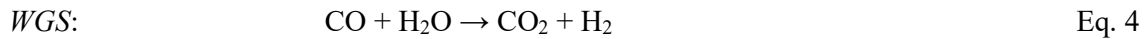
It is noteworthy that although the chemistries involved in the process have been basically studied or well-known, there has never been a research applying them to the iron-making. From the previous studies, it is chemically possible that the reactions depicted in Eqs. 1–3 produce iron from iron oxides. By exploiting the characteristics of oxalic acid and its anion as the ligand, iron is chemoselectively extracted, reduced from trivalent to divalent, recovered as solid, and then reduced to a metallic state. On the other hand, there is substantial uncertainty in the iron-making process, particularly in relation to iron productivity that is huge in the current industrial processes, exceeding 2 ton/m^3/day for the BF. [18]. Then, the reactions are requested to be faster and occur at a high iron concentration. However, due to the difference in purposes, the above-mentioned studies focus mainly on the reactions in diluted oxalic acid aqueous solutions at a pH adjusted by alkali oxalate. Moreover, the occurrence of reactions according to Eqs. 1–3 is important to establishing a carbon-neutral iron-making process with full iron recovery.

CHAPTER 1

1.4 Overview of dissertation

This dissertation consists of six chapters. The following is a brief description of each chapter.

Chapter 1 of this dissertation introduces the background, motivations and objectives of this work. A briefs review of the current status of ironmaking process including both conventional and alternative iron-making process are summarized. After that, the motivation and objectives of this work are provided. In this chapter, the concept of the iron-making process mediated by oxalic acid is introduced, followed by the overview of the dissertation

In chapter 2, the dissolution of iron oxides using oxalic acid which is the first step of this novel iron-making approach is described. The factors that influence the dissolution are varied in order to obtain the best condition for the dissolution. The effect of types of iron oxides, namely α-Fe_2O_3, $FeOOH$, and Fe_3O_4, and the temperature used for the dissolution were studied. The molar ratio of oxalic acid to Fe (OxA/Fe) is also crucial and studied to find the optimum ratio that provides the complete dissolution and achieves maximum Fe dissolution by using oxalic acid. The analysis of the dissolved iron species is also investigated and explained in terms of the OxA/Fe and the final solution pH.

Chapter 3 describes the second step of this iron-making method which is the photochemical reduction of iron (III) oxalate aqueous solution to recover iron as in solid form, Fe(II) oxalate dihydrate. As this process requires light to induce the reaction, the effects of various light sources, such as simulated sunlight, natural sunlight, and LED with specific wavelengths (LED-365 nm, LED-450 nm, LED-525 nm and LED-730 nm), as well as light intensities in terms of photon flux density (PFD) were investigated. Various influences on the rate of photochemical reduction are determined under simulated sunlight, for example, the solution depth, the iron sources, and their initial concentration in the solution.

In chapter 4, the pyrolytic reduction of the Fe(II) oxalate dihydrate to produce metallic iron which is the last step of the proposed iron-making process is studied. The various pyrolytic atmospheres, such as N_2, 50%H_2/N_2, 50%CO_2/N_2, 50%CO/N_2, and 50%air/N_2, were used to investigate the thermal behaviors of Fe(II) oxalate dihydrate under to provide the importance information for the design of pyrolytic reactor, analyzed by TGA. Moreover, the pyrolytic reduction of the obtained Fe(II) oxalate dihydrate from previous steps under 50%H_2/N_2 atmosphere is also demonstrated.

Chapter 5 is a proof of this proposed process on a lab-scale experiment. The findings in chapter 2-4 are applied in this chapter in order to attain the metallic iron as the final product when the iron samples contain the other metal impurities. Two types of iron ore and conventional slag were used for this proof in order to investigate the effect of metal impurities. The obtained iron products were characterized to reveal their structures and phases. Some suggestions and highlights are included for further investigations.

Finally, Chapter 6 summarized the findings described in the preceding chapters, and the future challenges of this process are also described.

CHAPTER 1

1.5 References

[1] Association, W. Steel Demand Forecasts https://www.worldsteel.org/media-centre/press-releases/2019/worldsteel-short-range-outlook-2019.html. Accessed January 2020

[2] Cahyono, R. B.; Yasuda, N.; Nomura, T.; Akiyama, T. Utilization of Low Grade Iron Ore (FeOOH) and Biomass through Integrated Pyrolysis-Tar Decomposition (CVI Process) in Ironmaking Industry: Exergy Analysis and Its Application. ISIJ Int. 2015, 55 (2), 428–435. https://doi.org/10.2355/isijinternational.55.428.

[3] Siitonen, S.; Tuomaala, M.; Ahtila, P. Variables Affecting Energy Efficiency and CO_2 Emissions in the Steel Industry. Energy Policy 2010, 38 (5), 2477–2485. https://doi.org/10.1016/j.enpol.2009.12.042.

[4] Chukwuleke, O. P.; CAI, J. ju; Chukwujekwu, S.; XIAO, S. Shift from Coke to Coal Using Direct Reduction Method and Challenges. J. Iron Steel Res. Int. 2009, 16 (2), 1–5. https://doi.org/10.1016/S1006-706X(09)60018-2.

[5] Harada, T.; Tanaka, H. Future Steelmaking Model by Direct Reduction Technologies. ISIJ Int. 2011, 51 (8), 1301–1307. https://doi.org/10.2355/isijinternational.51.1301.

[6] Hasanbeigi, A.; Arens, M.; Price, L. Alternative Emerging Ironmaking Technologies for Energy-Efficiency and Carbon Dioxide Emissions Reduction: A Technical Review. Renew. Sustain. Energy Rev. 2014, 33, 645–658. https://doi.org/10.1016/j.rser.2014.02.031.

[7] Davis, S. J.; Lewis, N. S.; Shaner, M.; Aggarwal, S.; Arent, D.; Azevedo, I. L.; Benson, S. M.; Bradley, T.; Brouwer, J.; Chiang, Y. M.; et al. Net-Zero Emissions Energy Systems. Science 2018, 360 (6396). https://doi.org/10.1126/science.aas9793.

[8] IEA. Industry direct CO_2 emissions in the Sustainable Development Scenario, 2000-2030 https://www.iea.org/data-and-statistics/charts/industry-direct-co2-emissions-in-the-sustainable-development-scenario-2000-2030

[9] Association, W. World Steel in Figure 2019; 2019. https://www.worldsteel.org/media-centre/press-releases/2019/world-steel-in-figures-2019.html. Accessed January 2020.\

[10] RITE. Estimation of Specific Energy Consumption for Integrated Steelmaking Process in 2010. 2012, 1–18.

[11] Lu, W. K.; Huang, D. F. The Evolution of Ironmaking Process Based on Coal-Containing Iron Ore Agglomerates. ISIJ Int. 2001, 41 (8), 807–812. https://doi.org/10.2355/isijinternational.41.807.

[12] Palacios, P.; Toledo, M.; Cabrera, M. Iron Ore Reduction by Methane Partial Oxidation in a Porous Media. Int. J. Hydrogen Energy 2015, 40 (31), 9621–9633. https://doi.org/10.1016/j.ijhydene.2015.05.058.

[13] Carmo de Lima, L.; Duarte, J. B. F.; Veziroglu, T. N. A Proposal of an Alternative Route for the Reduction of Iron Ore in the Eastern Amazonia. Int. J. Hydrogen Energy 2004, 29 (6), 659–661. https://doi.org/10.1016/S0360-3199(03)00053-3.

[14] Yilmaz, C.; Turek, T. Modeling and Simulation of the Use of Direct Reduced Iron in a Blast Furnace to Reduce Carbon Dioxide Emissions. J. Clean. Prod. 2017, 164, 1519–1530.

[15] Guo, D.; Hu, M.; Pu, C.; Xiao, B.; Hu, Z.; Liu, S.; Wang, X.; Zhu, X. Kinetics and Mechanisms of Direct Reduction of Iron Ore-Biomass Composite Pellets with Hydrogen Gas. Int. J. Hydrogen Energy 2015, 40 (14), 4733–4740. https://doi.org/10.1016/j.ijhydene.2015.02.065.

[16] Hosokai, S.; Kasiwaya, Y.; Matsui, K.; Okinaka, N.; Akiyama, T. Ironmaking with Ammonia at Low Temperature. Environ. Sci. Technol. 2011, 45 (2), 821–826.

[17] Yasuda, N.; Mochizuki, Y.; Tsubouchi, N.; Akiyama, T. Reduction and Nitriding Behavior of Hematite with Ammonia. ISIJ Int. 2015, 55 (4), 736–741. https://doi.org/10.2355/isijinternational.55.736.

[18] Ujisawa, Y.; Sunahara, K.; Matsukura, Y.; Nakano, K.; Yamamoto, T. Effect of HBI Use on Blast Furnace Performance. Tesu-to-Hagane 2006, 92 (10), 591–600. https://doi.org/10.2355/tetsutohagane1955.92.10_591

1.6 Supporting information
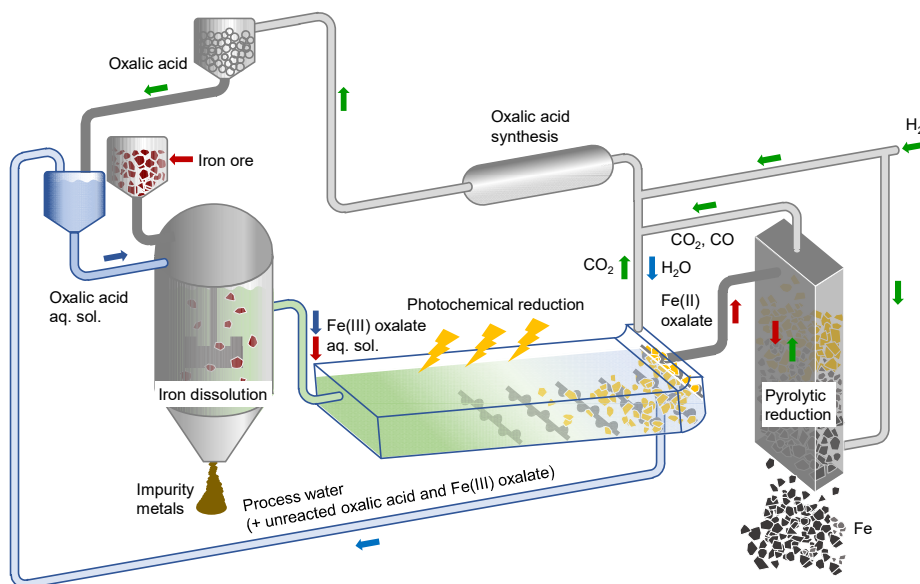
Figure S1-1. Outline of the process flow.

Reprinted with permission from Santawaja et al. 2020. Copyright 2020 American Chemical Society.

The reactors for iron dissolution, photochemical reduction, and pyrolytic reduction are designed and illustrated for the continuous operation: 1) A continuous stirred tank reactor for the iron dissolution has a filter at the outlet to prevent solids from flowing out of the reactor, 2) The photochemical reduction pool is designed to enable light irradiation over the liquid surface as large as possible, collection of gaseous products, and sweeping the solid precipitates with paddles at the bottom, and 3) The reactor for pyrolytic reduction is an updraft moving bed reactor to allow the operation with minimum consumption of hydrogen and to reduce the contact between pyrolysis gas and pyrolyzing solids.

CHAPTER 2

Dissolution of Iron Oxides with Oxalic Acid

2.1 Introduction

Dissolution of iron oxides such as hematite (α-Fe$_2$O$_3$), magnetite (Fe$_3$O$_4$), and goethite (α-FeOOH) is an important chemical process in industries to improve properties of industrial minerals or avoid troubles of the processes (e.g., ore, clay, quartz, soil, and ceramic). During this process, the iron oxides, as impurity metals, are removed by acids. [1-5] Inorganic (HCl and HNO$_3$) and organic acids (oxalic, acetic, L-ascorbic, and citric acids) have been studied for the iron oxide dissolution. [1-8] Among them, oxalic acid has been suggested to be the most promising acid due to its high acid strength, complexing ability, and reducing property. [8-12] Moreover, since it can be easily decomposed by calcination, there is no risk of contaminating the treated materials. [5,11]

The dissolution of iron oxides in oxalic acid aqueous solution is generally explained by three different mechanisms: (1) adsorption of oxalate anions on the surface of iron oxide via protonation and complexation, (2) non-reductive dissolution, and (3) reductive dissolution. [13,14] The adsorption of oxalate anions is the initial step, followed by non-reductive dissolution and/or reductive dissolution, depending on operating conditions. The non-reductive dissolution is a simple desorption process for removing only active sites over iron oxides and is more likely to occur at a low pH and high temperatures, which increases the number of active sites. The reductive dissolution consists of induction and autocatalytic periods. The induction period is to generate ferrous ions (Fe^{2+}). When the concentration of Fe^{2+} reaches a sufficient level, the autocatalytic period is initiated by the generated catalytic species, [Fe^{2+}(C$_2$O$_4$)$_2$]$^{2-}$, accelerating the iron dissolution. When an iron oxide has Fe(II) in the structure (e.g., magnetite),

the rate of dissolution is fast because the catalytic anion is directly formed upon adsorption of oxalate anions. The reductive dissolution of iron oxides without Fe(II) (e.g., hematite and goethite) in the structure requires electron transfer from adsorbed oxalate anions to Fe(III) in the induction period, which is the rate-determining step in the dissolution.

The efficiency of dissolution using oxalic acid is affected by several factors. [6,13,15-20] The pH of aqueous solution remarkably influences the rate of iron dissolution, and studies have revealed the optimum pH in the range of 2.5–3.0. [10,15,16] Several types of thermodynamically stable iron oxalate complex ions under different pH have been reported. [17] In a high pH solution (pH > 3), $[Fe^{2+}(C_2O_4)_2]^{2-}$ and $[Fe^{3+}(C_2O_4)_3]^{3-}$ are thermodynamically stable, while $[Fe^{3+}(C_2O_4)_2]^-$ and $[Fe^{3+}C_2O_4]^+$ are stable at the pH of 1–2. Only $[Fe^{3+}HC_2O_4]^{2+}$ presents in a highly acidic solution (pH < 1). Uncomplexed Fe^{2+} is also found in the highly acidic aqueous solution, but uncomplexed Fe^{3+} is unlikely to form in oxalic acid solutions.

Apart from the pH effect, the rate of dissolution increases with the concentration of oxalic acid. [2] However, in the case of magnetite dissolution, the effect of oxalic acid concentration is diminished by the richness in autocatalytic species. [21] The temperature also contributes to the acceleration of dissolution, where reasonable dissolution rates are found above 80 °C. [2,6,13,16,18] Besides, the ratio between leachate (oxalic acid solution) and loaded iron oxide-containing materials, so-called liquid-solid ratio (L/S ratio), is an important factor for the efficient dissolution. [19,20]

The proposed iron-making process in this study starts with the iron oxide dissolution from iron ore as presented in **Figure S2-1**. [22] Iron dissolved mainly as Fe(III) oxalate (Eq. 2.1 for Fe_2O_3) is reduced to metallic iron in two steps; photochemical reduction and pyrolytic reduction. Unique chemical properties of iron oxalates enable iron-making at low temperatures. To extract iron selectively and produce a high purity iron, the iron oxide dissolution process is

operated in the absence of light. For achieving high iron productivity of the process, it is required to produce the solution with a high concentration of iron oxalates as fast as possible. However, previous studies on iron oxide dissolution have been carried out basically at diluted conditions with the addition of buffering agents to control the pH in the optimum range. [12,14-16,23-25]

To the best of our knowledge, there has been no research that focused mainly on the dissolution of highly loaded iron oxides. Moreover, the amount of oxalic acid required to completely dissolve iron (molar ratio of oxalic acid to iron loaded in the solution: OxA/Fe) has not been reported regardless of its importance for minimizing the consumption of oxalic acid. The dissolution of iron oxides is unlikely to simply follow the Eq. 2.1, considering the presence of several types of iron oxalates in the solution as mentioned above.

$$Fe_2O_3 + 3H_2C_2O_4 \rightarrow Fe_2(C_2O_4)_3 + 3H_2O \qquad \text{Eq. 2.1}$$
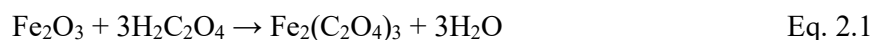
Therefore, in the present study, the dissolution of iron oxides highly loaded in the oxalic acid aqueous solution (up to 1.3 mol-Fe/L) in the absence of light and with no addition of other chemical reagents under atmospheric pressure has been investigated. Hematite (α-Fe_2O_3), goethite ($FeOOH$) and magnetite (Fe_3O_4) were used as iron precursors typically contained in iron ores. We believe that the findings serve as a guideline for achieving an efficient iron oxide dissolution in the potential iron-making process, and provide further insight into the mechanism of iron oxide dissolution by oxalic acid as well.

2.2 Materials and methods

2.2.1 Materials

α-Fe_2O_3 and Fe_3O_4 were purchased from Sigma-Aldrich, and $FeOOH$ was purchased from Nacalai Tesque. Anhydrous oxalic acid (Wako Pure Chemical) was used as a reagent for

the iron dissolution. 1,10-phenanthroline (Aldrich), ammonium acetate (Wako Pure Chemical), and hydroxylamine (Wako Pure Chemical) were used for quantification of dissolved iron.

2.2.2 Iron dissolution

The iron oxide dissolution experiments were carried out in a dark room to protect the solution from light. The irradiation of light, particularly within the tropospheric solar UV-visible region (290–570 nm), causes reduction of Fe(III) oxalate to water-insoluble Fe(II) oxalate. [22] The quantum efficiency of this photochemical reaction is close to unity. [26] Upon the light irradiation, the amount of dissolved iron, therefore, readily decreases. This phenomenon is not preferred for the proposed iron-making process, because it decreases the yield of metallic iron on a feedstock iron basis.

A 50 mL of centrifuge tube with a silicone cap was used as a reactor in all experiments, excepted the experiment performing at 99 °C, the three-necked round bottom flask equipped with condenser was used. A needle for syringe was penetrated through the silicone cap for keeping atmospheric pressure and sampling of the solution during the iron dissolution. The photos of dissolution set-up are shown in **Figure 2-1**.

Various loading amounts of iron oxides (4.7–100 g-iron oxide/L: 0.05–1.3 mol-Fe/L) and oxalic acid concentrations (0.1–1.0 mol/L) were investigated. The iron oxide with particle sizes below 38 μm was added to a hot oxalic acid aqueous solution (47, 75, 92 or 99 °C), and then the slurry was stirred for 360 min using an oil bath with a magnetic stirrer. The dissolution temperatures are hereafter denoted by 45, 75, 90 and 99 °C, respectively, for the simplification. During the dissolution, 30 μL of the solution was sampled at predetermined times to quantify the dissolved iron by absorption spectroscopy. The volume of sampling amount was small enough to neglect the influence on the analysis of the dissolution. The pH of the solution was

not controlled throughout the experiment. After the test, the slurry was naturally cooled down to room temperature and centrifuged at 4000 rpm for 10 min to separate the aqueous solution from the remaining solids. Some of the recovered solutions, iron oxalate aqueous solution, was subjected to photochemical reduction (in Chapter 3), and the solids were washed until a neutral pH and dried at 60 °C in vacuo.
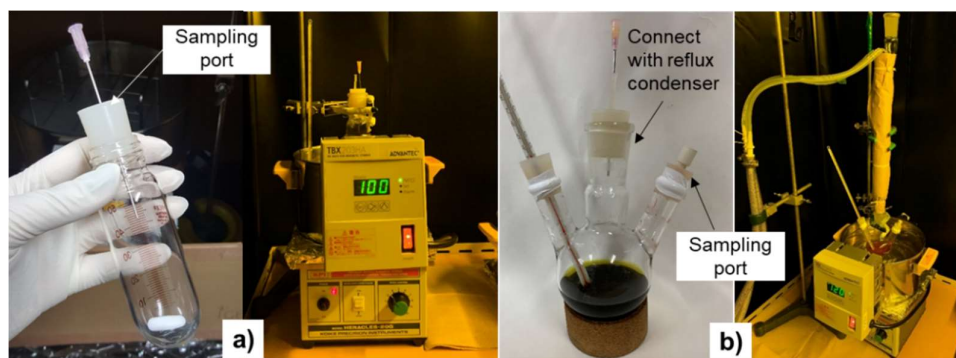
Figure 2-1. Photos of dissolution set-up: a) set-up for dissolution at 47, 75 and 92 °C, b) reflux set-up for dissolution at 99°C

2.2.3 Characterizations

The concentration of iron dissolved in the solution was determined by absorption spectroscopy with a UV-Vis spectrophotometer (PerkinElmer, Lambda 365). For investigating chemistry of the dissolution in detail, the dissolved iron was analytically categorized into two types, Fe^{2+} species and Fe^{3+} species. For determining the total concentration of Fe^{2+} and Fe^{3+} species, prescribed amounts of hydroxylamine, 1,10-phenanthroline, ammonium acetate, and deionized water were added as the reducing agent, complexing agent, buffering agent, and diluting solution, respectively, immediately after the sampling in the darkroom, and then the solution was subjected to the spectroanalysis. The experimental details of the spectroanalysis is also provided in **Appendix I.** The iron concentration was determined by measuring the absorbance of tris(1,10-phenanthroline)iron(II) ($[Fe(phen)_3]^{2+}$) at 510 nm. This analysis

determined the total concentration of Fe^{2+} and Fe^{3+} species. While the concentration of Fe^{2+} species was determined by the analysis of the solution prepared in the absence of the reducing agent. The concentration of Fe^{3+} species was calculated by the difference between total and Fe^{2+} concentrations. The concentrations of Fe^{2+} species, Fe^{3+} species, and their total in the solution are hereafter denoted by Fe^{2+}, Fe^{3+}, and total Fe concentrations, respectively. The rate of iron dissolved in the solution from feedstock (Fe dissolution) was calculated from the dissolved iron and iron loaded in the solution.

Crystalline structures of solid samples were analyzed by X-ray diffraction, XRD, on a Rigaku TTR-III X-ray diffractometer with Cu Kα radiation at 50 kV and 30 mA.

2.3 Results and dissolution

2.3.1 Effect of iron oxide types

Figure 2-2 shows the experimental results of dissolution of α-Fe_2O_3, FeOOH, and Fe_3O_4 in 0.5 M oxalic acid aqueous solution at 75 °C. The loaded iron oxides were 0.33 mol-Fe/L, corresponding to 26.3 g/L, 29.3 g/L, and 25.4 g/L for α-Fe_2O_3, FeOOH, and Fe_3O_4, respectively.

As seen from the results, the rate of dissolution depended significantly on the type of iron oxide; Fe_3O_4 was the fastest, followed by α-Fe_2O_3 and then FeOOH. Fe dissolution of Fe_3O_4 reached 80% within 30 min and then remained almost unchanged in 6 h of the run. On the other hand, Fe dissolutions of α-Fe_2O_3 and FeOOH gradually increased and, at 6 h, reached 77% and 71%, respectively. It should be mentioned that, although the dissolution of Fe_3O_4 was fast, the dissolution was incomplete, and the product contained a solid residue that was a precipitated Fe(II) oxalates, the details of which are discussed later. The fast dissolution of Fe_3O_4 was due to the presence of Fe(II) in the structure. Fe^{2+} was dissolved into the solution at an early stage of the dissolution, forming the complex with oxalate anions to work as a type of

catalyst for the iron dissolution. [13,14,24,27] These events nearly completed before the first sampling at 15 min, but the occurrence was apparent from the abundance of Fe^{2+} in the solution, compared to those using α-Fe_2O_3 and FeOOH as the feedstock.
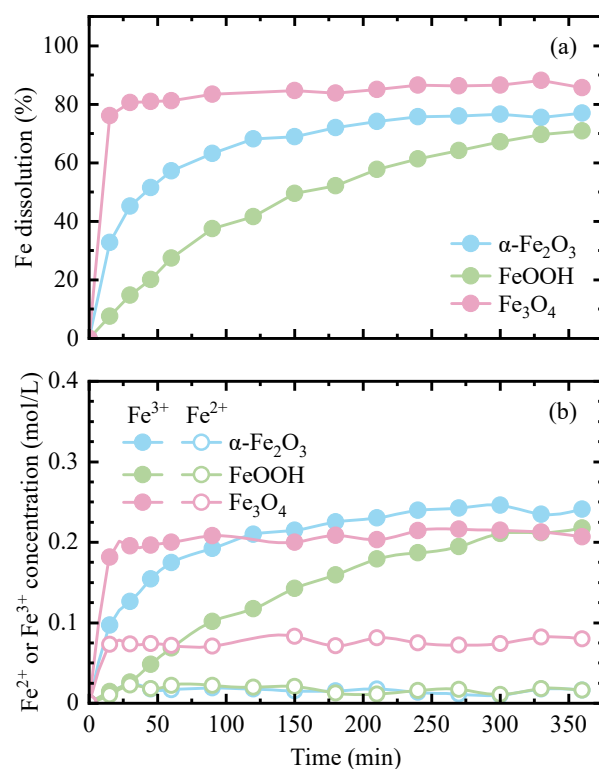
Figure 2-2 Time-dependent change of (a) Fe dissolution and (b) Fe^{2+} or Fe^{3+} concentration. Conditions: 75 °C, 0.33 mol-Fe/L loaded iron oxide, and 0.5 mol/L oxalic acid

The distribution of dissolved Fe species (**Figure 2-2** (b)) showed that the majority of dissolved iron in all solutions was trivalent iron (Fe^{3+}) species. The result indicated that the dissolution mainly followed the non-reductive dissolution, where active sites over iron oxide surface were removed by active hydrogen ions in the solution. [10,13,23-25,28] This conflicted with a generally accepted mechanism of reductive dissolution for the iron dissolution using organic acids. On the other hand, the iron dissolution in the present study occurred under a highly acidic solution because more oxalic acid was required to dissolve highly loaded iron

oxides, compared to general studies. In addition, the dissolution was carried out at a relatively high temperature (75 °C) without the exposure to light that promotes the generation of Fe(II) oxalates. Therefore, under the conditions examined in this study, the non-reductive dissolution is suggested to be a dominant pathway, because those conditions contribute to the increase in the number of active sites over iron oxides. [24,29]

Fe(III) oxalate in the solution is supposed to be in the form of $[Fe^{3+}HC_2O_4]^{2+}$, having dissociation constant $(K_d) = 2.95 \times 10^{-10}$, because it is the most stable form in a highly acidic solution of pH < 1. [17] With this in consideration, reactions of α-Fe_2O_3 and FeOOH dissolution are described by Eqs. 2.2 and 2.3, respectively. Trace amounts of Fe^{2+} in the solution of α-Fe_2O_3 and FeOOH occurred possibly via the reductive dissolution pathway by electron transfer from oxalate anion [13], resulting in the formation of uncomplexed Fe^{2+}, as shown in Eqs. 2.4 and 2.5, where the symbol, "$\rangle$", is used to represent species at the surface of iron oxides.

$$Fe_2O_3 + 2HC_2O_4^-{}_{(aq)} + 6H^+{}_{(aq)} \rightarrow 2[Fe^{3+}HC_2O_4]^{2+}{}_{(aq)} + 3H_2O_{(l)} \qquad \text{Eq. 2.2}$$

$$2FeOOH + 2HC_2O_4^-{}_{(aq)} + 6H^+{}_{(aq)} \rightarrow 2[Fe^{3+}HC_2O_4]^{2+}{}_{(aq)} + 3H_2O_{(l)} \qquad \text{Eq. 2.3}$$

$$[\rangle Fe^{III}-C_2O_4^{2-}] \leftrightarrow [\rangle Fe^{II}-C_2O_4^-] \qquad \text{Eq. 2.4}$$

$$2[\rangle Fe^{II}-C_2O_4^-] + 2H^+{}_{(aq)} \leftrightarrow 2Fe^{2+}{}_{(aq)} + 2CO_2 + C_2O_4^{2-}(aq) + 2 \rangle H \qquad \text{Eq. 2.5}$$
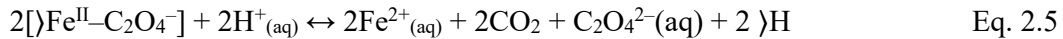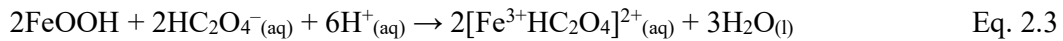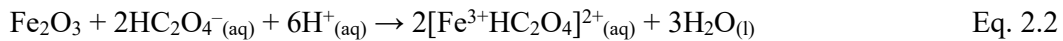
The dissolution of Fe_3O_4 with oxalic acid has been reported as Eq. 2.6, where iron is dissolved as $[Fe^{3+}(C_2O_4)_3]^{3-}$ and $[Fe^{2+}(C_2O_4)_2]^{2-}$ at the ratio of 2. [24,27] However, OxA/Fe of 2.67, assumed in Eq. 2.6, is much higher than that applied in the present experiment (= 1.5). Considering the most stable chemical forms of dissolved Fe^{3+} and Fe^{2+} as $[Fe^{3+}HC_2O_4]^{2+}$and uncomplexed Fe^{2+}, respectively, under conditions of this study, the dissolution of Fe_3O_4 is rewritten by Eq. 2.7. Furthermore, the presence of Fe(II) oxalate precipitate, which has little

solubility in water ($K_{sp} = 2 \times 10^{-7}$ at 25 °C), [17] in the solution indicated the occurrence of a reaction described by Eq. 8. In the concentration profiles of **Figure 2-2** (b), the reaction system, consisting of Eqs. 2.7 and 2.8, reached the equilibrium in 30 min, and the concentrations of Fe^{3+} and Fe^{2+} were almost unchanged over the time period thereafter. Fe^{3+}/Fe^{2+} ratio in the solution after reaching the equilibrium was roughly consistent with the stoichiometry of Eq. 2.7.

$$Fe_3O_4 + 8HC_2O_4^-{}_{(aq)} \rightarrow 2[Fe^{3+}(C_2O_4)_3]^{3-}{}_{(aq)} + [Fe^{2+}(C_2O_4)_2]^{2-}{}_{(aq)} + 4H_2O_{(l)} \qquad \text{Eq. 2.6}$$

$$Fe_3O_4 + 2HC_2O_4^-{}_{(aq)} + 8H^+{}_{(aq)} \rightarrow 2[Fe^{3+}HC_2O_4]^{2+}{}_{(aq)} + Fe^{2+}{}_{(aq)} + 4H_2O_{(l)} \qquad \text{Eq. 2.7}$$

$$Fe^{2+}{}_{(aq)} + C_2O_4^{2-}{}_{(aq)} \leftrightarrow FeC_2O_{4(s)} \qquad \text{Eq. 2.8}$$
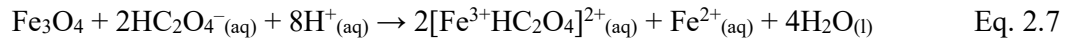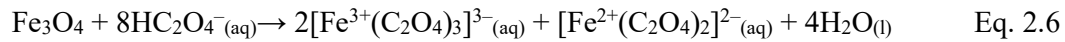
2.3.2 Effect of dissolution temperature

To investigate the effect of temperature on the dissolutions of iron oxides: $\alpha\text{-}Fe_2O_3$, $FeOOH$, and Fe_3O_4, the loaded iron oxides of 0.33 mol-Fe/L were performed in 0.50M aqueous oxalic acid solution at three different temperatures: 45, 75, and 90 °C, and the experimental results are shown in **Figure 2-3.** It is clearly sees from the results that although the rate of dissolution depends on types of iron oxides as described in previous section, the dissolution rates were significantly improved by increasing temperature. Higher temperature resulted in a faster dissolution of iron oxides, therefore, the rate of dissolution at dissolution temperature as 90 °C is fastest, followed by 75 and 45 °C, respectively. The reasons behind this phenomenon are probably because the increasing of temperature improves not only the dissolution rate by increasing the active sites, but also the dissociation of oxalic acid leading to the higher active species of oxalic acid.
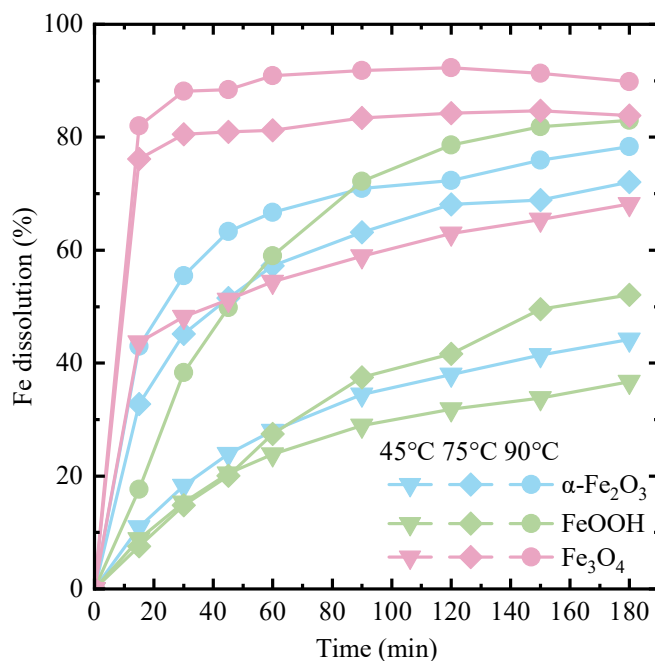
Figure 2-3. Time-dependent change of Fe dissolution at different temperatures. Conditions: 0.33 mol-Fe/L loaded iron oxide, 0.5 mol/L oxalic acid, and 180 min.

To further investigate the effect of dissolution temperature, the dissolution temperature as high as 99 °C was used. In this experiment, the dissolutions of α-Fe$_2$O$_3$ with the loaded iron oxides as 0.50 mol-Fe/L were performed in 1.0 M oxalic acid aqueous solution at two different temperatures: 90, and 99 °C by using the reflux set-up to prevent the decomposition of oxalic acid when the solution was boiling. The experimental results are shown in **Figure 2-4.**

As expected, the rate of dissolution is significantly increased by performing dissolution at 99 °C. The dissolution of 0.50 mol-Fe/L of α-Fe$_2$O$_3$ was completed within 120 min which is faster than that using 90 °C for 90 min. However, after the completion of dissolution, the percent of Fe dissolution gradually decreased, as clearly seen in **Figure 2-4.** This is probably because the dissolution temperature as high as 99 °C not only improved the dissolution rate but also increased the possibility of iron(II) oxalate precipitation by disturbing or destroying the

equilibrium between each dissolved iron species and oxalate, which causes the precipitation of iron(II) oxalate.
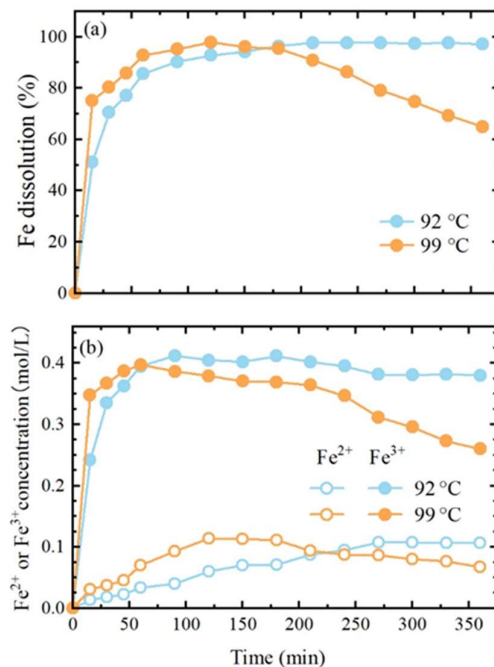
Figure 2-4. Time-dependent change of (a) Fe dissolution and (b) Fe^{2+} or Fe^{3+} concentration. Conditions: 0.50 mol-Fe/L loaded α-Fe_2O_3, and 1.0 mol/L oxalic acid.

2.3.3 Effect of OxA/Fe on the dissolution of iron oxides

OxA/Fe is an important parameter for enabling a complete iron oxide dissolution while minimizing the consumption of oxalic acid. The experiments of **Figure 2-2** employed OxA/Fe = 1.5, which was determined from the stoichiometry of Eq. 2.1. However, the product solutions from all iron oxides contained undissolved iron oxides, indicating that OxA/Fe = 1.5 was insufficient for achieving the complete dissolution.

To investigate the effect of OxA on the iron oxide dissolution and involved reactions, the experiments were carried out at various oxalic acid concentrations (0.1–1.0 mol/L) and iron oxides loadings (0.05–1.3 mol-Fe/L), providing the OxA/Fe from 0.4 to 10, at 90 °C for 360 min in the absence of light. The dissolution temperature of 90 °C was chosen to avoid boiling

the solution in the experiment under atmospheric pressure although temperatures higher than 90 °C were effective for further facilitating the dissolution. **Figure S2.2** presents time-dependent changes in Fe dissolution and total Fe concentration. The result showed steady Fe dissolutions at the late stage of experiments, indicating that the conditions of 90 °C and 360 min were sufficient for achieving Fe dissolution at the equilibrium.

The data set obtained from the experiments under 167 different conditions (oxalic acid concentration, iron oxide loadings and iron oxide types) are listed in **Tables S2-1–S2-3**. It is to be noted that oxalic acid concentration was limited up to 1.0 mol/L due to its solubility in water at room temperature. It was confirmed from the results that the majority of iron dissolved in the solution presented as Fe^{3+} species. Total Fe concentrations from α-Fe_2O_3, FeOOH, and Fe_3O_4 reached 0.56, 0.55, and 0.50 mol/L, respectively. The data were further analyzed under the assumption that Fe dissolution reaches the equilibrium value in the experiment of 360 min, i.e., Fe dissolution would not change after longer dissolution.

Figure **2-5** plots Fe dissolution or the ratio between Fe^{2+} and Fe^{3+} species concentrations (Fe^{2+}/Fe^{3+}) against OxA/Fe. It can be seen from **Figure 2-5** (a) that the Fe dissolution increases linearly with OxA/Fe until it reaches plateaus that are almost 100% for α-Fe_2O_3 and FeOOH, and 80–90% for Fe_3O_4. The linear correlation between Fe dissolution and OxA/Fe, obtained from the plots, is approximated by $y = 54.8x$ with the regression coefficient $R^2 = 0.95$, where y and x are Fe dissolution and OxA/Fe, respectively. For α-Fe_2O_3 and FeOOH, Fe dissolution reaches 100% at OxA/Fe = 1.82 (= 100/54.8). This is the required minimum OxA/Fe to achieve the complete dissolution. In the case of Fe_3O_4, because a portion of dissolved iron precipitates as Fe(II) oxalate, the Fe dissolution does not reach 100%, as observed in **Figure 2-2**.
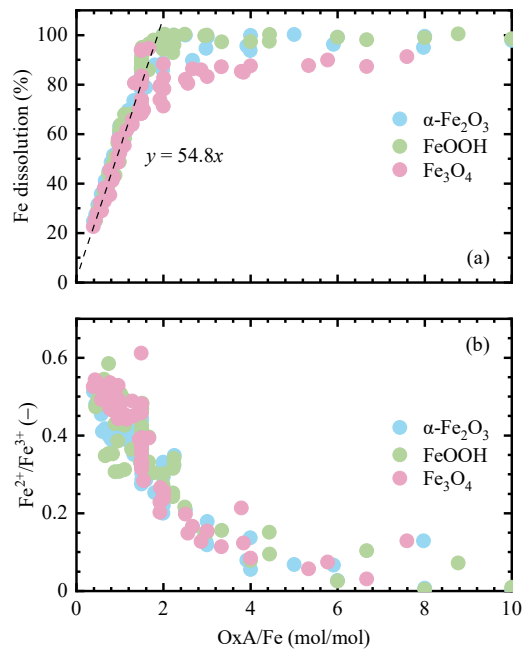
Figure 2-5. Fe dissolution (a) and Fe^{2+}/Fe^{3+} (b) plotted against OxA/Fe. The data were obtained from the dissolution experiments at 90 °C for 360 min with 0.1–1.0 mol/L oxalic acid and 0.05–1.3 mol-Fe/L loaded iron oxide.

As shown in **Figure 2-5** (b), Fe^{2+}/Fe^{3+} decreased with OxA/Fe, irrespective of the type of iron oxides. This was because of the stability of Fe(III) oxalates, which, compared to Fe(II) oxalates, increased with acidity. [17] Under the conditions employed in this experiment, the initial pH of oxalic acid aqueous solution was generally below 1, excepting 0.1 mol/L oxalic acid (pH = 1.23). Therefore, the iron dissolution was believed to follow the non-reductive mechanism, as evidenced by the presence of Fe(III) oxalates as the main Fe species for all the solutions after dissolution. Fe^{2+}/Fe^{3+} was thermodynamically determined by the chemical equilibrium, resulting in more abundance of Fe^{3+} with OxA/Fe.

According to the mechanism of non-reductive dissolution, the most important factor influencing the dissolution is active hydrogen ions, protons (H^+), generated from the dissociation of oxalic acid because protons create active sites over iron oxides surface by protonation. In Eqs. 2, 3, and 7, H^+ required for obtaining 1 mol of $[Fe^{3+}HC_2O_4]^{2+}$ is 3 mol or

4 mol. Oxalic acid dissociates in two steps (Eqs. 2.9 and 2.10) and potentially provides 2 mol

of H^+ per mol-OxA. When oxalic acid is fully dissociated, the required minimum of OxA/Fe

for the complete Fe dissolution is 1.5 as presented by Eq. 2.1. However, the complete Fe

dissolution at 90 °C, as shown in **Figure 2-5** (a), needed more OxA/Fe, 1.82. This was

attributed to the incomplete dissociation of oxalic acid. Using the dissociation constants, H^+

concentrations in 0.1–1.0 mol/L oxalic acid aqueous solution at 25 °C was calculated to be

0.07–0.24 mol/L. The dissociation of oxalic acid was temperature-dependent, resulting in

higher H^+ concentrations in the range of 0.09–0.27 mol/L at 90 °C.

$$H_2C_2O_{4(aq)} \leftrightarrow HC_2O_4^-{}_{(aq)} + H^+{}_{(aq)} \qquad (K_{a1} = 5.9 \times 10^{-2}) \qquad \text{Eq. 2.9}$$

$$HC_2O_4^-{}_{(aq)} \leftrightarrow C_2O_4^{2-}{}_{(aq)} + H^+{}_{(aq)} \qquad (K_{a2} = 6.2 \times 10^{-5}) \qquad \text{Eq. 2.10}$$

To correlate H^+ concentration with Fe dissolution, Eqs. 2.2 and 2.3 were employed, and

Fe dissolution was plotted against $3H^+$/Fe in **Figure 2-6,** where H^+ was a molar concentration

of proton generated by dissociation of oxalic acid at 90 °C, and Fe was a molar concentration

of Fe loaded as iron oxides. As with the case of plots against OxA/Fe, Fe dissolution increased

in proportion to $3H^+$/Fe, irrespective of iron oxide types, before reaching the plateau values.

The linear relationship had a slope of 54.3, which was close to that found in **Figure 2-5** (a).

Therefore, it was concluded that the reason for the required minimum OxA/Fe (= 1.82) to

complete the Fe dissolution was the requirement for dissociated protons to create a sufficient

number of active sites over the iron oxides surface by protonation. It is worth mentioning that

this finding corresponds to previous reports stating that when the dissolution is assisted by

proton (proton-assisted dissolution or protonation-induced dissolution), three protons are

required to detach Fe(III) into the solution. [30-33] One proton is adsorbed on the surface to

generate a positively charged site (Eq. 2.11), followed by a weakening of the Fe-O bond with

the additional two protons to dissolve Fe(III) into the solution (Eq. 2.12). The present

experimental results revealed that this pathway dominates the dissolution of highly loaded α-Fe_2O_3, FeOOH, and Fe_3O_4 under the conditions employed.

$$\rangle Fe^{III}OOH_{(s)} + H^+ \rightarrow \rangle Fe^{III}(OH)_2^+{}_{(s)} \qquad \text{Eq. 2.11}$$

$$\rangle Fe^{III}(OH)_2^+{}_{(s)} + 2H^+ \rightarrow Fe^{3+}{}_{(aq)} + 2H_2O \qquad \text{Eq. 2.12}$$
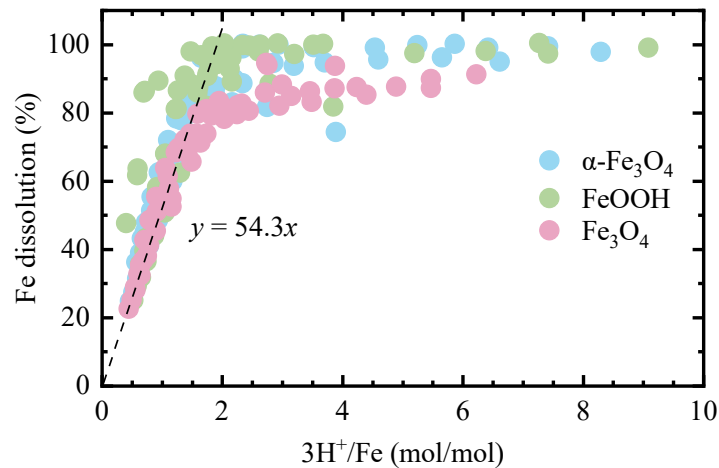
Figure 2-6. Fe dissolution plotted against H^+ concentration per Fe loaded in the solution, $3H^+/Fe$, derived from Eqs. 2.2 and 2.3. The data were obtained from the dissolution experiments at 90 °C for 360 min with 0.1–1.0 mol/L oxalic acid and 0.05–1.3 mol-Fe/L loaded iron oxide.

2.3.4 Fe dissolution at a constant oxalic acid concentration

To study and clarify the influence of OxA/Fe in more detail, a part of the data set in **Tables S2.1-S2.3** was extracted and replotted in **Figure 2-7**. **Figure 2-7** (a) presents the relationship between Fe dissolution and OxA/Fe at 0.5 mol/L of oxalic acid concentration. The loaded amount of iron oxides ranged from 10 to 100 g/L (0.1–1.3 mol-Fe/L). The plot confirmed that OxA/Fe = 1.82 was required for the complete dissolution of iron oxides at 90 °C.
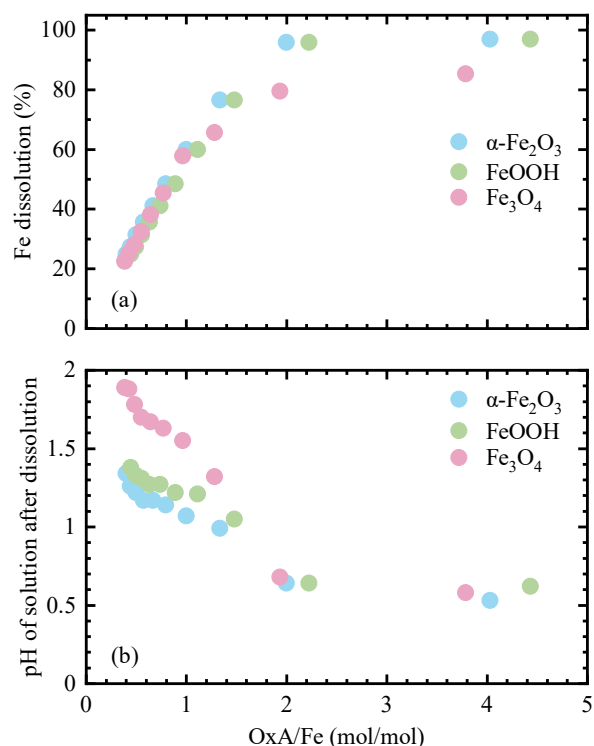
Figure 2-7. Fe dissolution and pH of the solution after dissolution plotted against OxA/Fe in the experiments with 0.5 mol/L oxalic acid and 0.05–1.3 mol-Fe/L loaded iron oxide at 90 °C for 360 min.

Figure 2-7 (b) presents the pH of the solution after dissolution. The pH of 0.5 mol/L fresh oxalic acid aqueous solution was 0.74. When the dissolution of iron oxides was completed (OxA/Fe ≥ 1.82), the pH of the solution was lower than 0.72. This was likely because the consumption of bioxalate anion to form $[Fe^{3+}HC_2O_4]^{2+}$ during the dissolution caused more dissociation of oxalic acid, contributing to the decrease in pH of the final solution. On the other hand, at the OxA/Fe below 1.82, the dissolution is incomplete, and the pH gradually increases in the range of 1–2 with the decrease of OxA/Fe because of the insufficient oxalic acid loaded in the solution.

The difference in pH of the resulting solution between below and above OxA/Fe = 1.82 indicated the occurrence of other chemical events in addition to Eqs. 2.2–2.5, 2.7, and 2.8. At

the pH of 1–2, the stable Fe(III) oxalates are $[Fe^{3+}(C_2O_4)_2]^-$ ($K_d = 6.31 \times 10^{-17}$) and $[Fe^{3+}C_2O_4]^+$ ($K_d = 3.98 \times 10^{-10}$). [17] Considering higher stability of $[Fe^{3+}(C_2O_4)_2]^-$, Eqs. 2.13–2.15 are supposed to be involved in the dissolution at the oxalic acid loadings insufficient for the complete dissolution of iron oxides. Fe(III) oxalate ($[Fe^{3+}HC_2O_4]^{2+}$) in Eqs. 2.2, 2.3, and 2.7 forms from an equivalent mole of oxalic acid, but $[Fe^{3+}(C_2O_4)_2]^-$ in Eqs. 2.13–2.15 requires two moles of oxalate, which reasonably explains the shortage of oxalates at OxA/Fe < 1.82, causing the high pH of the solution.

$$Fe_2O_3 + 4C_2O_4^{2-}{}_{(aq)} + 6H^+{}_{(aq)} \rightarrow 2[Fe^{3+}(C_2O_4)_2]^-{}_{(aq)} + 3H_2O_{(l)} \qquad \text{Eq. 2.13}$$

$$2FeOOH + 4C_2O_4^{2-}{}_{(aq)} + 6H^+{}_{(aq)} \rightarrow 2[Fe^{3+}(C_2O_4)_2]^-{}_{(aq)} + 4H_2O_{(l)} \qquad \text{Eq. 2.14}$$

$$Fe_3O_4 + 4C_2O_4^{2-}{}_{(aq)} + 8H^+{}_{(aq)} \rightarrow 2[Fe^{3+}(C_2O_4)_2]^-{}_{(aq)} + Fe^{2+}{}_{(aq)} + 4H_2O_{(l)} \qquad \text{Eq. 2.15}$$
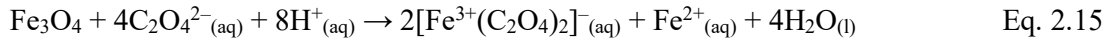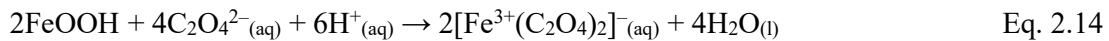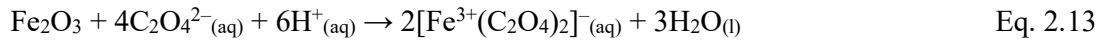
Figure 2-8 plots the total Fe, Fe^{2+}, and Fe^{3+} concentrations against the Fe loaded as iron oxides in 0.5 mol/L oxalic acid. As shown in **Figure 2-8** (a), the total Fe concentration increased with the loaded Fe and then remained constant at around 0.3 mol-Fe/L when the loaded Fe was over 0.3 mol-Fe/L. This result is explained by the required minimum OxA/Fe = 1.82, which corresponds to the maximum Fe concentration of 0.27 mol/L in 0.5 mol/L oxalic acid. Thus, when the loaded Fe was over 0.27 mol/L, the dissolution reached its maximum, and further increases in Fe loading did not result in the increase in total Fe concentration because of the shortage of oxalic acid. In other words, the excess loadings of Fe did not affect the chemistry of dissolution. It should be noted that the maximum total Fe concentration was not caused by the solubility of iron oxalates in water. In a preliminary experiment, the solubility of Fe(III) oxalate ($Fe_2(C_2O_4)_3 \cdot 6H_2O$) was confirmed to be over 1.0 mol-Fe/L. Indeed, **Tables S2-1-S2-3** contained experimental data that showed total Fe concentrations over 0.27 mol/L. It was seen from **Figure 2-8** (b) that Fe^{3+}/Fe^{2+} ratio in all cases was around 2, and the ratio was

unchanged by the loaded Fe at the full dissolution with 0.5 mol/L oxalic acid. This result agrees with **Figure 2-5** (b), where Fe^{2+}/Fe^{3+} approaches around 0.5 with a decrease in OxA/Fe.
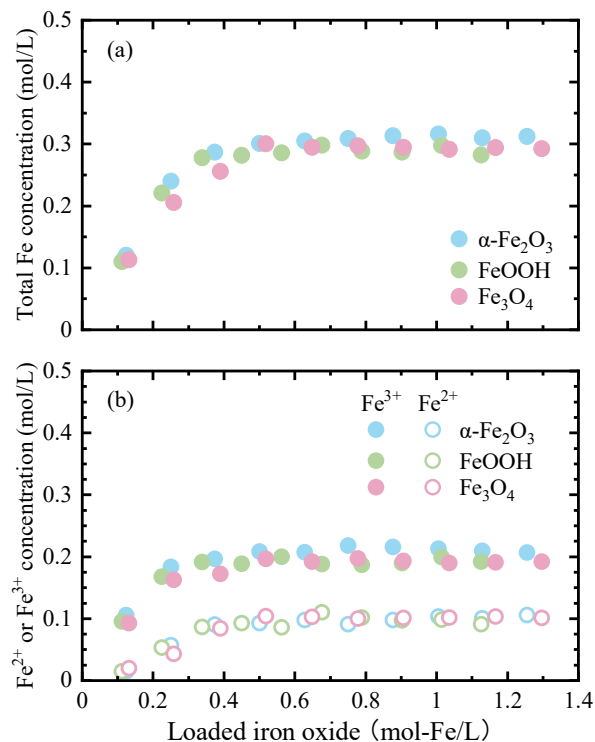
Figure 2-8. Total Fe, Fe^{2+} and Fe^{3+} concentrations plotted against iron oxide loaded in the solution in the experiments with 0.5 mol/L oxalic acid and 0.05–1.3 mol-Fe/L loaded iron oxide at 90 °C for 360 min.

2.3.5 Analysis of precipitates in the dissolution of Fe₃O₄

Three types of iron oxides, examined in this study, showed similar trends in most experimental results, but the faster dissolution rate and lower Fe dissolution of Fe_3O_4 was the exception. The difference was caused by the presence of Fe(II) in the structure of Fe_3O_4. A facile and quick release of catalytic Fe(II) oxalate results in the fast dissolution of overall Fe_3O_4 as reported in literature. [21] On the other hand, the formation of precipitates was assumed by Eq. 2.8 in this study. To confirm the occurrence of Eq. 2.8, precipitates recovered from the dissolution at different OxA/Fe at 90 °C were analyzed by XRD. As shown in **Figure 2-9**, all

the precipitates had a monoclinic structure of Humboldtine, $FeC_2O_4 \cdot 2H_2O$, although higher crystallinity was observed for the precipitates generated at OxA > 2.
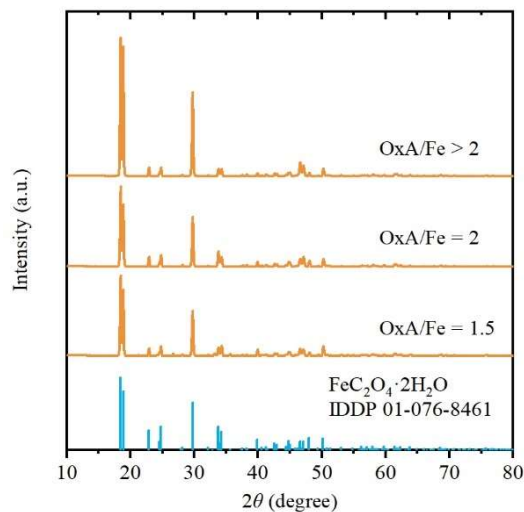
Figure 2-9. XRD patterns of precipitates obtained from the dissolution of Fe_3O_4 at 90 °C for 360 min with different OxA/Fe.

In our scheme of iron-making using oxalic acid [22], $FeC_2O_4 \cdot 2H_2O$ is prepared by photochemical reduction of Fe(III) oxalate in the solution and used as a direct feedstock for producing metallic iron by its pyrolytic reduction. The formation of $FeC_2O_4 \cdot 2H_2O$ without the need of a photochemical reduction step and as its fast dissolution rate seems like an advantage of Fe_3O_4 over $\alpha\text{-}Fe_2O_3$ and FeOOH. However, when Fe_3O_4 contained in natural iron ore is used as feedstock, a difficulty is found in the separation of precipitated $FeC_2O_4 \cdot 2H_2O$ from the dissolution residue consisting mainly of metals other than iron. The use of $FeC_2O_4 \cdot 2H_2O$ mixed with other metals for pyrolytic reduction results in the production of low-quality iron with impurities. When the precipitates are not considered as the feedstock of metallic iron in consideration of this issue, 10–20% of the iron in Fe_3O_4 is lost in the dissolution. On the other hand, as experimentally evidenced in the present study, Fe_2O_3 and FeOOH are recovered, with

little loss in the dissolution, as Fe(III) oxalates and Fe^{2+} in the aqueous solution, which are subjected to photochemical reduction to produce $FeC_2O_4\cdot2H_2O$ with a near-complete recovery.

2.4 Conclusions

The dissolution of iron oxides was studied to reveal the chemistry under various conditions with a particular purpose for its application to iron-making. The experimental results demonstrated that Fe concentration of over 0.5 mol/L could be achieved by the dissolution. Among iron oxides tested, Fe_3O_4 showed a distinguished fast dissolution, completing within 30 min even at 75 °C, due to the facile and fast release of catalytic Fe(II) oxalate. A drawback of Fe_3O_4 as a feedstock of the iron-making was the formation of $FeC_2O_4\cdot2H_2O$ precipitates, which accounted for 10–20% of the iron in the feedstock, during the dissolution. Near-complete dissolution was confirmed for Fe_2O_3 and FeOOH. On the other hand, highly acidic oxalic acid for preparing the high concentration iron oxalate solution resulted in the predominant occurrence of non-reductive dissolution independently of the type of iron oxides. Fe dissolution under various conditions could be described by a single line when plotted against a factor represented by proton concentration, which was indicated by the occurrence of non-reductive dissolution. This correlation also revealed the required minimum OxA/Fe for achieving the maximum Fe dissolution. The detailed analysis of dissolved iron species and suggested stoichiometries evidenced that Fe^{3+} and Fe^{2+} presented mainly as $[Fe^{3+}HC_2O_4]^{2+}$ and Fe^{2+} in the solution, respectively, but other iron species such as $[Fe^{3+}(C_2O_4)_2]^-$ was possibly involved in the solution when oxalates were not sufficiently provided, i.e., at OxA/Fe lower than the required minimum.

2.5 References

[1] Gerald, O.; Christopher, N.; Ayebatonworio, O.; Martin, O. Comparative Kinetics of Iron Ore Dissolution in Aqueous HCl-HNO$_3$ System. J. Miner. Mater. Charact. Eng. 2013, 01 (04), 153–159. https://doi.org/10.4236/jmmce.2013.14026.

[2] Martínez-Luévanos, A.; Rodríguez-Delgado, M. G.; Uribe-Salas, A.; Carrillo-Pedroza, F. R.; Osuna-Alarcón, J. G. Leaching Kinetics of Iron from Low Grade Kaolin by Oxalic Acid Solutions. Appl. Clay Sci. 2011, 51 (4), 473–477. [3] Tuncuk, A.; Akcil, A. Iron Removal in Production of Purified Quartz by Hydrometallurgical Process. Int. J. Miner. Process. 2016, 153, 44–50. https://doi.org/10.1016/j.minpro.2016.05.021.

[4] Cornell, R. M.; Posner, A. M.; Quirk, J. P. Kinetics and Mechanisms of the Acid Dissolution of Goethite (α-FeOOH). J. Inorg. Nucl. Chem. 1976, 38 (3), 563–567. https://doi.org/10.1016/0022-1902(76)80305-3.

[5] Salmimies, R.; Kallas, J.; Ekberg, B.; Häkkinen, A. Oxalic Acid Regeneration of Ceramic Filter Medium Used in the Dewatering of Iron Ore. ISRN Chem. Eng. 2012, 2012, 1–6.

[6] Salmimies, R.; Mannila, M.; Kallas, J.; Häkkinen, A. Acidic Dissolution of Hematite: Kinetic and Thermodynamic Investigations with Oxalic Acid. Int. J. Miner. Process. 2012, 110–111, 121–125. https://doi.org/10.1016/j.minpro.2012.04.001.

[7] Pariyan, K.; Hosseini, M. R.; Ahmadi, A.; Zahiri, A. Optimization and Kinetics of Oxalic Acid Treatment of Feldspar for Removing the Iron Oxide Impurities. Sep. Sci. Technol. 2019, 0 (0), 1–12. https://doi.org/10.1080/01496395.2019.1612913.

[8] Ambikadevi, V. R.; Lalithambika, M. Effect of Organic Acids on Ferric Iron Removal from Iron-Stained Kaolinite. Appl. Clay Sci. 2000, 16 (3–4), 133–145.

CHAPTER 2

[9] Yang, Y.; Wang, X.; Wang, M.; Wang, H.; Xian, P. Recovery of Iron from Red Mud by Selective Leach with Oxalic Acid. Hydrometallurgy 2015, 157, 239–245. https://doi.org/10.1016/j.hydromet.2015.08.021.

[10] Hernández, R. Á. H.; García, F. L.; Cruz, L. E. H.; Luévanos, A. M. Statistical Treatment of Bleaching Kaolin by Iron Removal. J. Mex. Chem. Soc. 2013, 57 (4), 261–266.

[11] Verma, A.; Kore, R.; Corbin, D. R.; Shiflett, M. B. Metal Recovery Using Oxalate Chemistry: A Technical Review. Ind. Eng. Chem. Res. 2019, 58 (34), 15381–15393. https://doi.org/10.1021/acs.iecr.9b02598.

[12] Lee, S. O.; Tran, T.; Park, Y. Y.; Kim, S. J.; Kim, M. J. Study on the Kinetics of Iron Oxide Leaching by Oxalic Acid. Int. J. Miner. Process. 2006, 80 (2–4), 144–152. https://doi.org/10.1016/j.minpro.2006.03.012.

[13] Panias, D.; Taxiarchou, M.; Paspaliaris, I.; Kontopoulos, A. Mechanisms of Dissolution of Iron Oxides in Aqueous Oxalic Acid Solutions. Hydrometallurgy 1996, 42 (2), 257–265. https://doi.org/10.1016/0304-386X(95)00104-O.

[14] Taxiarchou, M.; Panias, D.; Douni, I.; Paspaliaris, I.; Kontopoulos, A. Removal of Iron from Silica Sand by Leaching with Oxalic Acid. Hydrometallurgy 1997, 46 (1–2), 215–227. https://doi.org/10.1016/s0304-386x(97)00015-7.

[15] Cornell, R. M.; Schindler, P. W. Photochemical Dissolution of Goethite in Acid/Oxalate Solution. Clays Clay Miner. 1987, 35 (5), 347–352. [16] Lee, S. O.; Tran, T.; Jung, B. H.; Kim, S. J.; Kim, M. J. Dissolution of Iron Oxide Using Oxalic Acid. Hydrometallurgy 2007, 87 (3–4), 91–99. [17] Panias, D.; Taxiarchou, M.; Douni, I.; Paspaliaris, I.; Kontopoulos, A. Thermodynamic Analysis of the Reactions of Iron Oxides: Dissolution in Oxalic Acid. Can. Metall. Q. 1996, 35 (4), 363–373. https://doi.org/10.1179/cmq.1996.35.4.363.

[18] Sultana, U. K.; Gulshan, F.; Kurny, A. S. W. Kinetics of Leaching of Iron Oxide in Clay in Oxalic Acid and in Hydrochloric Acid Solutions. Mater. Sci. Metall. Eng. 2014, 2 (1), 5–10. https://doi.org/10.12691/msme-2-1-2.

[19] Lee, S.-O.; Kim, W.-T.; Oh, J.-K.; Shin, B.-S. Iron-Removal of Clay Mineral with Oxalic Acid. Shigen-to-Sozai 1997, 113 (11), 847–851. https://doi.org/10.2473/shigentosozai.113.847.

[20] Jena, S. K.; Singh, S.; Rao, D. S.; Dhawan, N.; Misra, P. K.; Das, B. Characterization and Removal of Iron from Pyrophyllite Ore for Industrial Applications. Miner. Metall. Process. 2015, 32 (2), 102–110. https://doi.org/10.1007/bf03402427.

[21] Salmimies, R.; Mannila, M.; Kallas, J.; Häkkinen, A. Acidic Dissolution of Magnetite: Experimental Study on the Effects of Acid Concentration and Temperature. Clays Clay Miner. 2011, 59 (2), 136–146. https://doi.org/10.1346/CCMN.2011.0590203.

[22] Santawaja, P.; Kudo, S.; Mori, A.; Tahara, A.; Asano, S.; Hayashi, J. Sustainable Iron-Making Using Oxalic Acid: The Concept, A Brief Review of Key Reactions, and An Experimental Demonstration of the Iron-Making Process. ACS Sustain. Chem. Eng. 2020, 8 (35), 13292–13301. https://doi.org/10.1021/acssuschemeng.0c03593.

[23] Taxiarchou, M.; Panias, D.; Douni, I.; Paspaliaris, I.; Kontopoulos, A. Dissolution of Hematite in Acidic Oxalate Solutions. Hydrometallurgy 1997, 44 (3), 287–299. https://doi.org/10.1016/s0304-386x(96)00075-8.

[24] Legorreta-García, F.; Salinas-Rodríguez, E.; Hernández-Cruz, L. E.; Hernández-Hernández, R. A.; Eduardo Cerecedo S. Kinetics Study of Iron Leaching from Kaolinitic Clay Using Oxalic Acid. Eur. Sci. J. 2015, 11 (12), 12–23.

[25] Cwiertny, D. M.; Hunter, G. J.; Pettibone, J. M.; Scherer, M. M.; Grassian, V. H. Surface Chemistry and Dissolution of &FeOOH Nanorods and Microrods: Environmental

Implications of Size-Dependent Interactions with Oxalate. J. Phys. Chem. C 2009, 113 (6), 2175–2186. https://doi.org/10.1021/jp807336t.

[26] Dudeney, A. W. L.; Tarasova, I. I. Photochemical Decomposition of Trisoxalatoiron(III): A Hydrometallurgical Application of Daylight. Hydrometallurgy 1998, 47, 243–257. https://doi.org/10.1016/s0304-386x(97)00049-2.

[27] Blesa, M. A.; Marinovich, H. A.; Baumgartner, E. C.; Maroto, A. J. G. Mechanism of Dissolution of Magnetite by Oxalic Acid-Ferrous Ion Solutions. Inorg. Chem. 1987, 26 (22), 3713–3717. https://doi.org/10.1021/ic00269a019.

[28] Lee, S.-O.; Oh, J.-K.; Shin, B.-S. Dissolution of Iron Oxide Rust Materials Using Oxalic Acid. Shigen-to-Sozai 1999, 115 (11), 815–819.

[29] Xu, N.; Gao, Y. Characterization of Hematite Dissolution Affected by Oxalate Coating, Kinetics and pH. Appl. Geochemistry 2008, 23 (4), 783–793. https://doi.org/10.1016/j.apgeochem.2007.12.026.

[30] Zinder, B.; Furrer, G.; Stumm, W. The Coordination Chemistry of Weathering: II. Dissolution of Fe(III) Oxides. Geochim. Cosmochim. Acta 1986, 50 (9), 1861–1869. https://doi.org/10.1016/0016-7037(86)90244-9.

[31] Schwertmann, U. Solubility and Dissolution of Iron Oxides. Plant Soil 1991, 130 (1–2), 1–25. https://doi.org/10.1007/BF00011851.

[32] Sulzberger, B.; Suter, D.; Siffert, C.; Banwart, S.; Stumm, W. Dissolution of Fe(Iii)(Hydr)Oxides in Natural Waters; Laboratory Assessment on the Kinetics Controlled by Surface Coordination. Mar. Chem. 1989, 28 (1–3), 127–144. https://doi.org/10.1016/0304-4203(89)90191-6.

[33] Jeong, D.; Kim, K.; Choi, W. Accelerated Dissolution of Iron Oxides in Ice. Atmos. Chem. Phys. 2012, 12 (22), 11125–11133. https://doi.org/10.5194/acp-12-11125-2012.

2.6 Supporting information
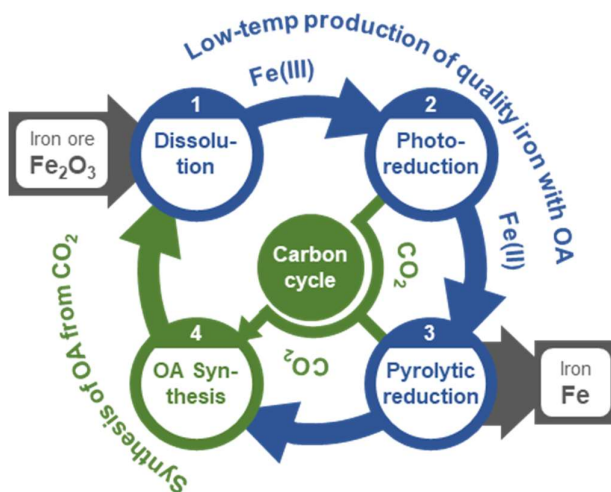
Figure S2-1. Concept of the proposed sustainable iron-making process. OA: oxalic acid. (Santawaja et al. 2020).
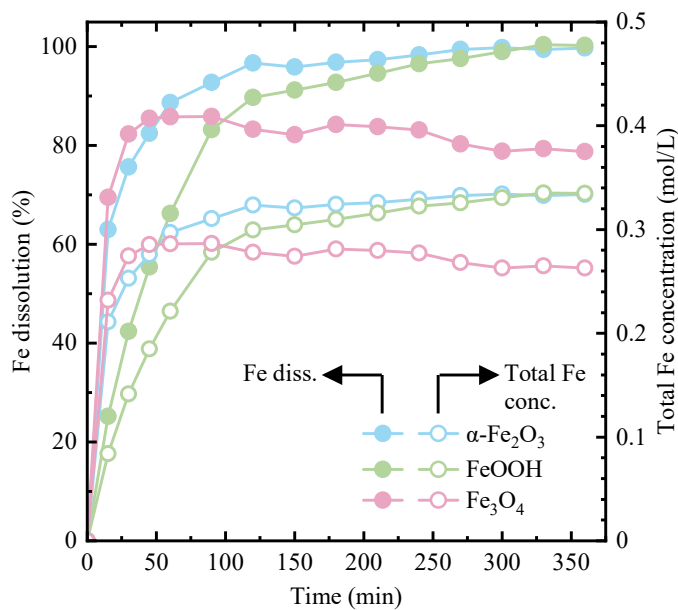
Figure S2-2 Time-dependent change of Fe dissolution and total Fe concentration at 90 °C for 360 min. Conditions: 0.33 mol-Fe/L loaded iron oxide and 0.67 mol/L oxalic acid.

Table S2-1. Dissolution of α-Fe_2O_3 with different feedstock loadings at 90 °C for 360 min.

Feedstock				Dissolved Fe (mol/L)			Feedstock				Dissolved Fe (mol/L)		
Fe	OxA	OxA/Fe	Fe diss[a]				Fe	OxA	OxA/Fe	Fe diss[a]			
(mol/L)	(mol/L)	(–)	(%)	Total	Fe^{3+}	Fe^{2+}	(mol/L)	(mol/L)	(–)	(%)	Total	Fe^{3+}	Fe^{2+}
0.07	0.10	1.5	74	0.05	0.04	0.01	0.42	0.50	1.2	68	0.28	0.20	0.08
0.10	0.20	2.0	95	0.09	0.08	0.02	0.42	0.75	1.8	88	0.37	0.29	0.07
0.10	0.30	3.0	99	0.10	0.09	0.01	0.50	0.50	1.0	61	0.30	0.21	0.10
0.10	0.40	4.0	100	0.10	0.09	0.01	0.50	0.70	1.4	81	0.41	0.29	0.11
0.10	0.50	5.0	100	0.10	0.09	0.01	0.50	0.75	1.5	84	0.42	0.31	0.11
0.10	0.60	6.0	99	0.10	0.10	0.00	0.50	1.00	2.0	96	0.48	0.37	0.11
0.10	0.80	8.0	100	0.10	0.10	0.00	0.53	0.80	1.5	83	0.44	0.32	0.12
0.10	1.00	10.0	99	0.10	0.10	0.00	0.58	0.75	1.3	70	0.41	0.30	0.11
0.13	0.50	3.9	96	0.12	0.11	0.01	0.60	0.90	1.5	78	0.47	0.37	0.10
0.13	0.75	5.9	96	0.12	0.11	0.01	0.63	0.50	0.8	49	0.30	0.21	0.10
0.13	1.00	8.0	95	0.12	0.11	0.01	0.63	0.75	1.2	69	0.44	0.32	0.12
0.14	0.20	1.5	82	0.11	0.08	0.03	0.63	1.00	1.6	79	0.49	0.39	0.11
0.17	0.50	3.0	99	0.17	0.14	0.02	0.67	1.00	1.5	78	0.52	0.40	0.13
0.20	0.30	1.5	83	0.17	0.13	0.04	0.75	0.50	0.7	41	0.31	0.22	0.09
0.20	0.50	2.5	100	0.20	0.17	0.03	0.75	0.75	1.0	59	0.44	0.32	0.12
0.22	0.50	2.2	100	0.22	0.17	0.05	0.75	1.00	1.3	72	0.54	0.40	0.15
0.25	0.50	2.0	89	0.22	0.19	0.04	0.88	0.50	0.6	36	0.31	0.22	0.10
0.25	0.75	3.0	95	0.24	0.21	0.03	0.88	0.75	0.9	51	0.45	0.32	0.13
0.25	1.00	4.0	94	0.23	0.21	0.03	0.88	1.00	1.1	63	0.55	0.39	0.16
0.27	0.40	1.5	86	0.23	0.16	0.07	1.00	0.75	0.7	45	0.45	0.32	0.13
0.33	0.50	1.5	87	0.29	0.20	0.09	1.00	1.00	1.0	55	0.56	0.39	0.16
0.33	0.67	2.0	100	0.32	0.25	0.08	1.01	0.50	0.5	31	0.32	0.21	0.10
0.33	0.75	2.2	99	0.33	0.24	0.08	1.13	0.50	0.4	27	0.31	0.21	0.10
0.34	0.67	2.0	98	0.33	0.26	0.07	1.13	0.75	0.7	39	0.44	0.31	0.13
0.38	1.00	2.7	90	0.34	0.29	0.05	1.13	1.00	0.9	48	0.54	0.39	0.15
0.38	0.50	1.3	74	0.28	0.21	0.07	1.25	0.75	0.6	36	0.45	0.32	0.13
0.38	0.75	2.0	88	0.33	0.27	0.06	1.25	1.00	0.8	43	0.54	0.39	0.15
0.40	0.60	1.5	83	0.33	0.24	0.10	1.26	0.50	0.4	25	0.31	0.21	0.11

[a] Fe dissolution.

Table S2-2. Dissolution of FeOOH with different feedstock loadings at 90 °C for 360 min.

Feedstock				Dissolved Fe (mol/L)			Feedstock				Dissolved Fe (mol/L)		
Fe	OxA	OxA/Fe	Fe diss[a]	Total	Fe^{3+}	Fe^{2+}	Fe	OxA	OxA/Fe	Fe diss[a]	Total	Fe^{3+}	Fe^{2+}
(mol/L)	(mol/L)	(–)	(%)				(mol/L)	(mol/L)	(–)	(%)			
0.05	0.20	4.0	97	0.05	0.05	0.00	0.45	0.75	1.7	86	0.39	0.29	0.10
0.05	0.30	6.0	99	0.05	0.05	0.00	0.45	1.00	2.2	99	0.45	0.36	0.09
0.05	0.40	8.0	99	0.05	0.05	0.00	0.47	0.70	1.5	88	0.41	0.29	0.12
0.05	0.50	10.0	98	0.05	0.05	0.00	0.49	0.50	1.0	64	0.31	0.21	0.11
0.07	0.10	1.5	82	0.06	0.04	0.01	0.50	0.50	1.0	62	0.31	0.21	0.10
0.11	0.50	4.4	97	0.11	0.10	0.01	0.50	0.75	1.5	86	0.43	0.31	0.12
0.11	0.75	6.7	98	0.11	0.10	0.01	0.50	0.75	1.5	91	0.46	0.32	0.14
0.11	1.00	8.8	100	0.11	0.11	0.01	0.50	1.00	2.0	97	0.49	0.37	0.11
0.13	0.20	1.5	88	0.12	0.08	0.03	0.53	0.80	1.5	86	0.46	0.32	0.14
0.17	0.50	3.0	100	0.17	0.14	0.02	0.56	0.50	0.9	51	0.29	0.20	0.09
0.20	0.30	1.5	89	0.18	0.12	0.06	0.56	1.00	1.8	98	0.55	0.42	0.13
0.20	0.50	2.5	100	0.20	0.17	0.04	0.60	0.90	1.5	86	0.52	0.37	0.15
0.22	0.50	2.2	100	0.22	0.17	0.05	0.67	1.00	1.5	81	0.54	0.40	0.14
0.23	0.50	2.2	98	0.22	0.17	0.05	0.68	0.50	0.7	44	0.30	0.19	0.11
0.23	0.75	3.3	97	0.22	0.19	0.03	0.68	0.75	1.1	68	0.46	0.32	0.14
0.23	1.00	4.4	100	0.23	0.21	0.02	0.68	1.00	1.5	81	0.55	0.40	0.15
0.25	0.50	2.0	100	0.25	0.20	0.05	0.79	0.50	0.6	37	0.29	0.19	0.10
0.27	0.40	1.5	89	0.24	0.16	0.08	0.79	0.75	1.0	56	0.44	0.32	0.12
0.30	0.50	1.7	96	0.29	0.21	0.08	0.79	1.00	1.3	68	0.54	0.39	0.14
0.33	0.50	1.5	91	0.30	0.21	0.10	0.90	0.50	0.6	32	0.29	0.19	0.10
0.33	0.67	2.0	100	0.33	0.29	0.05	0.90	0.75	0.8	48	0.43	0.32	0.11
0.33	0.75	2.2	96	0.32	0.24	0.08	0.90	1.00	1.1	58	0.52	0.40	0.12
0.34	0.50	1.5	82	0.28	0.19	0.09	1.01	0.75	0.7	40	0.40	0.30	0.10
0.34	0.75	2.2	93	0.31	0.25	0.06	1.01	1.00	1.0	49	0.49	0.38	0.12
0.34	1.00	3.0	100	0.34	0.29	0.04	1.02	0.50	0.5	29	0.30	0.20	0.10
0.38	0.75	2.0	94	0.35	0.28	0.07	1.13	0.50	0.4	25	0.28	0.19	0.09
0.40	0.60	1.5	88	0.35	0.25	0.10	1.13	0.75	0.7	36	0.40	0.30	0.10
0.45	0.50	1.1	62	0.28	0.19	0.09	1.13	1.00	0.9	43	0.49	0.37	0.11

[a] Fe dissolution.

Table S2-3. Dissolution of Fe_3O_4 with different feedstock loadings at 90 °C for 360 min.

Feedstock				Dissolved Fe (mol/L)			Feedstock				Dissolved Fe (mol/L)		
Fe (mol/L)	OxA (mol/L)	OxA/Fe (–)	Fe diss[a] (%)	Total	Fe^{3+}	Fe^{2+}	Fe (mol/L)	OxA (mol/L)	OxA/Fe (–)	Fe diss[a] (%)	Total	Fe^{3+}	Fe^{2+}
0.07	0.10	1.5	94	0.06	0.04	0.02	0.50	0.50	1.0	55	0.27	0.19	0.09
0.13	0.20	1.5	94	0.13	0.09	0.04	0.50	0.75	1.5	68	0.34	0.25	0.09
0.13	0.50	3.8	85	0.11	0.09	0.02	0.50	1.00	2.0	71	0.36	0.29	0.07
0.13	0.75	5.8	90	0.12	0.11	0.01	0.52	0.50	1.0	58	0.30	0.20	0.10
0.13	1.00	7.6	91	0.12	0.11	0.01	0.52	0.75	1.4	70	0.36	0.26	0.10
0.15	0.20	1.3	81	0.12	0.08	0.04	0.52	1.00	1.9	74	0.38	0.32	0.06
0.15	0.25	1.7	95	0.14	0.10	0.04	0.53	0.80	1.5	72	0.39	0.29	0.09
0.15	0.30	2.0	88	0.13	0.11	0.03	0.60	0.90	1.5	70	0.42	0.32	0.10
0.15	0.40	2.7	86	0.13	0.11	0.02	0.65	0.50	0.8	45	0.29	0.19	0.10
0.15	0.50	3.3	87	0.13	0.12	0.01	0.65	0.75	1.2	61	0.40	0.28	0.12
0.15	0.60	4.0	88	0.13	0.12	0.01	0.65	1.00	1.5	70	0.45	0.35	0.10
0.15	0.80	5.3	88	0.13	0.12	0.01	0.67	1.00	1.5	68	0.46	0.35	0.11
0.15	1.00	6.7	87	0.13	0.13	0.00	0.78	0.50	0.6	38	0.30	0.20	0.10
0.17	0.50	3.0	83	0.14	0.12	0.02	0.78	0.75	1.0	51	0.40	0.28	0.12
0.20	0.30	1.5	82	0.16	0.11	0.05	0.78	1.00	1.3	64	0.50	0.34	0.15
0.20	0.50	2.5	82	0.16	0.14	0.03	0.91	0.50	0.6	32	0.29	0.19	0.10
0.25	0.50	2.0	83	0.21	0.17	0.04	0.91	0.75	0.8	41	0.37	0.26	0.12
0.26	0.50	1.9	80	0.21	0.16	0.04	0.91	1.00	1.1	55	0.50	0.34	0.16
0.26	0.75	2.9	86	0.23	0.20	0.03	1.04	0.50	0.5	28	0.29	0.19	0.10
0.26	1.00	3.8	85	0.22	0.20	0.02	1.04	0.75	0.7	37	0.38	0.25	0.13
0.27	0.40	1.5	83	0.22	0.16	0.06	1.04	1.00	1.0	49	0.50	0.34	0.17
0.33	0.50	1.5	81	0.27	0.20	0.07	1.17	0.50	0.4	25	0.29	0.19	0.10
0.33	0.67	2.0	78	0.26	0.21	0.05	1.17	0.75	0.6	33	0.38	0.26	0.13
0.39	0.50	1.3	66	0.26	0.17	0.08	1.17	1.00	0.9	43	0.50	0.33	0.17
0.39	0.75	1.9	79	0.31	0.25	0.06	1.30	0.50	0.4	23	0.29	0.19	0.10
0.39	1.00	2.6	80	0.31	0.27	0.04	1.30	0.75	0.6	29	0.37	0.25	0.12
0.40	0.60	1.5	80	0.32	0.24	0.08	1.30	1.00	0.8	35	0.46	0.31	0.15
0.47	0.70	1.5	74	0.35	0.26	0.09							

[a] Fe dissolution.

# CHAPTER 3

Photochemical Reduction of Iron(III) Oxalate

3.1 Introduction

The photochemistry of Fe(III) oxalate to be converted into Fe(II) oxalate has been studied since the 1950s in relation to its absorption characteristics. [1-16] Its strong ligand-to-metal charge transfers are responsible for its unique photochemical properties upon excitation within the tropospheric solar UV-visible region (290–570 nm). [1,2,8-11] Due to its photochemical reactivity, Fe(III) oxalate is widely used as a chemical actinometer to measure light intensities in aqueous solution with high selectivity and precision under well-defined conditions. [12,13] The Fe(III) oxalate also works as a catalyst or promotor in the photodegradation and mineralization of dyes in water. [8,9] As mentioned above, light irradiation and the resulting photochemical reduction are used to promote the dissolution of iron with oxalic acid, which is called photoreductive dissolution [5] or photochemical dissolution. [6]

Fe(III) oxalate presents in water in several forms such as $[Fe(C_2O_3)]^+$, $[Fe(C_2O_4)_2]^-$ and $[Fe(C_2O_4)_3]^{3-}$, depending on the pH and ratio of Fe(III) to oxalate. [14] Among them, $[Fe(C_2O_4)_3]^{3-}$ is usually cited in the photochemical reduction, and the reaction is expressed in Eq. 3.1. [2,11,14,15]

$$2[Fe(C_2O_4)_3]^{3-} + h\nu \rightarrow 2[Fe(C_2O_4)_2]^{2-} + 2CO_2 + C_2O_4^{2-} \qquad \text{Eq. 3.1}$$
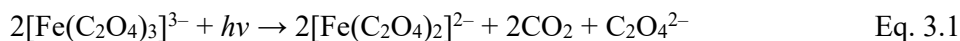
Although the mechanistic aspect of photolysis of Fe(III) oxalate is still under discussion, studies have revealed the reaction pathway, demonstrating that the absorption of photons causes not only the reduction of Fe(III) to Fe(II), but also the generation of reactive radicals such as $CO_2^{\bullet-}$ and $C_2O_4^{\bullet-}$ and that the radicals contribute to further reduction of Fe(III). [3,4,14,15] In an early stage of photochemical reduction, the crystals of Fe(II) oxalate

dihydrate, $FeC_2O_4 \cdot 2H_2O$, start to precipitate due to their very low solubility in water (ca. 22 mg/L). [2] Fe(II) oxalate dihydrate has two chemical forms, α-form and β-form, determined by precipitation conditions. The α-form known as Humboldtite has a monoclinic structure, which is commonly observed in the presence of excess oxalic acid. [16] The stoichiometric ratio of oxalic acid and Fe(II) results in the β-form which has an orthorhombic structure. [6]

The rate of photochemical reaction is generally slow, which is not suitable for mass production. On the other hand, the quantum efficiency of photochemical reduction of Fe(III) oxalate is reported to be approximately unity over wavelengths in the range 250–490 nm. [6] This is encouraging for the present process. The rate of reduction is enhanced simply by the enlargement of the solution's surface exposed to light, though the rate is also affected by light intensity.

With the aim of utilization of the characteristic of iron oxalate complex for the proposed iron-making process, therefore, in this study, the photochemical reduction of the obtained iron oxalate aqueous solution from the dissolution of iron oxides were investigated by using the natural sunlight, simulated sunlight and LED light as a light source. Moreover, the parameters which may affect the rate of photochemical reduction for example, light intensity, solution depth, and additives were determined by using simulated sunlight.

3.2 Materials and methods

3.2.1 Materials

α-Fe_2O_3 and Fe_3O_4 were purchased from Sigma-Aldrich. Iron oxalate aqueous solutions obtained from the iron oxides dissolution with oxalic acid at 92 °C for 6 h were used as an iron precursor for the photochemical reduction. 1,10-phenanthroline (Aldrich), ammonium acetate (Wako Pure Chemical), and hydroxylamine (Wako Pure Chemical) were used for quantification of dissolved iron.

The obtained iron oxalate aqueous solutions from α-Fe_2O_3, and Fe_3O_4 are hereafter denoted by DS-Fe_2O_3 and DS-Fe_3O_4, respectively.

In this study, three different light sources (natural sunlight, simulated sunlight, and LED lights) were used to irradiate the iron oxalate aqueous solutions. For natural sunlight, the experiment carried out during the daytime on September 29 – October 1, 2020 at Kyushu University, Fukuoka, Japan. The simulated sunlight in the range of 380-780 nm was produced from a solar simulator (Asahi spectra, HAL-320, Japan). The LED lights centered at 365, 435, 525, and 730 nm were generated from a LED light source (ASAHI SPECTRA, CL-1501). The illuminance, light intensity, and photon flux density were measured using a light analyzer (NK System, LA-105).

3.2.2 Photochemical reduction

An open-top cylindrical glass container with an inner diameter of 5 cm was used as a reactor for photochemical reduction experiments using natural sunlight, while the experiments with LEDs light were performed in an open-top cylindrical glass container with an inner diameter of 2.5 cm. The experiments using simulated sunlight and LED light were carried out in a dark room to eliminate the effect of stray light, while the experiment using natural sunlight was performed outside the building in order to allow reactor to fully expose to the sunlight. During the reaction, 30 µL of solution was sampled at predetermined times to measure the concentration of the remaining dissolved Fe by absorption spectroscopy until the completion of the reaction was observed. After that, the ferrous oxalate precipitate was filtrated, washed with distilled water, and dried overnight at 60 ℃, while the supernatant was collected for analysis of the remaining dissolved iron.

3.2.2.1 Photochemical reduction using simulated sunlight

CHAPTER 3

Iron oxalate aqueous solution was added to the reactor and then irradiated by simulated sunlight with a beam diameter as 5x5 cm under atmospheric conditions with continuous stirring. The photos of the simulated sunlight experiment set-up and its beam size are shown in **Figure 3-1.**
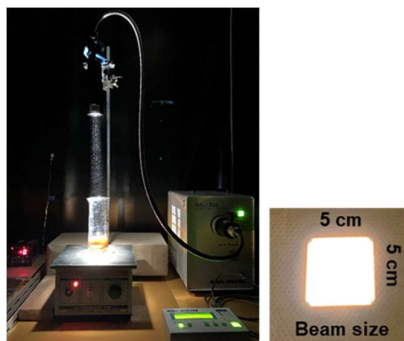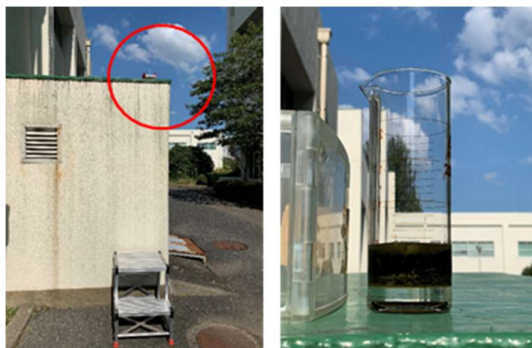

Figure 3-1. Photos of photochemical reduction using simulated sunlight experiment

A simulated sunlight with a photon flux density (PFD) as 4274 μmol/m^2/s, that is equal to photosynthetic photon flux density (PPFD) as 3170 μmol/m^2/s and illuminance as 180 klx, was used to investigate the effect of iron sources in iron oxalate aqueous solution (by using 90 ml of DS-Fe$_2$O$_3$ and DS-Fe$_3$O$_4$) and the depth of solution. In case of investigation of solution depth experiments, the volume of DS-Fe$_2$O$_3$, samples were varied as 90, 45, and 15 ml resulting in the solution height of 5, 2.5 and 0.9 cm, respectively. The 45 ml of DS-Fe$_2$O$_3$ was chosen to study the effect of light intensity at different PFD: 4274, 2550, and 1655 μmol/m^2/s, corresponding to illuminance about 180, 110, 70 klx, respectively.

3.2.2.2 Photochemical reduction using natural sunlight

45 mL of DS-Fe$_2$O$_3$ was added to the reactor and then placed outside the building to expose to the sunlight without stirring and controlling temperature. The photos of natural sunlight experiment are shown in **Figure 3-2.**
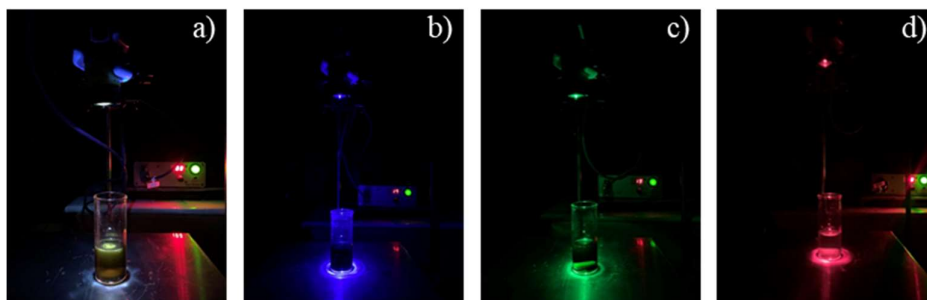
Figure 3-2. Photos of photochemical reduction using natural sunlight experiment

3.2.2.3 Photochemical reduction using LED lights

12 ml of DS-Fe$_2$O$_3$ was irradiated by different LED lights with a constant PFD (about 490 μmol/m^2/s) under atmospheric conditions with continuous stirring to investigate the effect of dominant wavelength on the rate of photochemical reduction. The set-up photos of LED light experiments are presented in **Figure 3-3**.

Figure 3-3. Photos of photochemical reduction using LED lights experiments: the LED centered at a) 365, b) 435, c)525, and d) 730 nm.

3.2.3 Characterizations

The concentration of iron dissolved in the solution was analyzed by absorption spectroscopy with a UV-Vis spectrophotometer (PerkinElmer, Lambda 365) that is in a similar manner to which described in Chapter 2 (also explained in **Appendix I**). The conversion to

CHAPTER 3

Fe(II) oxalate dihydrate (X_t) was calculated using Eq. 3.2 referring the concentration of total dissolved iron (C total dissolved iron) in solution.

$$X_t = \frac{C\ total\ dissolved\ Fe_{int} - C\ total\ dissolved\ Fe_t}{C\ total\ dissolved\ Fe_{int}} \times 100 \qquad \text{Eq. 3.2}$$

The phase analyses of the iron samples were performed by X-ray diffraction, XRD (a Rigaku TTR-III X-ray diffractometer with Cu K radiation at 50 kV and 30 mA). The morphology of iron samples was observed by Scanning Electron Microscope, SEM (a Keyence VE 9800 real 3D system).

3.3 Results and dissolution

3.3.1 Photochemical reduction using simulated sunlight

To investigate the parameters affecting the photochemical reduction of iron oxalate aqueous solution in this study, the simulated sunlight from Asahi spectra was used because it provided a wide spectrum of wavelengths ranging from ultraviolet to infrared similar as the natural sunlight. Moreover, it produced the stable light which can adjust the intensity and illuminance of light.

The relative irradiance of simulated sunlight and natural sunlight using in this experiment are presented in **Figure 3-4.**
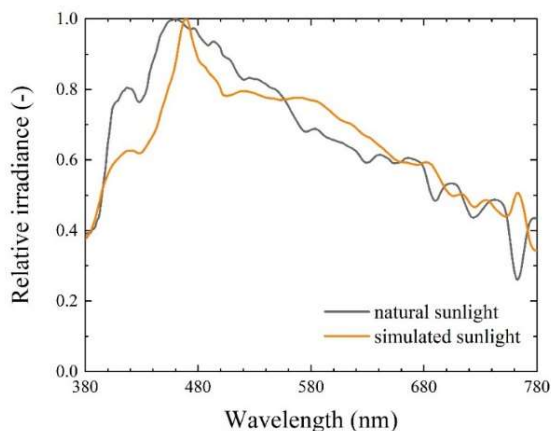
**Figure 3-4.** Relative irradiance spectra of natural and simulated sunlight.

3.3.1.1 Preliminaries study of photochemical reduction

In preliminary study, 90 ml of DS-Fe_2O_3 with a pH of 0.24 was exposed to a constant simulated sunlight with the photon flux density (PFD) of 4273 µmol/m^2/s and illuminance of 180 klx until the completion of reaction was observed. The initial concentrations of dissolved Fe^{2+}, Fe^{3+} and total Fe in this solution are 0.101, 0.383, and 0.485 mol/L, respectively. **Figure 3-5** illustrates the relationship between the dissolved Fe spices (Fe^{2+}, Fe^{3+} and total Fe) and percent of conversion to Fe(II) oxalate with the irradiation time together with the photos of iron oxalate aqueous solution at some specific times.

In this reaction, the Fe(III) oxalate complex in solution was reduced to Fe(II) oxalate dihydrate under the light illumination as presented in Eq. 3.3.

$$Fe_2(C_2O_4)_3 \text{ (aq)} + 4H_2O \rightarrow 2FeC_2O_4 \cdot 2H_2O \text{ (s)} + 2CO_2 \text{ (g)} \qquad \text{Eq. 3.3}$$
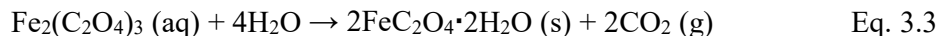
However, as can be seen in **Figure 3-5** that the iron was dissolved in the solution as Fe^{3+} or Fe^{2+}. They presented mainly in the forms of Fe(III) and Fe(II) oxalates, respectively, and Fe^{2+} was suggested to be a free divalent cation because it is a stable ion in a highly acidic aqueous solution(ref). As seen in the changes in Fe^{2+} and Fe^{3+} concentrations with time, the dissolved iron was completely recovered from the solution as the precipitated Fe(II) oxalate within 450 min, therefore, the presence of Fe^{2+}, which was not involved in the photochemical reduction outlined in Eq.3.3, did not disturb the iron recovery.
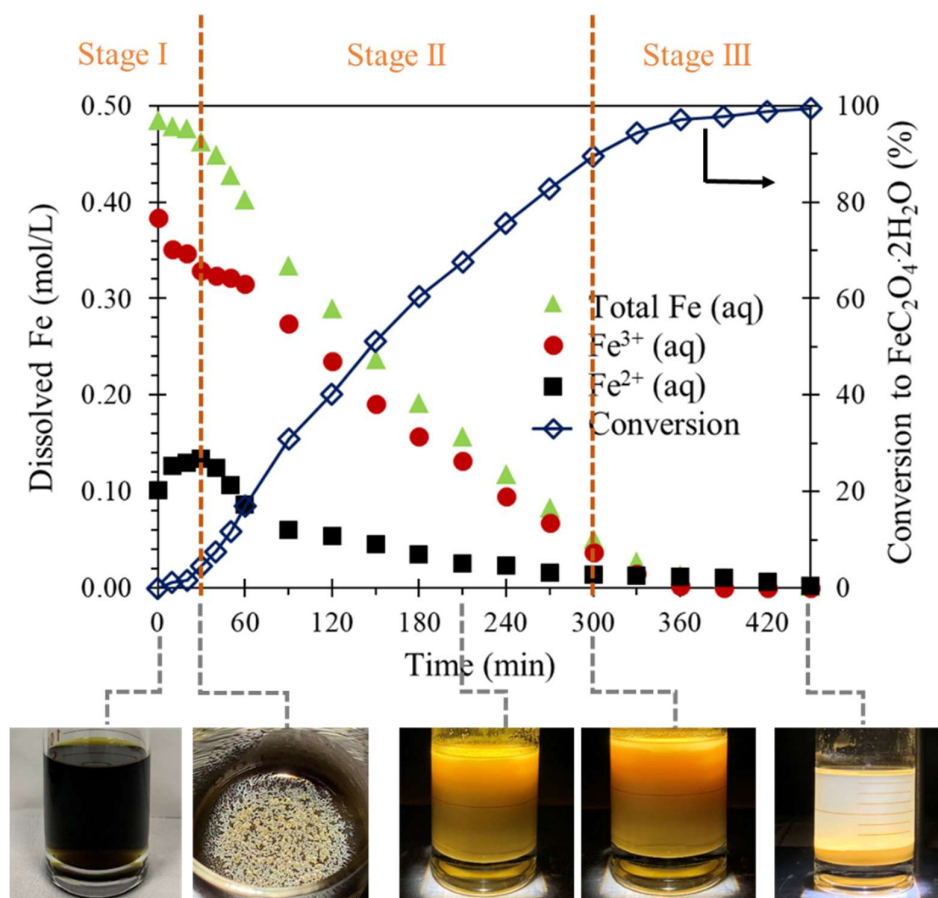
Figure 3-5. Photochemical reduction of DS-Fe$_2$O$_3$ using simulated sunlight with PFD of 4273 µmol/m^2/s and illuminance of 180 klx

Regarding the experiment, the conversion profile was simply separated into three stages. At the initial stage, Fe^{3+} was reduced to Fe^{2+}, but the precipitation of Fe(II) oxalate hardly occurred, rendering the slow rate of conversion. During the initial stage, the Fe^{3+}/Fe^{2+} ratio continued to decrease as shown in **Figure 3-5**. When the ratio reached around 2, the second stage, significant precipitation of Fe(II) oxalate was initiated on the top of solution, as presented in the **Figure 3-6**.
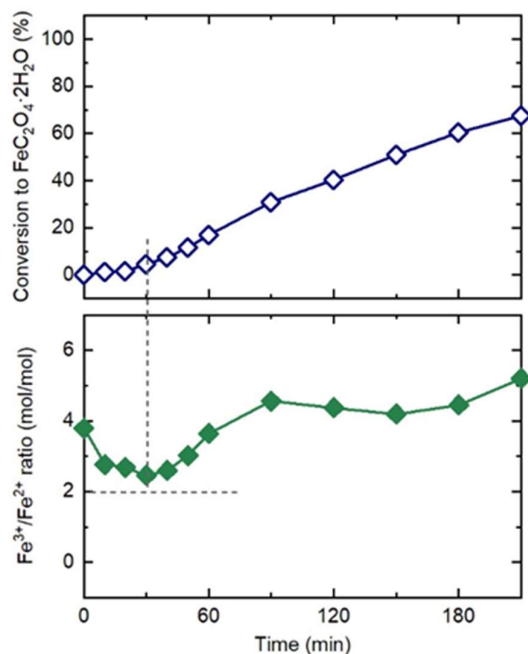
Figure 3-6. Time-dependent change of Fe^{3+}/Fe^{2+} ratio (bottom) in photochemical reduction.

The abundance of dissolved Fe^{2+} in the initial solution was, in this regard, rather beneficial because it contributed to shortening the duration of the initial stage. In the last stage of conversion, the solution was dense slurry consisting of diluted Fe(III) oxalate aqueous solution and Fe(II) oxalate particles, as can be seen in the photos in **Figure 3-5** and thereby the efficiency of light absorption was low, resulting in a decrease in the rate of conversion. Under this condition, the photochemical reduction of DS-Fe_2O_3 reached the completion in 450 min with a rate of conversion as 0.134 mol/min calculated in the second stage of the reduction. As can be seen from the photos in **Figure 3-5**, during the photochemical reduction, the color of the iron oxalate aqueous solution gradually changed from dark olive-green to yellow-green and then became colorless when the reduction was completed while the solution the final pH of solution was slightly increased to 0.71.

The obtained yellow iron oxalate precipitate was characterized by XRD and SEM, and the results are shown in **Figure 3-7**. The XRD pattern indexed to an orthorhombic structure of

FeC$_2$O$_4$·2H$_2$O (IDDP 01-075-7291) with no diffraction peaks due to other phases. From SEM image, it can see that the obtained FeC$_2$O$_4$·2H$_2$O has square rods structure with the diameter about 3.8 μm and length about 14 μm.
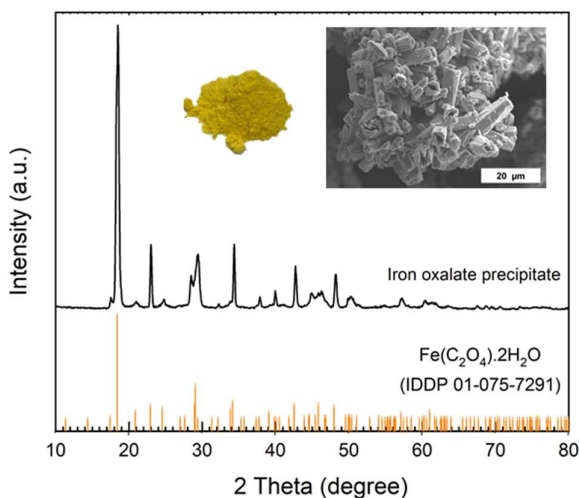
Figure 3-7 XRD pattern, SEM image and photo of the obtained iron oxalate precipitate by using simulated sunlight.

3.3.1.2 Effect of light intensity

To investigate the effect of light intensity on the rate of photochemical reduction of iron(III) oxalate aqueous solution, the 45 ml of DS-Fe$_2$O$_3$ samples with a solution depth of 2.5 cm were irradiated by the different intensities of simulated sunlight. The experimental data are listed in **Table 3-1**. The conversion to FeC$_2$O$_4$.2H$_2$O from DS-Fe$_2$O$_3$ samples irradiated by different light intensities are plotted in **Figure 3-8,** while the properties of simulated sunlight at these intensities are presented in **Table S3-1.**

The results showed that the intensity of simulated sunlight strongly affected the rate of photochemical reduction. Under the condition in this study, the conversion rate was approximately directly proportional to the of simulated sunlight intensity (in term of PFD). Higher light intensity provides a higher rate of conversion and resulted in a shortened time for completing the reaction. The conversion rates of DS-Fe$_2$O$_3$ samples under the irradiation of

simulated sunlight with PFD as 4273, 2550, 1655 μmol/m^2/s are 0.134, 0.086, 0.045 mol/min, respectively, calculated in the range of 20~80% conversion. Although the DS-Fe$_2$O$_3$_1 sample has the highest initial Fe concentration (0.495 mol-Fe/L), the reaction can be completed within 240 min with a conversion rate of 0.134 mol/min when the simulate sunlight with PFD of 4273 μmol/m^2/s was used. On the other hand, the DS-Fe$_2$O$_3$_3 sample which has the lowest initial Fe concentration required 600 min for completing the reduction with the lowest conversion rate of 0.045 mol/min.

Table 3-1. Experimental data of photochemical reduction of DS-Fe$_2$O$_3$ using simulated sunlight with different in light intensity

Sample name	Initial Fe concentration (mol/L)			PFD (μmol/m^2/s)	Illuminance (klx)	Time (min)	Rate (mol/min)
	Total Fe	Fe^{3+}	Fe^{2+}				
DS-Fe$_2$O$_3$_1	0.495	0.395	0.099	4273	180	240	0.134
DS-Fe$_2$O$_3$_2	0.485	0.368	0.117	2550	110	330	0.086
DS-Fe$_2$O$_3$_3	0.459	0.373	0.085	1655	70	600	0.047

It is worth to mentioned that these results are agreement with the report that the rate of conversion directly depends on the light intensity on the surface of solution. [2] In addition, although the intensity of simulated sunlight affected the rate of conversion, it did not show significant influence on the dissolved iron species in the solution as presented in **Figure 3-8**. The conversion profiles of all samples have the same trend: the concentration of dissolved Fe^{2+} gradually increased while the amount of dissolved Fe^{3+} decrease at the beginning of the reaction, which is same as observed in the preliminary results section.
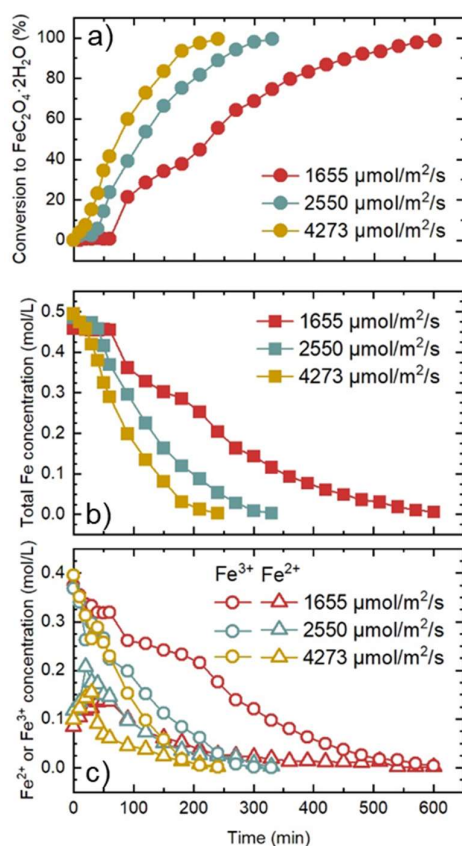
Figure 3-8. Time-dependent change of (a) conversion to $FeC_2O_4.2H_2O$, (b) Total Fe concentration and Fe^{2+} or Fe^{3+} concentration. Conditions: simulated sunlight with different intensities of simulated sunlight, room temperature, continuous stirring.

The obtained iron(II) oxalate precipitates was collected and characterized using XRD and SEM, as presented in **Figure 3-9.** The XRD patterns and the SEM images of the obtained iron(II) oxalate precipitates from $DS-Fe_2O_3$ samples by using different intensities of simulated sunlight are slightly different. From the XRD patterns, the iron(II) oxalate in all samples indexed to the $FeC_2O_4 \cdot 2H_2O$. However, the precipitates under irradiation by simulated sunlight with PFD of 4273 and 1655 $\mu mol/m^2/s$ were in the orthorhombic structure (IDDP 01-075-7291) while the one from PFD of 2550 $\mu mol/m^2/s$ corresponded to the monoclinic structure (Humboldtine, IDDP 01-076-8451). The faster in conversion rate may influence the crystallinity the $FeC_2O_4.2H_2O$ precipitate crystal. From the XRD patterns, the obtained

$FeC_2O_4.2H_2O$ by using the light with PDF of 4273 $\mu mol/m^2/s$, providing the highest conversion rate, showed the lowest crystallinity as evidenced by the lowest intensity in XRD patterns. The differences can also be observed in the SEM images, as can be seen in **Figure 3-9** that the orthorhombic structure of $FeC_2O_4 \cdot 2H_2O$ shows squared rods form while the monoclinic structure of $FeC_2O_4 \cdot 2H_2O$ obtained from has pyramidal-shaped particles.
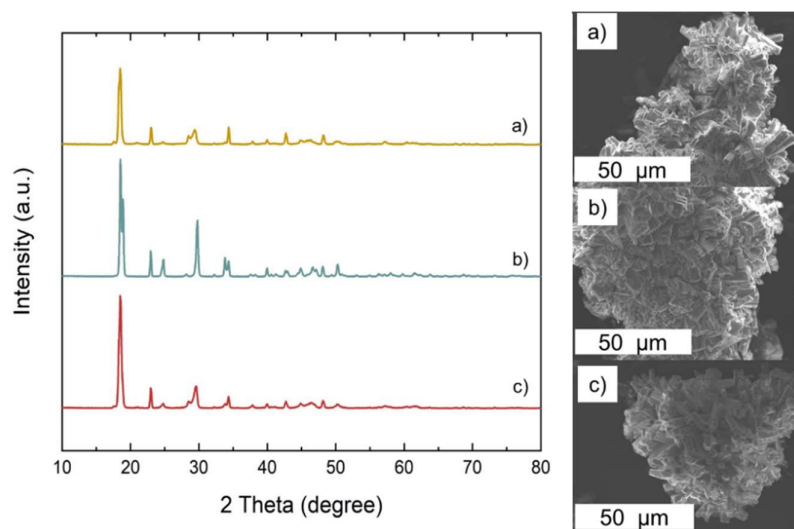

Figure 3-9 XRD patterns and SEM images of the iron(II) oxalate precipitate under the irradiation of simulated sunlight with PFD of a) 4273, b) 2550, and c) 1655 $\mu mol/m^2/s$

3.3.1.3 Effect of solution depth

The DS-Fe_2O_3 samples with different solution volumes were used to determine the effect of solution depth on the rate of photochemical reduction of iron oxalate aqueous solution using a constant simulated sunlight (PFD as 4273 $\mu mol/m^2/s$ and illuminance as 180 klx). The experimental data are listed in **Table 3-2**, while the plots of conversion to $FeC_2O_4 \cdot 2H_2O$, total Fe concentration and Fe^{2+} or Fe^{3+} concentration with the time of DS- Fe_2O_3 samples are presented in **Figure 3-10.**
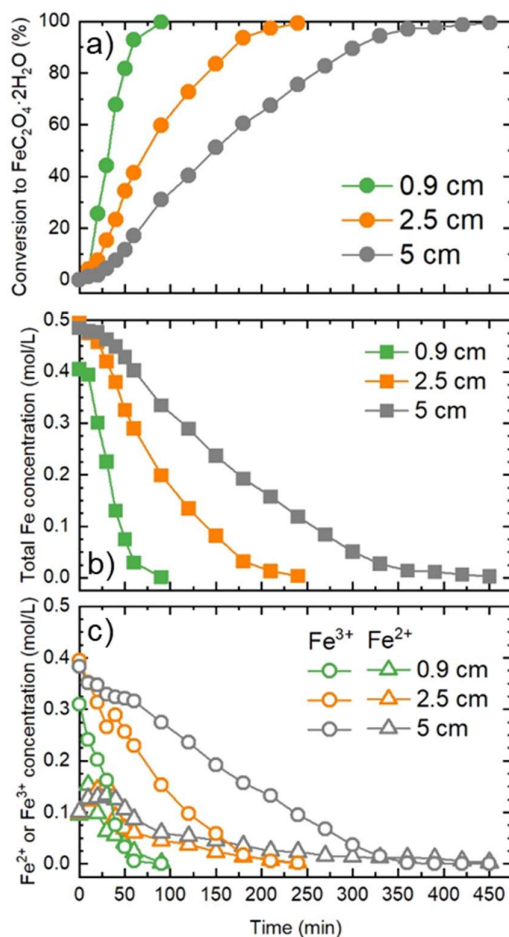
Figure 3-10 Time-dependent change of (a) conversion to $FeC_2O_4 \cdot 2H_2O$, (b) Total Fe concentration and Fe^{2+} or Fe^{3+} concentration. Conditions: different solution depths of DS-Fe_2O_3 samples

Table 3-2 Experimental data of photochemical reduction using simulated sunlight with different solution volumes and solution depths of DS- Fe_2O_3 samples.

| Sample No.	Initial Fe concentration (mol/L)			Solution volume (ml)	Solution depth (cm)	Time (min)	Rate (mol/min)
	Total Fe	Fe^{3+}	Fe^{2+}				
1	0.485	0.383	0.101	90	5	450	0.13
2	0.495	0.395	0.099	45	2.5	240	0.13
3	0.405	0.309	0.095	15	0.9	90	0.13

It clearly sees from the results that the time for completing the reduction in sample 3 which has the lowest initial Fe concentration, solution volume and solution depth was only 90 min which is the fastest in this experiment. However, by calculating the rate of conversion, the results reveal the conversion rates of all samples are 0.13 mol/min. Therefore, it can be simply concluded that under the same light intensity the depths of solution did not significantly affect the rates of conversion to $FeC_2O_4 \cdot 2H_2O$, but it influenced the time for completing the reaction: higher depth of solution required a longer time. This is because the photochemical reduction generally occurs at the exposed liquid surface, therefore, the depth of solution does not affect the rate of conversion. [2]

3.3.1.4 Effect of iron sources and initial iron concentration in iron oxalate aqueous solution

To study the effect of Fe sources and initial Fe concentrations on the rate of photochemical reduction, the iron oxalate aqueous solution obtained from dissolution of Fe_2O_3 and Fe_3O_4 with the different Fe concentrations (denoted as DS- Fe_2O_3 and DS- Fe_3O_4, respectively) were used. The concentration of dissolved Fe species in each solution together with the results from the photochemical reduction are presented in **Table 3-3**

Table 3-3 Experimental data of photochemical reduction using simulated sunlight with different Fe sources and/or initial Fe concentrations of iron oxalate aqueous solution

Source of Fe/ sample name	Initial Fe concentration (mol/L)			Time (min)	Rate (mol/min)
	Total Fe	Fe^{3+}	Fe^{2+}		
DS- Fe_2O_3_1	0.311	0.213	0.098	270	0.165
DS- Fe_2O_3_2	0.425	0.323	0.103	360	0.130
DS- Fe_2O_3_3	0.485	0.383	0.101	450	0.134
DS- Fe_3O_4	0.381	0.323	0.058	360	0.136
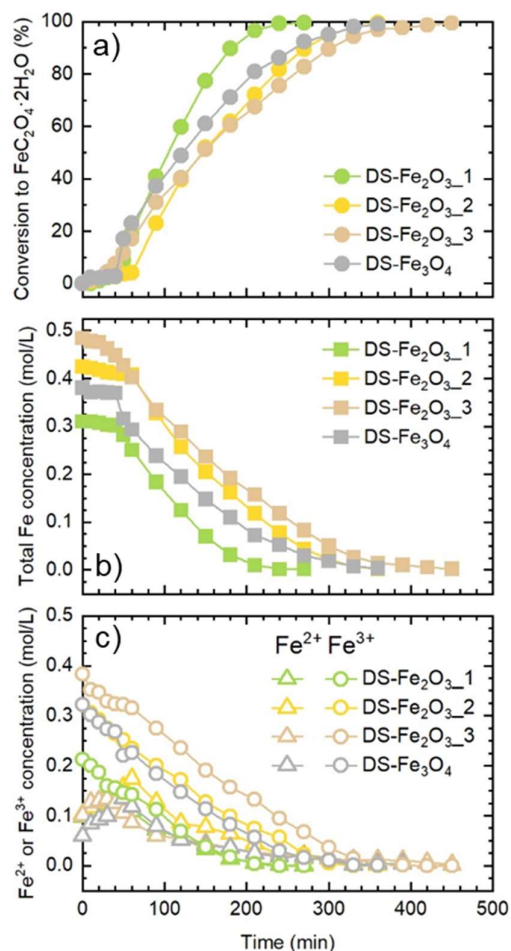
Figure 3-11. Time-dependent change of (a) conversion to $FeC_2O_4 \cdot 2H_2O$, (b) Total Fe concentration and Fe^{2+} or Fe^{3+} concentration. Conditions: 90 ml of solution, 5 cm of solution depth, irradiated under simulated sunlight with PFD about 4273 $\mu mol/m^2/s$

Figure 3-11. shows the time-dependent change of conversion to $FeC_2O_4 \cdot 2H_2O$, and concentration of total Fe, Fe^{2+}, and Fe^{3+} with time. The conversion curves of all samples indicated the same trend: the reduction rates are slow at the beginning of the reaction, where the dissolved Fe^{3+} gradually decreased while the dissolved Fe^{2+} increased. After that, it was dramatically increased when the dissolved Fe^{2+} concentration reached the maximum point, triggering the precipitation of $FeC_2O_4 \cdot 2H_2O$. The rates of conversion are calculated in the range of 20-80 % conversion and listed in **Table 3-3.** By comparing the results of DS- Fe_2O_3 and DS-

Fe_3O_4 samples, these results suggested that the photochemical reduction rates seem to be independent of the sources of iron in Fe(III) oxalate solution, but they significantly depend on the concentrations of initial iron in the solution. Under the same condition, the conversion rates of DS- Fe_2O_3_1, DS- Fe_2O_3_2, DS- Fe_2O_3_3, and DS- Fe_3O_4 are 0.165, 0.13, 0.134, and 0.136 mol/min, respectively. Therefore, it can imply that, under this condition, the rate of conversion and time for complete the reduction depends on the initial concentration of Fe in solution. The possible explanation for this phenomenon might be because when the initial Fe concentrations in solution was high, during the reduction, it was able to produce a dense slurry consisting of diluted Fe(III) oxalate aqueous solution and Fe(II) oxalate particles during the reduction which may obstruct the penetration of light causing the decrease in the rate of conversion.

3.3.2 Photochemical reduction using natural sunlight

To investigate the photochemical reduction using natural sunlight, 45 ml of DS-Fe_2O_3 with 2.5 cm of solution height was used. The initial concentrations of dissolved Fe^{2+}, Fe^{3+} and total Fe are 0.117, 0.368, and 0.485 mol/L, respectively. The results are summarized and presented in **Table 3-4 and Figure 3-12,** while the details of experimental data are listed in **Table S3-2.**

Table 3-4. The results of photochemical reduction using natural sunlight

	Weather	Illuminance (lux)	PPDF* ($\mu mol/m^2/s$)	Initial Fe (mol/L)	Irradiating time	Conv. (%)	Rate (mol/min)
Day 1	Sunny	102300-1633	1893-30	0.485	4 h	35	0.052
Day 2	Cloudy	71930-4013	1449-74	0.288	4 h 30 min	54	0.029
Day 3	mixed	90860-7196	1681-120	0.118	3 h	~100	0.061
Day 1-3		102300-1633	1893-30	0.485	11 h 30 min	~100	0.028

* : PPFD: photosynthetic photon flux density in range of 400-700 nm, unit as $\mu mol/m^2/s$

Figure 3-12 illustrates the relationship of dissolved Fe spices (Fe^{2+}, Fe^{3+} and total Fe), percent of conversion to Fe(II) oxalate, and qualities of natural sunlight in terms of illuminance and PPFD with the irradiating time. Moreover, to observe the change of DS-Fe_2O_3 solution appearance during the reaction, the photos of this solution at some specific times are also presented.
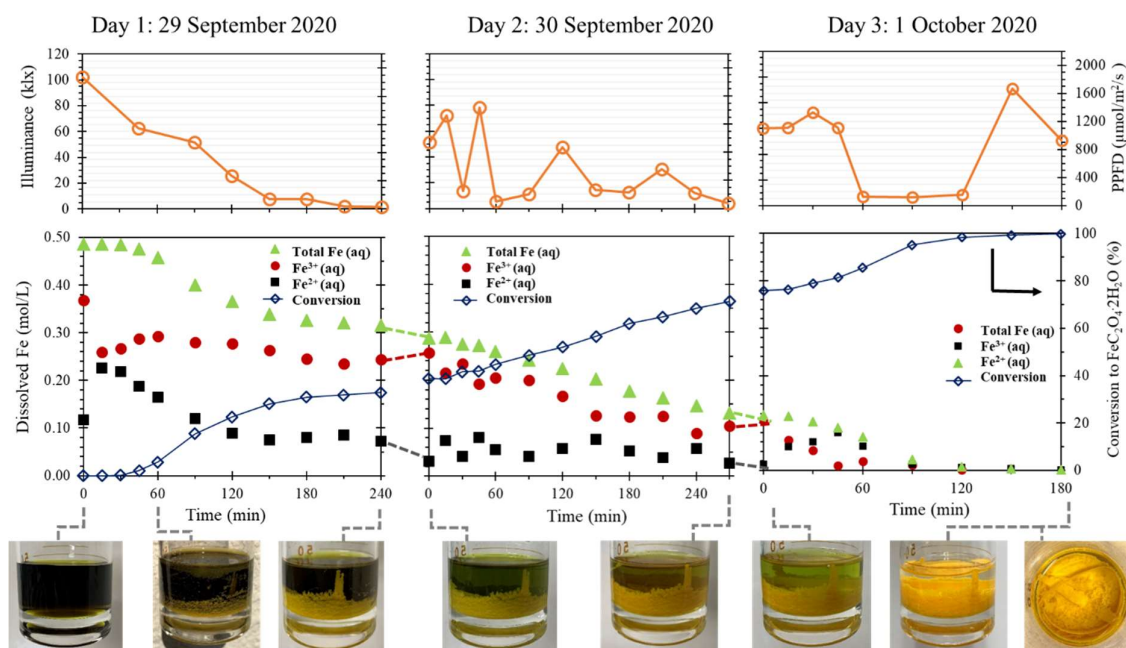
Figure 3-12. Photochemical reduction of DS-Fe_2O_3 using natural sunlight

From **Figure 3-12**, it clearly shows that the qualities of a natural sunlight fluctuate in the range of 102300-1633 lux and 1893-30 $\mu mol/m^2/s$ due to the weather conditions which directly affected the photochemical reduction of DS-Fe_2O_3. At the first 60 min of reaction in day 1, the dissolved species in the iron oxalate solution showed the same trend as using simulated sunlight: the dissolved Fe^{2+} significantly increases with decreasing in amount of dissolved Fe^{3+}, followed by gradually decreasing due to the precipitation of Fe(II)oxalate dihydrate. However, the conversion after 180 min on day 1 levels off when the sunlight intensity, in terms of PPFD, was lower than 140 $\mu mol/m^2/s$ due to sunset, as seen in **Figure 3-**

12. Therefore, the reduction using natural sunlight was paused, and the reactor was kept in dark to avoid any stray light and uncontrollable reactions for the next day experiments.

On the following day, the reactor was placed on the same position as the day 1 to expose to the natural sunlight for proceeding the photochemical reduction. On day 2 and 3 where the illuminance of sunlight is higher, the conversion rose during the reaction. These results suggest that under the sufficient sunlight intensity, Fe^{3+} can be reduced to Fe^{2+} by ligand to metal charge transfer (LCTM) as evidenced by the increase in the concentration of dissolved Fe^{2+}. Thus, from the experimental results, it seems that sunlight with PPFD above 400 $\mu mol/m^2/s$ was sufficient to induce the reduction of Fe^{3+}.

Moreover, the results also confirmed that the conversion to Fe(II) oxalate precipitate strongly depends on the intensity of sunlight. It is worth nothing that during sunset, although the reactor was kept in the dark as mentioned above, the reaction can further proceed even if in the absence of light. As can be seen in **Figure 3-12**, the concentration of dissolved total Fe slightly decreased after storing the reactor in the dark room during night-time. The possible reason of this phenomenon might be the remaining active species, probably $CO_2^{\bullet-}$ and $C_2O_4^{\bullet-}$ radicals, contribute to further reduction of Fe(III), and/or the solution was saturated with Fe^{2+}, resulting in the precipitation of iron(II)oxalate dihydrate. [3,4,14,15]

The photochemical reduction using natural sunlight reached the completion within three days when the total irradiating time was 11 h 30 min with the conversion rate of 0.028 mol/min calculated in the conversion range of 20-80% using only the irradiation time. The resulting rate is much lower than that of using simulated sunlight under the same conditions of iron oxalate aqueous solution. This is because uncontrollable nature of sunlight causing the inconstant light intensity and the limitation of irradiation time due to the sunset.

The obtained iron(II) oxalate precipitate was characterized by XRD and SEM, and the results are shown in **Figure 3-13.** The XRD pattern showed that the iron oxalate precipitate was the mixture between monoclinic (Humboldtine, IDDP 01-076-8451) and orthorhombic structure of $FeC_2O_4 \cdot 2H_2O$ (IDDP 01-075-7291). From the SEM images, the obtained precipitate showed a squared rods structure with the diameter about 6 μm and varied lengths in the range of 15-50 μm. It should be noted that the obtained crystal of $FeC_2O_4 \cdot 2H_2O$ by using natural sunlight was relatively longer and bigger than those obtained from the simulated sunlight, which is probably due to the slower rate of conversion providing the longer time for crystal growth.
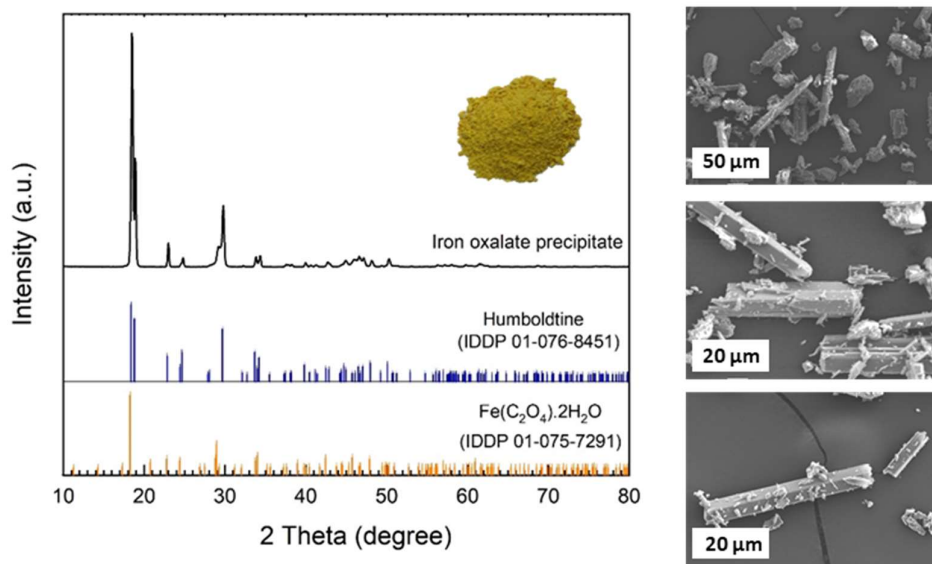
Figure 3-13. XRD pattern and SEM images of the obtained iron (II) oxalate precipitate under the irradiation by natural sunlight

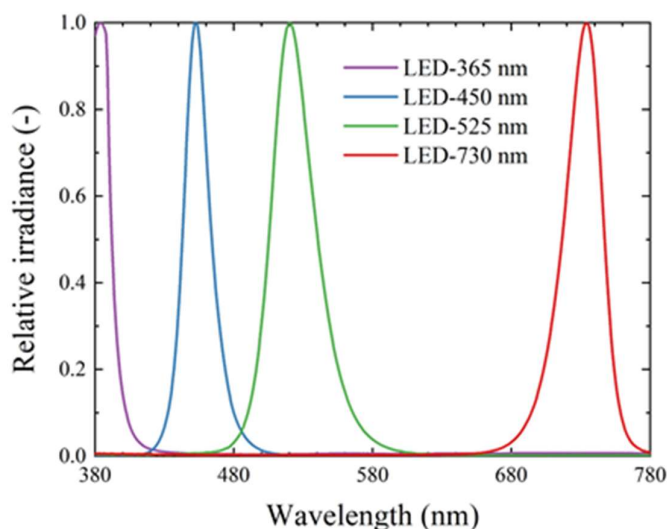### 3.3.3 Photochemical reduction using LED light

To investigate and distinguish the effect of wavelengths of light on the photochemical reduction of iron(II) oxalate aqueous solution, the LED light source which generates the light

centered at a specific wavelength was chosen. In this study, the LED centered at 365 (LED-365 nm), 450 (LED-450 nm), 525 (LED-525 nm), and 730 (LED-730 nm) nm was used. Moreover, in this study, to eliminate the influence from light intensity, a prescribe of PDF at about 490 μmol/m^2/s was set to irradiate the 12 ml of DS-Fe$_2$O$_3$ samples with the solution depth of 2.5 cm.

Hereafter, the DS-Fe$_2$O$_3$ samples were exposed to the LED-365 nm, LED-450 nm, LED-525 nm and LED 730 nm are denoted by PL-365, PL-450, PL-525 and PL-730, respectively.

The relative radiation spectra of these LED lights are shown in **Figure 3-14**, while the properties of lights are listed in **Table S3-3.** The experimental data including some properties of lights and the properties of iron oxalate aqueous solution are summarized in **Table 3-4**, while **Table 3-5** show the experimental results under these conditions.

Figure 3-14. Relative radiation spectra of LED lights centered at 365, 450, 525 and 730 nm

CHAPTER 3

Table 3-4. The experimental data of photochemical reduction using different of LED lights and simulated sunlight (SMSL) at PFD about 490 $\mu mol/m^2/s$

| Sample name	Light source		PFD ($\mu mol/m^2/s$)	Initial dissolved Fe (mol/L)			pH of solution
	Type of light			Total Fe	Fe^{3+}	Fe^{2+}	
PL-365	LED	UV	491	0.495	0.395	0.099	0.25
PL-450	LED	Vis	497	0.485	0.368	0.117	0.26
PL-525	LED	Vis	491	0.459	0.373	0.085	0.29
PL-730	LED	NIR	495	0.465	0.411	0.054	0.22
PSLSM	SMSL	UV-vis	495	0.493	0.400	0.095	0.27

Table 3-5 The experimental results of photochemical reduction using different of LED lights and simulated sunlight (SMSL) at PFD about 490 $\mu mol/m^2/s$

Sample name	Initial Fe (mol/L)	Light intensity ($\mu mol/m^2/s$)				Time (h)	Conver-sion (%)	Rate[&] (mol/min)
		PFD	PFD-UV	PFD-B	PFD-G			
PL-365	0.493	491	330	45	25	1	~100	0.217
PL-450	0.487	497	0.5	490	5.2	8.5	~100	0.015
PL-525	0.478	491	0.5	30	453	> 97	92	0.001
PL-730	0.465	495	0.4	1.7	1.9	-	0	-
PSLSM	0.493	495	7.2	88.2	133.6	24	~100	0.006

Note: PFD: photon flux density in range of 380-780 nm, unit as $\mu mol/m^2/s$
PFD-UV: PFD in UV field (380-400 nm)
PFD-B: PFD in blue field (400-500 nm)
PFD-G: PFD in green field (500-600 nm)
[&] calculated in the conversion range of 20~80%

Figure 3-15 shows the time-dependent results of photochemical reduction of DS-Fe$_2$O$_3$ using different wavelengths of LED light in the dark room. It should be noted that the reaction time of 500 min is presented in **Figure 3-15**, but the experiments using LED-525 nm and LED-730 nm were carried out over the course of 97 h and 18 h, respectively. Thus, a full course of experimental results by using LED-525 nm and LED-730 nm are plotted and presented in **Figure S3-1, Figure S3-2**, respectively.
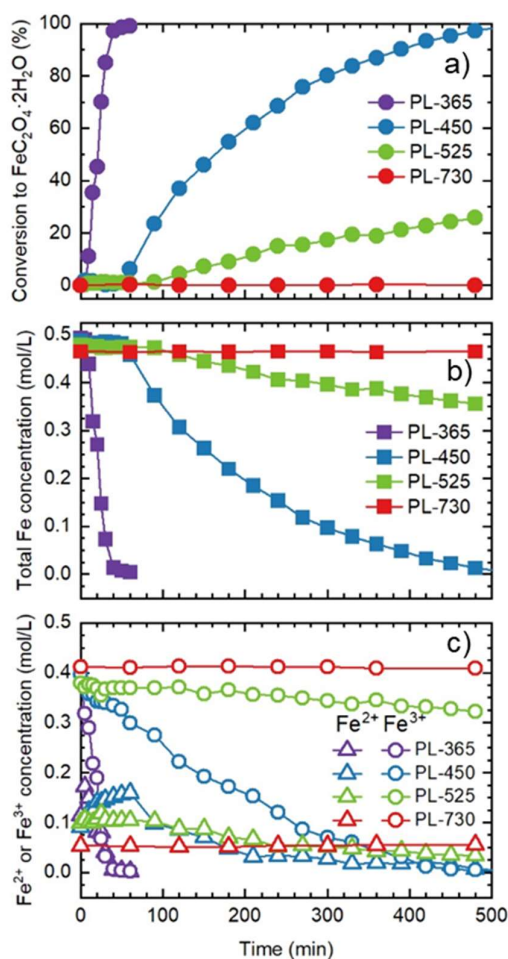
Figure 3-15 Time-dependent change of (a) conversion to FeC$_2$O$_4$.2H$_2$O, (b) Total Fe concentration and Fe^{2+} or Fe^{3+} concentration. Conditions: irradiation under different LED lights, room temperature, continuous stirring.

CHAPTER 3

As expected, from the results, it confirms that LED lights with the wavelengths of 365, 450 and 525 nm are able to reduce Fe^{3+} in iron oxalate aqueous solution resulting in the precipitation of $FeC_2O_4 \cdot 2H_2O$. However, by using LED-730 nm, the photochemical reduction cannot occur even if the reaction time was extended until 18 h (**Figure S3-2**), evidenced by the percent of conversion of PL-730 sample remained at 0 over the full course of observation. Moreover, it did not show any effect on the concentration of each dissolved Fe species in the solution, as clearly seen in **Figure 3-15 and Figure S3-2**. These results agreed with the previous studies that the lights under the tropospheric solar UV-Vis (290-570 nm) can induce the ligand-to-metal charge transfers of Fe (III)-oxalate complexes. [1,2,8-11]

Under the similar of LED light intensity, PFD about 490 $\mu mol/m^2/s$, the results show that the photochemical reduction of PL-365 sample irradiated by LED-365 nm is fastest, it reached the completion in 90 min, while by using LED-450 and LED-525 nm, the time required for completing the reduction was 8.5 h and more than 97 h, respectively. The conversion rates of PL-365, PL-450 and PL-525 nm are 0.217, 0.015, 0.001 mol/min, calculated in the range of conversion as 20~80%. It is also worth highlighting the effect of wavelengths of light used. Although the LED light centered at 365, 450 and 525 nm can induce the photochemical reduction, the fastest rate of conversion was obtained from the in the UV-region, LED-365 nm, accounting for 0.217 mol/min which is more than 10 times higher than those obtained from others LED-lights in this study. Therefore, it can be summarized that apart from the light intensity which directly affects the rate of photochemical reduction, the wavelength of light, in other words, the region of light also plays an important role in the rate of reaction: light in UV-region has high impact on photochemical reduction of iron(III) oxalate in aqueous solution.

For further clarification, the simulated sunlight (SMSL) with PFD as 495 $\mu mol/m^2/s$ was used to irradiate the $DS\text{-}Fe_2O_3$ under the same conditions: solution volume of 12 ml and

depth of solution of 2.5 cm, named as PSMSL, in order to compare the effect of wavelength of light. The result of PSMSL sample are included in **Table 3-5** and presented **Figure 3-16.**
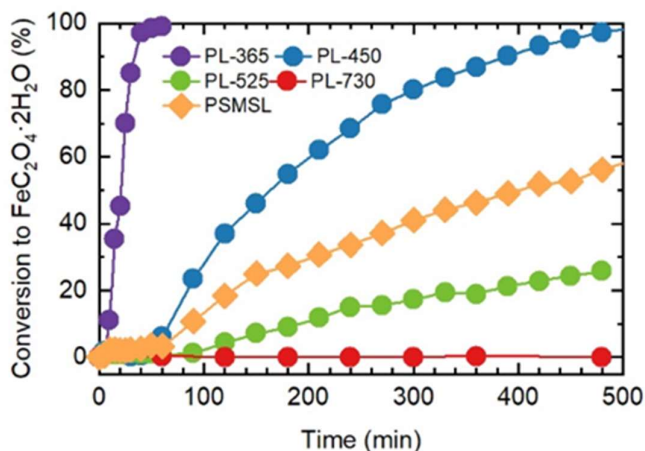

Figure 3-16 Time-dependent change of conversion to $FeC_2O_4 \cdot 2H_2O$ during photochemical reduction of DS-Fe_2O_3 under the radiation of different light sources: LED-365, LED-450 nm, LED-525 nm, LED-730 nm, and simulated sunlight (SMSL) at PFD about 490 $\mu mol/m^2/s$.

The results show that, under the same PFD, although SMSL having a wide spectrum of wavelengths is used, the rates of conversion still depended on the wavelength of light. The total intensity of light that close to UV-region (PFD-UV plus with PFD-B) gave the faster in conversion rate. Thus, LED-365 nm which has the highest total PFD in those regions, accounting for 375 $\mu mol/m^2/s$, provided the fastest in rate of conversion, followed by LED-450 nm (490.5 $\mu mol/m^2/s$), SMSL (95.4 $\mu mol/m^2/s$), and LED-525 nm (95,4 $\mu mol/m^2/s$), respectively.

Figure 3-17 show the XRD patterns and SEM images of the obtained iron oxalate precipitation in all experiments. The results confirmed that all precipitates are $FeC_2O_4 \cdot 2H_2O$ but in different structure. The obtained $FeC_2O_4 \cdot 2H_2O$ from LED-365 nm and LED-450 nm are

in the orthorhombic structure (IDDP 01-075-7291) with the morphology as squared rods while they are in the monoclinic structure with the morphology as the pyramidal-shaped particles when LED-525 nm and SMSL were used. This is probably because the rate of conversion which influences on the crystal growth: the reaction having faster rate of conversion tended to provide the $FeC_2O_4 \cdot 2H_2O$ with the orthorhombic structure, while the slower one gave in the monoclinic structure with the higher crystallinity.
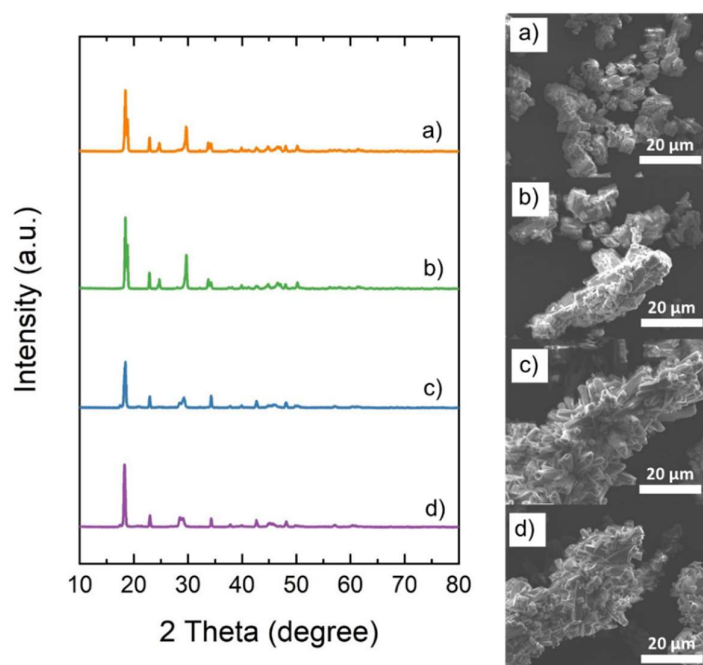
Figure 3-17 The XRD patterns, photos and images of the obtained iron oxalate precipitate under the radiation of a) SMSL, b) LED-525 nm, c) LED-450 nm, and d) LED-365 nm.

3.4 Conclusions

The photochemical reduction of iron(III) oxalate aqueous solution was investigated to reveal the chemistry under various conditions with a particular purpose for its application for iron-making. The results suggested that, by using the simulated sunlight, the rate of conversion strongly depends on the light intensity; it is approximately proportional to the of light intensity

(PFD), whereas sources of iron in iron (III) oxalate solution, and the depth of solution did not show a significant effect on the rate of conversion.

However, when the LED lights were used, the results revealed the rate of reduction of LED-365 nm in the UV-region (0.217 mol/min) was more than 10 times faster compared to LED-450 (0.015 mol/min), and more than 30 times faster, compared to that of using simulated sunlight (0.006 mol/min), under the same PFD of 490 $\mu mol/m^2/s$. Thus, it can be concluded that apart from the light intensity which directly affects the rate of photochemical reduction, the wavelength of light (or the region of light) also plays an important role in the rate of reaction: light near UV-region has a high impact on the photochemical reduction of iron(III) oxalate in aqueous solution.

In addition, this study also confirmed that natural sunlight could reduce the iron(III) oxalate aqueous solution to iron(II) oxalate dihydrate precipitate, but it required more time to complete the reaction due to the weather and location dependency. Moreover, the precipitation can slightly further proceed in the absence of light when the solution contained the actives species or/and it was supersaturated with Fe^{2+}.

Although the three different light sources were used in this study, the obtained Fe(II) oxalate precipitate from photochemical reduction are indexed to be pure $FeC_2O_4 \cdot 2H_2O$. However, they are slightly different in their structures, crystallinities, and crystal sizes, which probably results from the rate of conversion. When the conversion rate is fast, it tends to provide the orthorhombic structure with the lower crystallinity.

CHAPTER 3

3.5 References

[1] Parker, C. A.; Hatchard, C. G. Photodecomposition of Complex Oxalates. Some Preliminary Experiments by Flash Photolysis. J. Phys. Chem. 1959, 63 (1), 22–26. https://doi.org/10.1021/j150571a009.

[2] Dudeney, A. W. L.; Tarasova, I. I. Photochemical Decomposition of Trisoxalatoiron(III): A Hydrometallurgical Application of Daylight. Hydrometallurgy 1998, 47 (2–3), 243–257. https://doi.org/10.1016/s0304-386x(97)00049-2.

[3] Ogi, Y.; Obara, Y.; Katayama, T.; Suzuki, Y. I.; Liu, S. Y.; Bartlett, N. C. M.; Kurahashi, N.; Karashima, S.; Togashi, T.; Inubushi, Y.; et al. Ultraviolet Photochemical Reaction of $[Fe(III)(C_2O_4)_3]^{3-}$ in Aqueous Solutions Studied by Femtosecond Time-Resolved X-Ray Absorption Spectroscopy Using an X-Ray Free Electron Laser. Struct. Dyn. 2015, 2 (3). https://doi.org/10.1063/1.4918803.

[4] Chen, J.; Zhang, H.; Tomov, I. V.; Rentzepis, P. M. Electron Transfer Mechanism and Photochemistry of Ferrioxalate Induced by Excitation in the Charge Transfer Band. Inorg. Chem. 2008, 47 (6), 2024–2032. https://doi.org/10.1021/ic7016566.

[5] Song, X.; Chen, Z.; Wang, X.; Zhang, S. Ligand Effects on Nitrate Reduction by Zero-Valent Iron: Role of Surface Complexation. Water Res. 2017, 114, 218–227. https://doi.org/10.1016/j.watres.2017.02.040.

[6] Cornell, R. M.; Schindler, P. W. Photochemical Dissolution of Goethite in Acid/Oxalate Solution. Clays Clay Miner. 1987, 35 (5), 347–352. https://doi.org/10.1346/CCMN.1987.0350504.

[7] Yu, Z. L.; Shi, Z. X.; Chen, Y. M.; Niu, Y. J.; Wang, Y. X.; Wan, P. Y. Red-Mud Treatment Using Oxalic Acid by UV Irradiation Assistance. Trans. Nonferrous Met. Soc. China 2012, 22 (2), 456–460. https://doi.org/10.1016/S1003-6326(11)61198-9.

[8] Dong, Y.; Chen, J.; Li, C.; Zhu, H. Decoloration of Three Azo Dyes in Water by Photocatalysis of Fe (III)-Oxalate Complexes/H_2O_2 in the Presence of Inorganic Salts. Dye. Pigment. 2007, 73 (2), 261–268. https://doi.org/10.1016/j.dyepig.2005.12.007.

[9] Zhou, D.; Wu, F.; Deng, N. Fe(III)-Oxalate Complexes Induced Photooxidation of Diethylstilbestrol in Water. Chemosphere 2004, 57 (4), 283–291. https://doi.org/10.1016/j.chemosphere.2004.05.043.

[10] Deng, N.; Wu, F.; Tian, S.; Fang, T. Photodegradation of Dyes in Aqueous Solutions Containing Fe(III)-oxalato Complexes. Chemosphere 1997, 35 (11), 2697–2706.

[11] Yuegang, Z.; Jürg, H. Formation of Hydrogen Peroxide and Depletion of Oxalic Acid in Atmospheric Water by Photolysis of Iron(III)-Oxalato Complexes. Environ. Sci. Technol. 1992, 26 (5), 1014–1022. https://doi.org/10.1021/es00029a022.

[12] Hatchard, C. G.; Parker, C. A. A New Sensitive Chemical Actinometer. I. Some Trials with Potassium Ferrioxalate. Proc. R. Soc. London. Ser. A. Math. Phys. Sci. 1953, 220 (1140), 104–116. https://doi.org/10.1098/rspa.1953.0175.

[13] Wehry, L. Photochemical Behaviour of Transition-Metal Complexes. Q. Rev. Chem. Soc. 1967, 21, 213–230. https://doi.org/10.1039/QR9672100213.

[14] Weller, C.; Horn, S.; Herrmann, H. Effects of Fe(III)-Concentration, Speciation, Excitation-Wavelength and Light Intensity on the Quantum Yield of Iron(III)-Oxalato Complex Photolysis. J. Photochem. Photobiol. A Chem. 2013, 255, 41–49 [15] Mangiante, D. M.; Schaller, R. D.; Zarzycki, P.; Banfield, J. F.; Gilbert, B. Mechanism of Ferric Oxalate Photolysis. ACS Earth Sp. Chem. 2017, 1 (5), 270–276. https://doi.org/10.1021/acsearthspacechem.7b00026.

[16] Baran, E. J. Natural Iron Oxalates and Their Analogous Synthetic Counterparts: A Review. Chemie der Erde 2016, 76 (3), 449–460. https://doi.org/10.1016/j.chemer.2016.06.005.

CHAPTER 3

3.6 Supporting information

Table S3-1. Properties of simulated sunlight (SMSL) at different intensities.

Sample name / properties of SMSL	DS-Fe$_2$O$_3$_1	DS-Fe$_2$O$_3$_2	DS-Fe$_2$O$_3$_3
Illuminance (lux)	178821.6	107771.3	70521.0
Irradiance (W/M^2)	866.6129	518.811	337.443
λp	470	470	470
Purity	12.9	11.6	11.0
PPFD	3169.9536	1906.1122	1243.955
PFD	4273.9277	2549.7542	1654.84
PFD-UV	66.498741	40.327568	26.38902
PFD-B	736.19812	452.14594	298.162
PFD-G	1124.9052	679.29987	445.0707
PFD-FR	1308.8502	774.66589	500.722

Note: λp: Peak wavelength in range of 380-780 nm

PPFD: photosynthetic photon flux density in range of 400-700 nm, unit as μmol/m^2/s

PFD: photon flux density in range of 380-780 nm, unit as μmol/m^2/s

PFD-UV: PFD in UV field (380-400 nm)

PFD-B: PFD in blue field (400-500 nm)

PFD-G: PFD in green field (500-600 nm)

PFD-R: PFD in red field (600-700 nm)

PFD-FR: PFD in IR field (700-780 nm)

Table S3-2. The experimental data of photochemical reduction of DS-Fe$_2$O$_3$ using natural sunlight performing on Sep 29-Oct 1, 2020.

Time (min)	Dissolved Fe (mol/L)			Conv. (%)	Natural sunlight		
	Total	Fe^{2+}	Fe^{3+}		time	Illuminance (lux)	PPFD (μmol/m^2/s^1)
Day 1_0	0.485	0.117	0.368	0	14.00	102300	1892.6
15	0.485	0.226	0.259	0	14.15	N/A	N/A
30	0.484	0.218	0.267	0	14.30	N/A	N/A
45	0.475	0.188	0.287	2	14.45	62280	1152.2
60	0.458	0.165	0.292	6	15.00	N/A	N/A
90	0.400	0.120	0.279	18	15.30	51740	957.2
120	0.366	0.089	0.277	25	16.00	25480	471.4
150	0.339	0.075	0.263	30	16.30	7498	138.7
180	0.325	0.081	0.245	33	17.00	7498	138.7
210	0.321	0.085	0.235	34	17.30	1897	35.1
240	0.316	0.072	0.244	35	18.00	1633	30.2
Day 2_0	0.288	0.030	0.258	0	12.30	51430	951.5
15	0.289	0.074	0.215	0	12.45	71930	1330.7
30	0.275	0.041	0.234	5	13.00	13510	249.9
45	0.273	0.080	0.193	5	13.15	78330	1449.1
60	0.259	0.055	0.204	10	13.30	5456	100.9
90	0.241	0.041	0.200	16	14.00	11130	205.9
120	0.224	0.058	0.166	22	14.30	47780	883.9
150	0.203	0.077	0.126	30	15.00	14500	268.3
180	0.177	0.053	0.124	39	15.30	12450	230.3
210	0.163	0.038	0.125	43	16.00	30320	560.9
240	0.146	0.058	0.089	49	16.30	12240	226.4
270	0.132	0.027	0.105	54	17.00	4013	74.2
Day 3_0	0.118	0.012	0.105	0	11.30	60150	1112.8
15	0.115	0.051	0.064	2	11.45	60880	1126.3
30	0.102	0.060	0.042	13	12.00	72550	1342.2
45	0.090	0.080	0.011	23	12.15	60500	1119.3
60	0.071	0.052	0.019	40	12.30	7196	133.1
90	0.023	0.012	0.011	80	13.00	6484	120.0
120	0.008	0.007	0.001	93	13.30	8340	154.3
150	0.003	0.004	0.000	97	14.00	90860	1680.9
180	0.001	0.001	0.000	99	14.30	50890	941.5

CHAPTER 3

Table S3-3. Properties of LED lights and simulated sunlight with the photon flux density (PFD) about 490 μmol/m²/s.

Types / properties of light source	LED light centered at:				Simulated sunlight (SMSL)
	365 nm	450 nm	525 nm	730 nm	
Illuminance (lux)	4129.5	5433.7	54700.5	397.3	21172.3
Irradiance (W/M²)	135.6	130.4	111.4	81.6	100.8
λp	385	452	521	734	470
Purity	18.0	98.5	79.5	26.1	12
PPFD	111.4	496.1	487.6	29.7	372.3
PFD	490.9	497.4	491.0	495.0	495.1
PFD-UV	329.7	0.5	0.5	0.4	7.7
PFD-B	44.7	490.0	29.9	1.7	88.2
PFD-G	24.9	5.2	452.6	1.9	133.6
PFD-R	41.8	0.9	5.2	26.0	150.5
PFD-FR	49.8	0.7	2.9	464.9	115.0

Note: λp: Peak wavelength in range of 380-780 nm

PPFD: photosynthetic photon flux density in range of 400-700 nm, unit as μmol/m²/s

PFD: photon flux density in range of 380-780 nm, unit as μmol/m²/s

PFD-UV: PFD in UV field (380-400 nm)

PFD-B: PFD in blue field (400-500 nm)

PFD-G: PFD in green field (500-600 nm)

PFD-R: PFD in red field (600-700 nm)

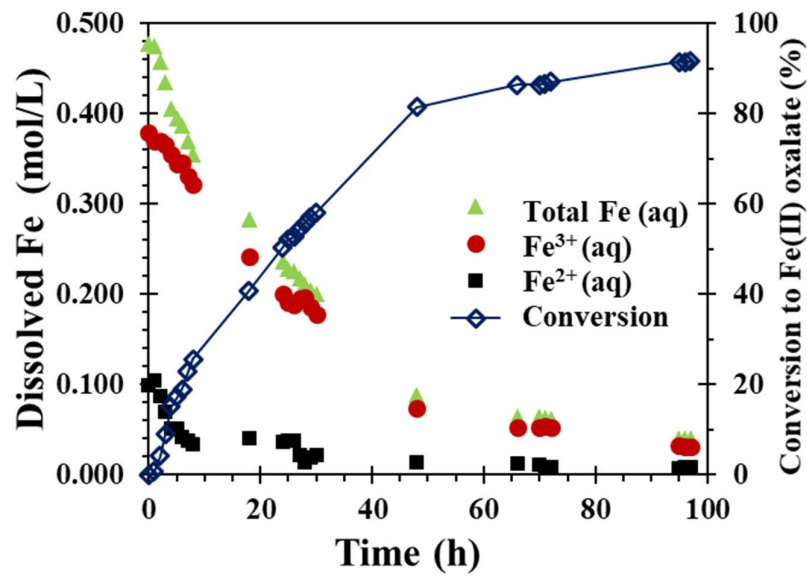PFD-FR: PFD in IR field (700-780 nm)

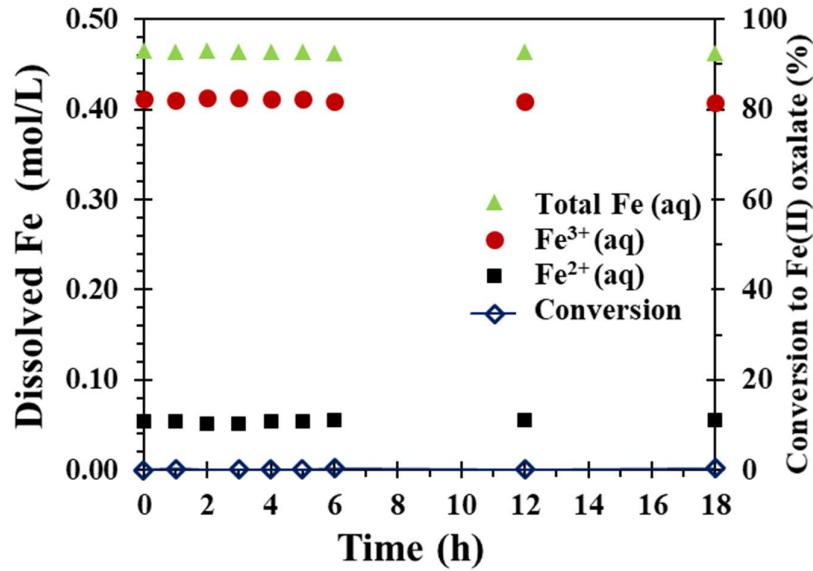**Figure S3-1.** Photochemical reduction of PL-525 sample

**Figure S3-2.** Photochemical reduction of PL-730 sample

CHAPTER 4

Pyrolytic Reduction of Iron(II) Oxalate Dihydrate

4.1 Introduction

Thermal treatment of metal oxalates is an approach used to synthesize nanocrystalline metals or metal oxides. Fe(II) oxalate dehydrate, is the typical precursor, and its thermal behavior has been investigated in some reports. [1-5]

Figure 4-1 presents mass release curves for pyrolysis of Fe(II) oxalate dihydrate under a flow of N_2 or 50% H_2/N_2, analyzed in this study.
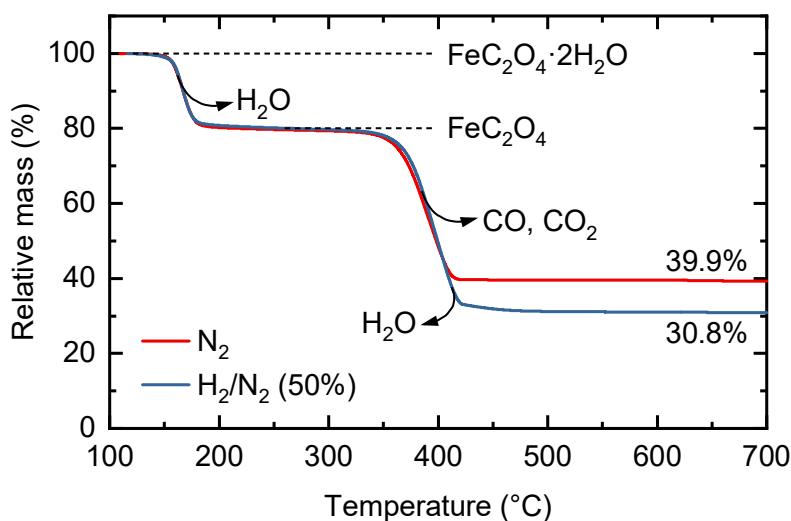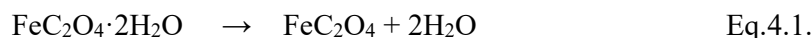

Figure 4-1. Mass release curves of Fe(II) oxalate dihydrate in the pyrolysis under a flow of N_2 or H_2/N_2 (50%): sample 5 mg, heating rate 10 °C/min, and gas 300 mL/min.

Upon heating, Fe(II) oxalate dehydrate ($FeC_2O_4.2H_2O$) starts to releases water corresponding to the dehydration process in which two water molecules were lost, forming anhydrous Fe(II) oxalate (FeC_2O_4) that is thermally stable up to around 300 °C, as shown in Eq 4.1. At higher temperatures, Fe(II) oxalate pyrolyzes with the release of CO and CO_2 to

form metallic iron, iron oxides, or iron carbides. The chemical form and composition of the iron product are significantly influenced by the atmosphere during the occurrence of pyrolysis. Although the reaction mechanism that determines the chemical form is still contested, most studies have identified FeO as the primary product during the pyrolysis under an inert atmosphere, which was also confirmed in **Figure 4-1** by the relative mass of 39.9%, corresponding to the generation of FeO (Eq. 4.2), at above 420 °C.

In the presence of H_2, the mass release curve followed the same path at temperature below 400 °C, but continued decreasing to 30.8%, which indicated the formation of metallic iron (Fe), and the reaction equation is show in Eq.4.3. The result strongly supports the occurrence of iron production from iron oxalates in the scheme proposed in this study. Furthermore, iron formation was complete at low temperatures of below 500 °C. Since the conversion of Fe(II) oxalate into iron involves pyrolytic reactions in the presence of H_2, this step is called pyrolytic reduction in our process.

$$FeC_2O_4 \cdot 2H_2O \quad \rightarrow \quad FeC_2O_4 + 2H_2O \qquad \qquad \text{Eq.4.1.}$$

$$FeC_2O_4 \quad \rightarrow \quad FeO + CO + CO_2 \qquad \qquad \text{Eq.4.2.}$$

$$FeC_2O_4 + H_2 \quad \rightarrow \quad Fe + CO + CO_2 + H_2O \qquad \qquad \text{Eq.4.3.}$$
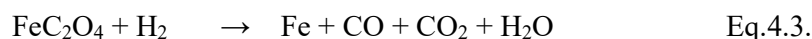
As can be seen from the Eq. 4.4, during the pyrolytic reduction of Fe(II) oxalate dihydrate it generates CO and CO_2 gases along with the reduction which may influence the obtained iron product. Therefore, in this chapter, Fe(II) oxalate dihydrate was investigated under various atmospheric conditions in order to observe and clarify the thermal behaviors in those atmosphere which can serve as a guideline for the design of pyrolytic reactor in this iron-making process. Moreover, the obtained Fe(II) oxalate dihydrate from various photochemical reduction conditions (in Chapter 3) and the Fe(II) oxalate dihydrate precipitate from dissolution

CHAPTER 4

(in chapter 2) were used as an iron precursor pyrolytic reduction in order to prove that all of the precipitates can produce Fe metal under this condition.

4.2 Materials and methods

4.2.1 Materials

$FeC_2O_4 \cdot 2H_2O$ (Wako Pure Chemical) was used for investigation of the thermal behavior under different atmospheric conditions: N_2, 50%H_2/N_2, 50%CO_2/N_2, 50%CO/N_2, and 50%air/N_2. The obtained Fe(II) oxalate dihydrate from various photochemical reduction conditions (in Chapter 3) and Fe(II) oxalate dihydrate precipitates from dissolution (in chapter 2) were used as the iron precursor for metallic iron production.

4.2.2 Pyrolytic reduction

Experimental investigations of the thermal behavior of $FeC_2O_4 \cdot 2H_2O$ carried out by a thermogravimetric analyzer (Hitachi Hi-Tech Science, STA7200) that was operated with the heating rate of 10 °C/min and gas flow rate of 300 mL/min.

For pyrolytic reduction, iron(II) oxalate dihydrate samples, about 0.1-1.0 g, were heated using a tube furnace under a flow of 50% H_2/N_2 at the heating rate of 10 °C/min to 600 °C with 1 h of holding time. After the pyrolytic reaction, the obtained iron was natural cooled down to room temperature and kelp it in the tube furnace under N_2 atmosphere for about 7 h to avoid the reoxidizidation by air.

4.2.3 Characterizations

The mass release curve in the pyrolytic reduction was analyzed on a thermogravimetric analyzer (Hitachi Hi-Tech Science, STA7200) that was operated with a heating rate of 10 °C/min and gas flow rate of 300 mL/min. The crystalline structure was analyzed by X-ray diffraction (XRD) on a Rigaku, TTR-III with Cu Kα radiation at 50 kV and 30 mA. The

morphology of iron samples was observed by Scanning electron microscope, SEM (a Keyence VE 9800 real 3D system).

4.3 Results and dissolution

4.3.1 Thermal analysis of Fe(II) oxalate dihydrate under various atmospheric conditions

The mass release curves for pyrolysis of Fe(II) oxalate dihydrate, $FeC_2O_4 \cdot 2H_2O$, under the flow of N_2, 50%H_2/N_2, 50%CO_2/N_2, 50%CO/N_2 or 50%air/N_2 are illustrated in **Figure 4-2.** It is clearly seen from the results that the obtained mass release curves of Fe(II) oxalate dihydrate are different depending on the atmospheric gas, which means that the atmospheric gas affects the thermal decomposition of Fe(II) oxalate dihydrate.
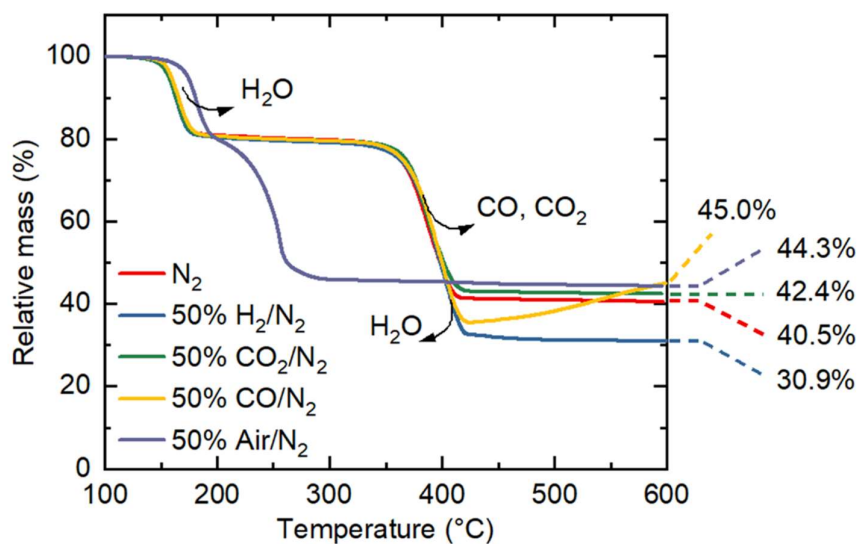

Figure 4.2. Mass release curves of Fe(II) oxalate dihydrate in the pyrolysis under the flow of N_2, 50%H_2/N_2, 50%CO_2/N_2, 50%CO/N_2 or 50%air/N_2: sample 5 mg, heating rate 10 °C/min, and gas 300 mL/min.

The decomposition of $FeC_2O_4 \cdot 2H_2O$ under N_2 atmosphere produced FeO as the final iron product, resulting in the presence of relative mass as 40.5%, while it can be reduced to Fe under the 50%H_2/N_2 atmosphere, as described above. In the case of oxidizing atmosphere

(50%CO_2/N_2 and 50%air/N_2), the decomposition of iron (II) oxalate provided the Fe_3O_4 as the final iron product under the atmosphere of 50%CO_2/N_2, corresponding to the presence of relative mass as 42.4%. On the other hand, Fe_2O_3 was obtained when 50%air/N_2 gas was used because the O_2 containing in air oxidized FeO which is the primary product during the pyrolysis under N_2 atmosphere to Fe_2O_3, as evidenced by the relative mass as 44.3%. However, the mass release curves of Fe(II) oxalate dihydrate under 50%CO/ N_2 atmosphere is complicated, and it cannot be analyzed by using only the relative mass curve from TGA. Therefore, XRD was used to clarify and confirmed the phase of the obtained iron products.
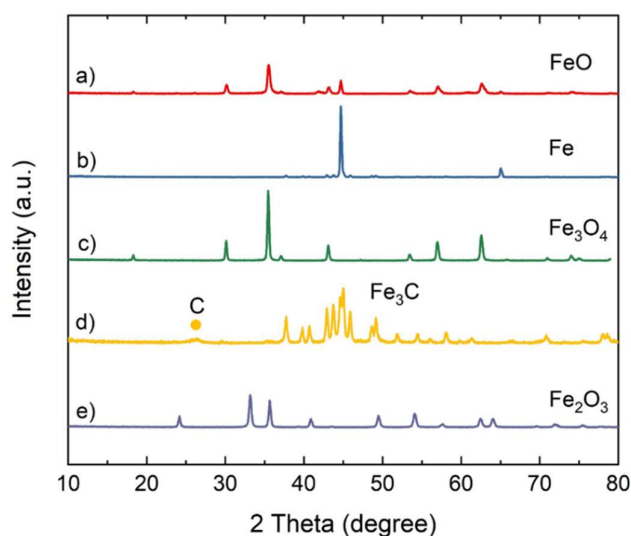

Figure 4-3. XRD patterns of the obtained product from the pyrolytic of Fe(II) oxalate dihydrate under the flow of (a) N_2, (b) 50%H_2/N_2, (c) 50%CO_2/N_2, (d) 50%CO/N_2 and (e) 50%air/N_2. (*Note: the intensity showing in XRD pattern of (d) 50%CO/N_2 was multiplied by 3*).

Figure 4-3 presents the XRD patterns of the obtained iron product from pyrolysis under different atmospheric conditions. It should be noted that the XRD pattern of the obtained iron product under the pyrolytic with 50%CO_2/N_2 gases, labeled as d), was multiplied by 3 in order to clearly see the peaks for comparison. When combined with the XRD analysis, it was found that the obtained iron product under CO/ N_2 atmosphere was a mixture between Fe_3C (IDDP

00-008-0415) and graphite (C, IDDP 00-008-0415), as shown in **Figure 4-3.** While the XRD results of obtained product from N_2, $50\%H_2/N_2$, $50\%CO_2/N_2$, and $50\%air/N_2$ also correspond to the TGA results that it was FeO (IDDP 01-073-2143), α-Fe (IDDP 01-071-4409), Fe_3O_4 (IDDP 01-071-6336), and Fe_2O_3 (IDDP 01-071-5008), respectively.

Based on those results, it is confirmed that the decomposition of iron (II) oxalate dihydrate under the atmosphere of CO and CO_2 gases which are the generated gases in the proposed iron-making process led to non-metallic iron, although the CO is the reducing gas which is the same as H_2. Therefore, in order to conserve the metallic iron as the final product under the pyrolytic reduction, it is necessary to reduce the contact between iron (II) oxalate and the pyrolysis product gas (CO and CO_2) during thermal decomposition at high temperature.
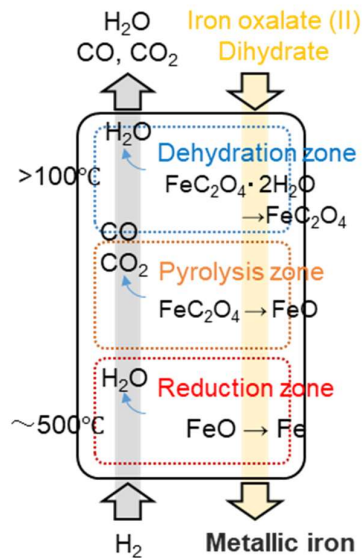
Figure 4-4. Schematic diagram of the proposed updraft type moving bed reactor for pyrolytic reactor

Thus, the updraft type moving bed reactor which is effective for minimizing the consumption of hydrogen and avoiding the contact between pyrolysis gas and pyrolyzing solids is suggested to use be a suitable pyrolytic reactor in the proposed iron-making process, as illustrated in **Figure 4-4.**

CHAPTER 4

4.3.2 Pyrolytic reduction of iron(II) oxalate precipitate

The obtained Fe(II) oxalate dihydrate precipitates from various photochemical reduction conditions and the precipitation during the dissolution are reduced with $50\%H_2/N_2$ atmosphere at 600 °C by using a tube furnace. The experimental data is listed in **Table 4-1**, and the photos of iron sample before ($FeC_2O_4 \cdot 2H_2O$) and after (metallic iron, Fe) pyrolytic reduction are shown in **Figure 4-5**.

Table 4-1 The experimental data of pyrolytic reduction of Fe(II) oxalate dihydrate

Sample name	Obtained conditions of $FeC_2O_4 \cdot 2H_2O$			%yield of Fe
	Source of Fe	Reaction	Conditions	
a	$DS\text{-}Fe_2O_3$	Photochemical reduction	SMSL-180 klx	100
b	$DS\text{-}Fe_2O_3$	Photochemical reduction	SMSL-110 klx	100
c	$DS\text{-}Fe_2O_3$	Photochemical reduction	SMSL-70 klx	98
d	$DS\text{-}Fe_2O_3$	Photochemical reduction	LED-365 nm	97
e	$DS\text{-}Fe_2O_3$	Photochemical reduction	LED-450 nm	101
f	$DS\text{-}Fe_2O_3$	Photochemical reduction	LED-525 nm	102
g	$DS\text{-}Fe_2O_3$	Photochemical reduction	Natural sunlight	100
h	$DS\text{-}Fe_3O_4$	Photochemical reduction	SMSL-180 klx	100
i	Fe_3O_4	Dissolution	92 °C	103
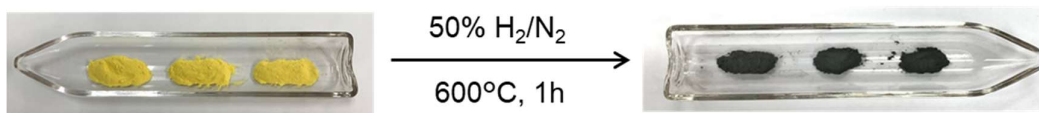
Figure 4-5. Photos of $FeC_2O_4 \cdot 2H_2O$ precursor (left) and the obtained metallic iron (right) from pyrolytic reduction under $50\%H_2/N_2$ atmosphere at 600 °C.

The obtained iron products were characterized by using XRD and SEM, as shown in **Figure 4-6** and **Figure 4-7**, respectively. From the XRD results, it confirms that the obtained iron from all samples were a pure α-Fe (IDDP 01-071-4409) without other iron phases and the recover yields are about 100%. The differences in peak intensities of the α-Fe products are probably due to the crystallinity and size of its corresponding $FeC_2O_4 \cdot 2H_2O$ precursor.
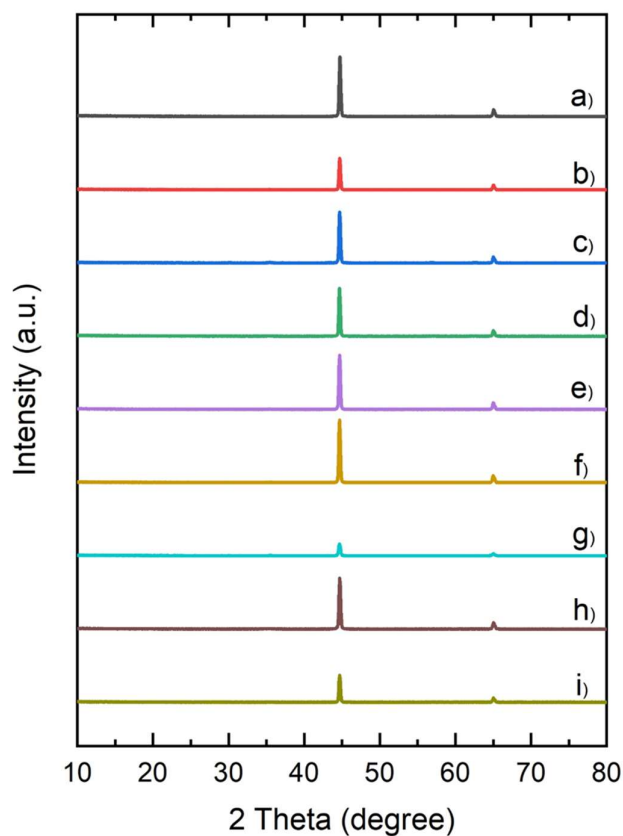
Figure 4-6. XRD patterns of the obtained Fe from the obtained $FeC_2O_4 \cdot 2H_2O$ precipitates from different routes: photochemical reduction of DS-Fe_2O_3 by using simulated sunlight at a) 180 klx, b) 110 klx and c)70 klx; using LED centered at d) 365 nm, e) 450 nm and f) 525 nm, and g) using natural sunlight; h) photochemical reduction of DS- Fe_3O_4 with simulated sunlight, and i) during the Fe_3O_4 dissolution at 92 °C.

The SEM images of some of the obtained Fe after pyrolytic reduction are observed and shown in **Figure 4-7**. It is clearly seen that the morphology of the obtained Fe remains the same shape as its corresponding Fe(II) oxalate dihydrate precursor. However, the surface of the particles became rough and porous resulting from the reduction process.
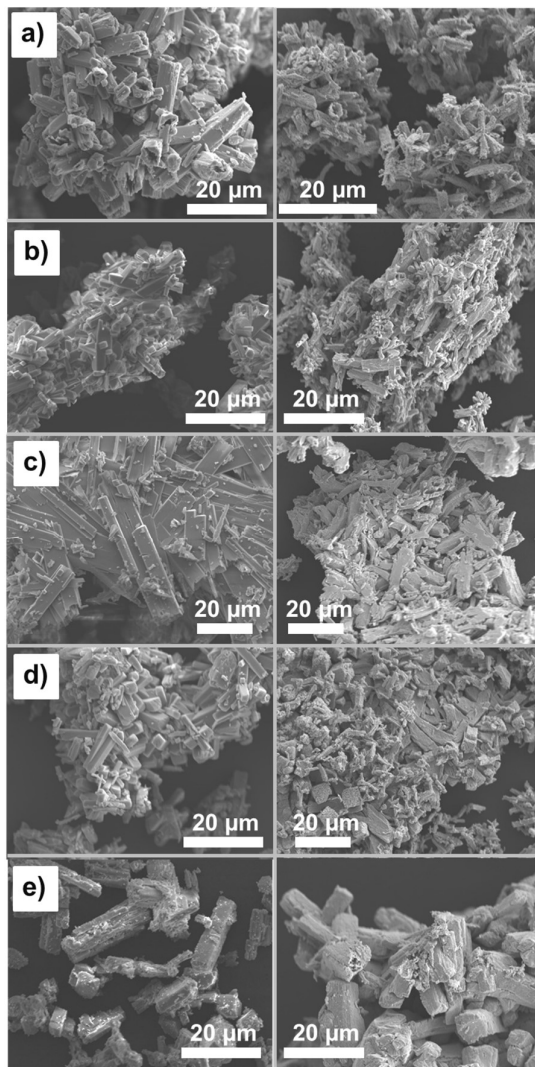
Figure 4-7. SEM images of the obtained metallic iron (right) from the $FeC_2O_4 \cdot 2H_2O$ precursor (left) obtaining from different conditions: photochemical reduction of $DS\text{-}Fe_2O_3$ by using a) simulated sunlight at 180 klx; b) LED-365 nm; c) using natural sunlight; d) photochemical reduction of $DS\text{-}Fe_3O_4$ with simulated sunlight, and e) during the Fe_3O_4 dissolution at 92 °C.

It is important to mention that some of the obtained metallic iron product was partially oxidized to FeO, and/or Fe_2O_3 by air (the results did not show here). Due to the obtained metallic iron contains many pores inside its structure resulting from the removal of oxygen by solid-state reduction, these porous structures increase the surface area and provide a tendency to re-oxidize and ignite which is also a problematic property of direct reduced iron (DRI). Thus, in this experiment, to avoid that phenomenon, the metallic iron was kept under a N_2 atmosphere for about 7 h before taking out of the reactor.

4.4 Conclusions

The thermal decomposition of iron(II) oxalate dihydrate was investigated with a particular purpose for its application for iron-making. The results showed the atmospheric condition strongly influences the thermal decomposition of $FeC_2O_4 \cdot 2H_2O$. The metallic iron can be produced under the 50%H_2/N_2 atmosphere at the temperature about 500 °C. However, CO and CO_2 are also generated during the reduction which can produce non-metallic iron at high temperatures. Thus, to maintain the product from pyrolytic reduction as only in form of metallic iron, the updraft type moving bed reactor is suggested to be used for the pyrolytic reactor used in the proposed iron-making process because it is able to minimize contact between pyrolysis gas and pyrolyzing solids at high temperature.

Moreover, the experimental results proved that all iron(II) oxalate dihydrate precipitates which were generated from both photochemical reduction and the precipitation during the dissolution of iron oxides could be reduced to the pure metallic iron in the pyrolytic reduction of the proposed process with the yield of 100% under the 50%H_2/N_2 atmosphere at 600 °C, which is much lower operation temperature compared to the production of DRI from iron ore in the current industry. However, since the obtained iron product has a low resistance to spontaneous ignition due to its structure, which is the same as DRI. Therefore, in large

production scale, it might be required the proper method for handling, such as, transportation under an inert atmosphere or converting it into a Hot Briquetted Iron (HBI).

4.5 References

[1] Hermanek, M.; Zboril, R.; Mashlan, M.; MacHala, L.; Schneeweiss, O. Thermal Behaviour of Iron(II) Oxalate Dihydrate in the Atmosphere of Its Conversion Gases. J. Mater. Chem. 2006, 16 (13), 1273–1280. https://doi.org/10.1039/b514565a.

[2] Zboril, R.; Machala, L.; Mashlan, M.; Hermanek, M.; Miglierini, M.; Fojtik, A. Structural, Magnetic and Size Transformations Induced by Isothermal Treatment of Ferrous Oxalate Dihydrate in Static Air Conditions. Phys. Status Solidi C Conf. 2004, 1 (12), 3583–3588. https://doi.org/10.1002/pssc.200405511.

[3] Macklen, E. D. Influence of Atmosphere on the Thermal Decomposition of Ferrous Oxalate Dihydrate. J. Inorg. Nucl. Chem. 1967, 29 (5), 1229–1234. https://doi.org/10.1016/0022-1902(67)80362-2.

[4] Kobayashi, H.; Ikeda, T.; Mitamura, T.; Kakizaki, K.; Hiratsuka, N. Preparation of Magnetic Particles by the Pyrolysis of Ferrous Oxalate in Various Atmospheres. Funtai Oyobi Fummatsu Yakin/Journal Japan Soc. Powder Powder Metall. 1996, 43 (1), 89–94. https://doi.org/10.2497/jjspm.43.89.

[5] Shoji, W.; Nobuaki, T.; Toshikazu, T. Preparation of Metallic Fine Particles by the Reduction of Fe-Co Double Oxalate. J. Soc. Mater. Sci. 1965, 14 (144), 736-740. https://doi.org/10.2472/jsms.14.736.

[6] Carles, V.; Alphonse, P.; Tailhades, P.; Rousset, A. Study of Thermal Decomposition of FeC2O4·2H2O under Hydrogen. Thermochim. Acta 1999, 334 (1–2), 107–113. https://doi.org/10.1016/s0040-6031(99)00133-1.

[7] Tyapkin PY, Petrov SA, Chernyshev AP, Gerasimov KB, Uvarov NF. Thermolysis of ferric oxalate in structured mesoporous silica. Mater Today Proc 2019;12:17–20. https://doi.org/10.1016/j.matpr.2019.02.207.

[8] Yang ZZ, Fu XM. Thermal decomposition process of FeC_2O_4. $2H_2O$ in the air. Adv Mater Res 2014;873:135–8. https://doi.org/10.4028/www.scientific.net/AMR.873.135.

[9] Feng Y, Hu T, Pu Z, Wu M, Mi J. Non-isothermal decomposition kinetics of FeC2O4·2H2O prepared by solid-state method aiming at the formation of Fe2O3. J Therm Anal Calorim 2015;122:947–53. https://doi.org/10.1007/s10973-015-4757-z.

[10] Smrčka D, Procházka V, Novák P, Kašlík J, Vrba V. Iron oxalate decomposition process by means of Mössbauer spectroscopy and nuclear forward scattering. AIP Conf Proc 2016;1781. https://doi.org/10.1063/1.4966008.

CHAPTER 5

Proof of Iron-Making Process Mediated by Oxalic Acid

5.1 Introduction

According to the results from dissolution of iron oxides using oxalic acid (in Chapter 2), photochemical reduction of the obtained Fe(III) oxalate aqueous solution (in Chapter3), and pyrolytic reduction of the obtained Fe(II) oxalate dihydrate (Chapter 4), the proposed iron-making process mediated by oxalic acid seems to be a promising iron-making process as it provides high yield in each process. More importantly, it is able to produce metallic iron with lower processing temperature. However, the iron oxides are used in chapters 2-4 are the commercial iron oxides without other metal impurities which can be affected the process performance.

Therefore, to examine and prove the proposed process under the selected conditions obtaining from the primary studies in chapters 2-4, three different iron sources containing other metals were used. Moreover, the technical challenges are also discussed in this chapter.

5.2 Materials and methods

5.2.1 Materials

Two natural iron ores (IO-A and IO-B) and a converter slag (CS) were used as the feedstock. Hematite (α-Fe_2O_3) and magnetite (Fe_3O_4) were purchased from Sigma-Aldrich and used for comparative experiments of iron dissolution. The samples were crushed into sizes below 38 μm and then subjected to the iron dissolution experiment. Anhydrous oxalic acid and analytical grade reagents, such as 1,10-phenanthroline, hydroxylamine, and ammonium acetate, were purchased from Wako Pure Chemical or Sigma-Aldrich.
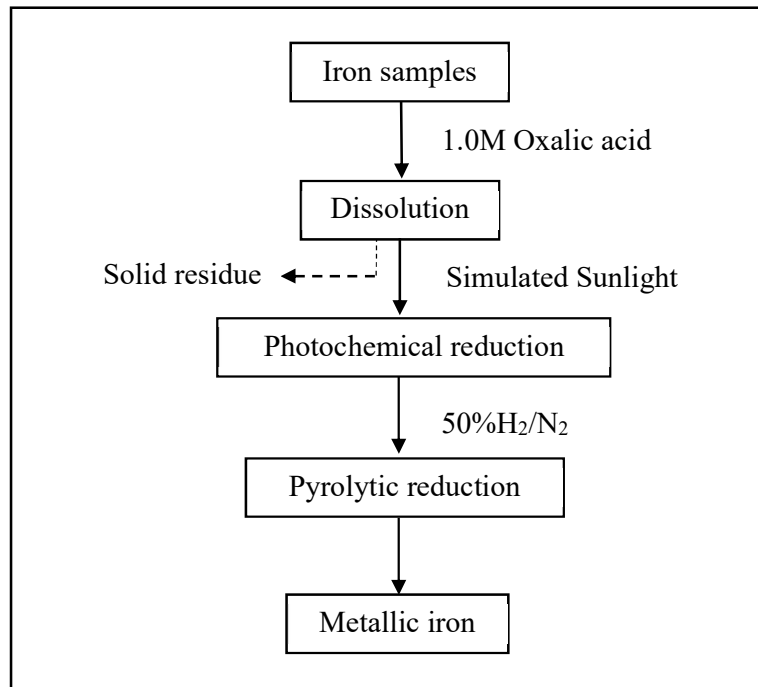
5.2.2 Proof of the proposed iron-making process

To obtain the highest amount of the metallic iron product, the most important step in this process is the dissolution of iron oxides. This is because the Fe(III) oxalate aqueous solution which is generated during the dissolution is the important iron intermediate for serving iron into this process. From the results in Chapter 2, it suggested that the dissolution temperature should be 92 °C to obtain the high dissolution rate without the solution being boiling, and the molar ratio of oxalic acid and iron (OxA/Fe) has to be at least 1.82 for the completion of dissolution.

Therefore, for the proof of the proposed iron-making process, 1M oxalic acid was chosen for leaching 0.50M iron from its sample (OxA/Fe =2) at 92 °C for 360 min. The dissolution and photochemical reduction process are performed in dark room (**Figure 5-1**) in order to protect from other interference lights.
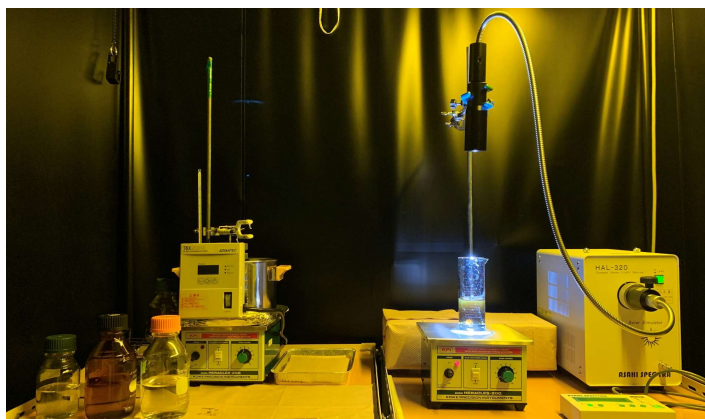

Figure 5-1. Photo of the dissolution (left) and photochemical reduction (right) set-up

The process flow diagram of the proof of the proposed iron-making process is shown in in **Scheme 5-1**, while the photos presenting the experimental procedure and the obtained product in each process is illustrated in **Figure 5-2.**

Scheme 5-1. Process flow diagram of the proof of the proposed iron-making process
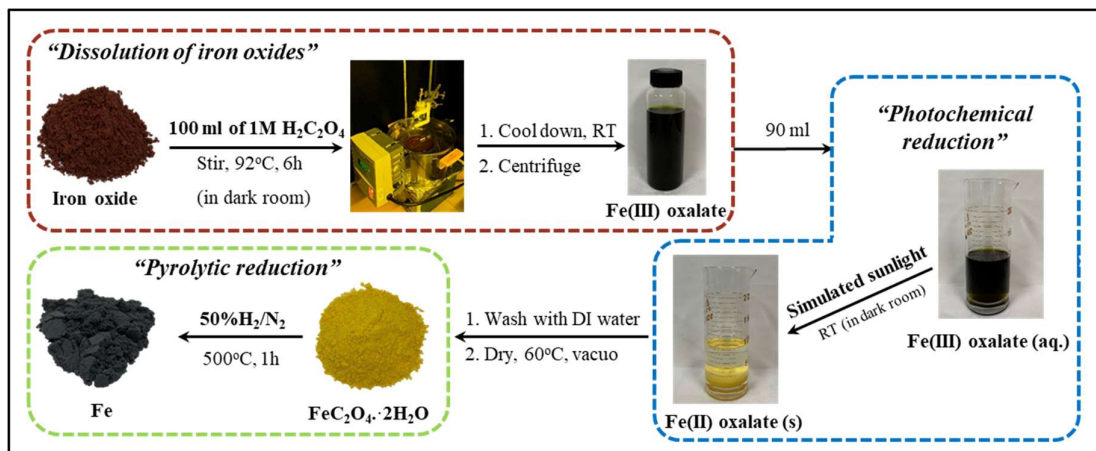
Figure 5-2. Photos of the experimental procedure and the obtained product in each process

5.2.2.1 Dissolution of iron oxides

The iron dissolution experiment was carried out in a 500 mL round-bottom flask in a dark room. To the flask, 4.0–15.1 g of the feedstock and 100 mL of 1.0 mol/L oxalic acid

were added. The loaded amount corresponded to 0.50 mol-Fe/L (0.62 mol-Fe/L for CS) at full iron dissolution. The slurry was stirred and heated to 92 °C with an oil bath for 360 min. During the dissolution, 30 μL of the aqueous solution was sampled at predetermined times to measure the concentration of dissolved iron. The sampling had little influence on the dissolution because of the small amount. The pH of the fresh oxalic acid solution was 0.5, which was not controlled throughout the experiment. After the test, the slurry was naturally cooled down to room temperature and centrifuged at 4000 rpm for 10 min to separate the aqueous solution from the remaining solids. The recovered solution was subjected to photochemical reduction, and the solids were washed until a neutral pH and dried at 60 °C in vacuo.

5.2.2.2 Photochemical reduction

The photochemical reduction was performed with a solar simulator (Asahi Spectra, HAL-320, Japan). 90 mL of aqueous solution, obtained from the iron dissolution, was added to an open-top cylindrical glass container with an inner diameter of 5 cm and then irradiated at 180 klx (350–1100 nm) under atmospheric conditions for 180–400 min with continuous stirring. The illuminance and photon flux density were measured on a light analyzer (NK System, LA-105). Conditions for sampling during reaction and the product separation were the same as those in the iron dissolution.

5.2.2.3 Pyrolytic reduction

In the pyrolytic reduction, about 1 g of solid product obtained in the photochemical reduction was heated under a flow of 50% H_2/N_2 at the heating rate of 5 °C/min to 500 °C with 1 h of holding time. The solid products obtained in each step of the conversion are hereafter denoted by S_{STP1}, S_{STP2}, and S_{STP3} for the iron dissolution (step 1), photochemical reduction (step 2), and pyrolytic reduction (step3), respectively, or, for example, by $S_{IO-A,STP1}$ with the name of the feedstock.

CHAPTER 5

5.2.3 Characterizations

The concentration of iron dissolved in the solution was analyzed by absorption spectroscopy with a UV-Vis spectrophotometer (PerkinElmer, Lambda 365). To the solution, prescribed amounts of 1,10-phenanthroline, hydroxylamine, and ammonium acetate were added as the complexing agent, reducing agent, and buffering agent, respectively, immediately after the sampling in the darkroom, and then the solution was subjected to the spectroanalysis. The analysis measured concentrations of both Fe^{2+} and Fe^{3+}. The Fe^{2+} concentration was determined from the solution prepared in the absence of a reductant, and the concentration of Fe^{3+} was calculated by the difference.

The metallic composition of feedstock and solid products was analyzed with a wavelength dispersive X-ray fluorescence (XRF) spectrometer (Rigaku, Supermini200). The crystalline structure was analyzed by X-ray diffraction (XRD) on a Rigaku, TTR-III with Cu Kα radiation at 50 kV and 30 mA. The iron content in samples was calculated from the metallic composition and crystalline structure. The mass release curve in the pyrolytic reduction was analyzed on a thermogravimetric analyzer (Hitachi Hi-Tech Science, STA7200) that was operated with a heating rate of 5 or 10 °C/min and gas flow rate of 300 mL/min.

5.3 Results and dissolution

IO-A, IO-B, and CS were all low-grade iron sources and, therefore, not available for BF as the direct feedstock. The as-received IO-A was composed mostly of goethite (α-FeOOH), but it was used after calcination at 500 °C to change the goethite to α-Fe$_2$O$_3$. The Fe contents were 61.5, 52.1, and 23.0 wt%, respectively. The structural characteristics are presented in **Table 5-1** and **Figures 5-3 and 5-4**.
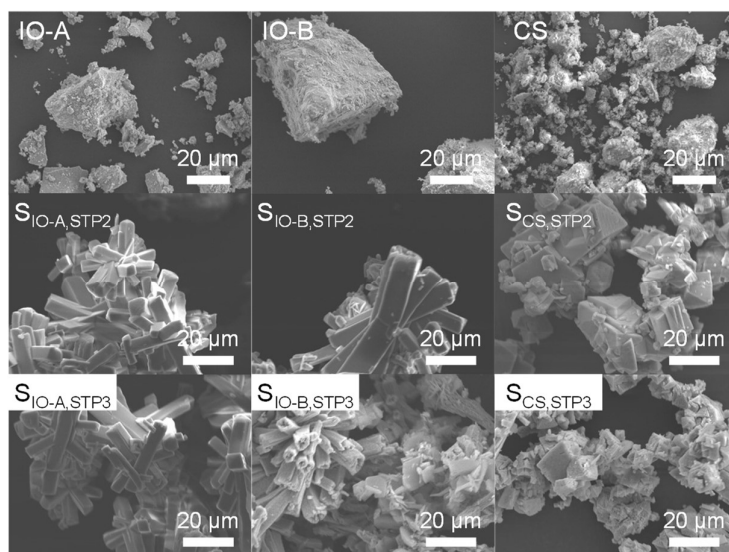
Table 5-1. Metallic composition of feedstock and solid products from photochemical reduction (S_{STP2}) and pyrolytic reduction (S_{STP3})

	IO-A	$S_{IO-A,STP2}$	$S_{IO-A,STP3}$	IO-B	$S_{IO-B,STP2}$	$S_{IO-B,STP3}$	CS	$S_{CS,STP2}$	$S_{CS,STP3}$
Composition (wt%-metal)									
Fe	93.3	99.7	99.7	82.3	96.3	94.4	33.9	77.6	80.5
Mg	–	–	–	-	–	–	1.1	11.8	6.8
Al	2.8	–	–	4.4	–	–	0.7	0.1	0.1
Si	3.3	–	–	7.5	–	–	4.1	0.1	0.0
P	–	–	–	0.1	–	–	1.1	<0.1	–
S	<0.1	–	–	–	–	–	0.2	–	–
K	–	–	–	–	–	–	<0.1	–	<0.1
Ca	0.3	0.1	0.1	4.6	3.1	4.8	52.6	0.9	0.8
Ti	<0.1	–	–	–	–	–	0.8	–	0.1
V	–	–	–	–	–	–	0.3	<0.1	<0.1
Cr	–	–	–	0.1	–	–	<0.1	<0.1	-
Mn	0.2	0.2	0.2	0.7	0.7	0.8	5.0	9.5	11.0
Cu	–	–	–	0.3	–	–	–	–	–
Zn	<0.1	–	–	–	–	–	–	–	–
Sr	<0.1	–	–	–	–	–	–	–	–

From the characterization results, magnetite was the major iron oxide in IO-B. These iron ores also contained other elements, such as Si, Al, and Ca. CS was a by-product of the BF iron-making process. The iron content was very low. Due to the richness in Ca, CS is used as fertilizers and building materials. Recycling to the BF process is an option of its application but is often hindered by the presence of phosphorus that is a deleterious element, affecting the quality of product steel even with the low content.
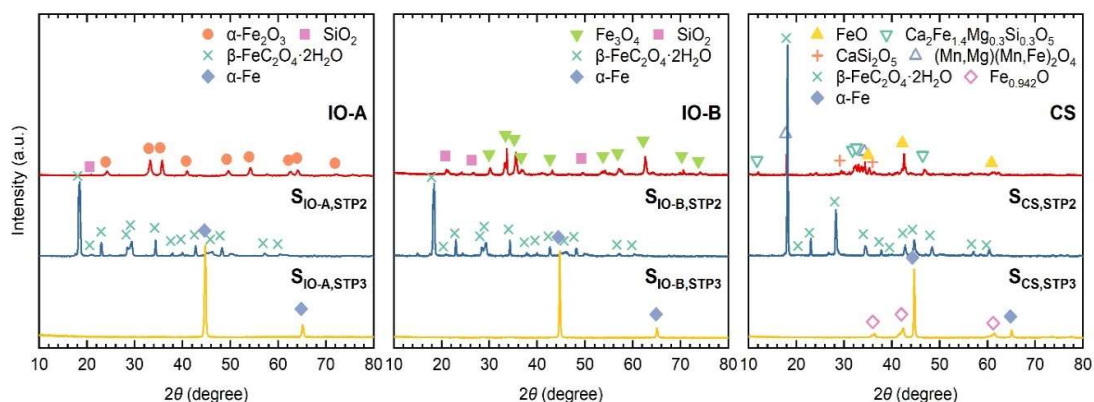
Figure 5-3. XRD pattern of feedstock and solid products from photochemical reduction (S$_{STP2}$) and pyrolytic reduction (S$_{STP3}$). *Reprinted with permission from Santawaja et al. 2020. Copyright 2020 American Chemical Society.*



Figure 5-4. SEM image of feedstock and solid products from photochemical reduction (S$_{STP2}$) and pyrolytic reduction (S$_{STP3}$). *Reprinted with permission from Santawaja et al. 2020. Copyright 2020 American Chemical Society.*

The three-step conversion of these low-grade materials was examined. The iron dissolution was carried out with 1.0 mol/L oxalic acid and 0.50 mol-Fe/L (or 0.62 mol/L for CS) iron feedstock at full dissolution. For achieving a high iron productivity, the product liquid

from this step is required to have a higher iron concentration. The solubility of iron in water as Fe(III) oxalate, which was the most abundant chemical form of dissolved iron, was confirmed to be over 1 mol-Fe/L, as presented in **Figure S5-2**. The employment of 0.50 mol-Fe/L (or 0.62 mol/L for CS) in the dissolution experiment was due to the solubility of oxalic acid at 1.0 mol/L around room temperature. The molar ratio of oxalic acid to iron at full dissolution (= 2.0) was slightly higher than that in the stoichiometry of eq. 1 (= 1.5). The illuminance of 180 klx in the photochemical reduction simulated a direct daylight in summer (> 100 klx). Iron dissolution and photochemical reduction were terminated after 6 h, which was sufficient to reach plateau conversion under the employed conditions as shown later.
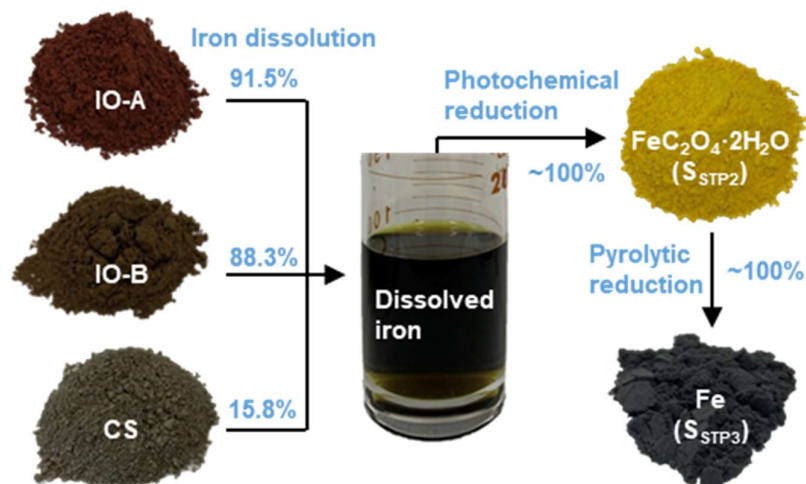
Figure 5-5. Iron recovery at each step of conversion.

Adapted with permission from Santawaja et al. 2020. Copyright 2020 American Chemical Society.

In all experiments, iron dissolution, photochemical reduction, and pyrolytic reduction produced a dark green aqueous solution, yellow solid (S_{STP2}), and grayish black solid (S_{STP3}), respectively (**Figure 5-5**). XRD analysis identified the main components of the solids as β-$FeC_2O_4 \cdot 2H_2O$ and α-Fe, respectively. The results clearly proved the possibility to make iron using the method proposed in this study.

CHAPTER 5

Of particular interest and importance was the improvement of iron purity in the conversion, which never occurs in the reduction step of conventional iron-making methods. The iron purity of 33.9–93.3% in the feedstock improved to over 80.5%, reaching 99.7% for $S_{IO-A,STP3}$. The first step, iron dissolution, was mainly responsible for this and chemoselectively dissolved iron.

Table 5-2. Metallic composition of solid products from iron dissolution (S_{STP1})

	$S_{IO-A,STP1}$	$S_{IO-B,STP1}$	$S_{CS, STP1}$
Composition (wt%-metal)			
Fe	75.4	67.4	19.3
Mg	–	–	1.8
Al	2.9	2.4	0.1
Si	20.8	22.2	4.0
P	–	<0.1	–
S	<0.1	–	–
Ca	–	6.0	70.8
Ti	0.8	–	0.4
V	–	–	<0.1
Cr	–	0.2	0.1
Mn	0.2	0.5	3.4
Cu	–	1.2	–

As seen in **Table S5-2**, undissolved solids (S_{STP1}) contained more other metals than the feedstocks. The iron was further purified by photochemical reduction, which separated iron as the solid. In other words, there was a double chemical system for iron purification in the process. It is reasonable to conclude that the major portions of typical trace elements, such as Al, Si, P, and S, were removed entirely by the system. On the other hand, the contents of impurity metals such as Ca, Mg, and Mn were not low for $S_{IO-B,STP3}$ and $S_{CS,STP3}$. Ca and Mg were unlikely to

react similarly to Fe in the sequential conversion due to the very low solubility of their oxalates in water. [1] The high acidity of water improves the solubility, but the pH of the solution was maintained at well below 1.0 even after photochemical reduction. The most probable reason for Ca and Mg inclusion in the iron product was an incomplete separation of their oxalates in the solid form from the aqueous solution after iron dissolution. The formation of solid oxalate was, in fact, confirmed for Ca in the S_{STP1}, as shown in **Figure 5-6.**
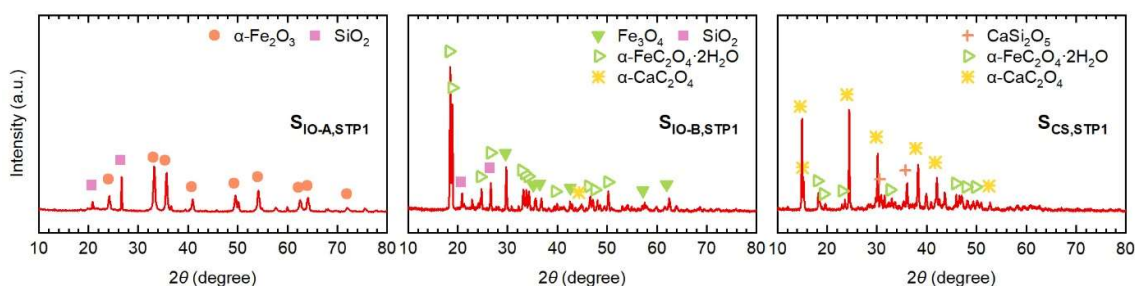
Figure 5-6. XRD pattern of solid product from iron dissolution (S_{STP1}). *Reprinted with permission from Santawaja et al. 2020. Copyright 2020 American Chemical Society.*

A portion of Ca and Mg oxalates with small crystallite sizes was likely transferred to the photochemical reduction and then physically deposited together with Fe(II) oxalate. Improving the separation process may solve this problem, but the consumption of oxalic acid by the presence of Ca and Mg is unavoidable, which requires a greater feeding of oxalic acid into the process. The inclusion of Mn was considered to occur in a different pathway because Mn(III) oxalate is photochemically active as reported by Porter et al. [2] who stated that, among the trivalent transition metal oxalates, Fe, Co and Mn were converted into the divalent forms upon light irradiation. Therefore, some transition metals such as Mn undergo reactions similar to those for Fe in the dissolution and photochemical reduction steps and are inevitably included in the iron product.

CHAPTER 5

The obtained Fe(II) oxalate dihydrate was the orthorhombic crystal (β-FeC$_2$O$_4$·2H$_2$O), as seen in the XRD patterns (**Figure 5-3**), showing the occurrence of a reaction at an oxalic acid to iron ratio close to stoichiometry. While, the S$_{CS,STP2}$ showed higher crystallinity than S$_{IO-A,STP2}$ and S$_{IO-B,STP2}$. The difference was also evident in the SEM images (**Figure 5-4**), where S$_{IO-A,STP2}$ and S$_{IO-B,STP2}$ consisted of 3–8×10–25 μm square rods, whereas orthorhombic S$_{CS,STP-2}$ was layered to form a pyramidal structure. The reason for this structural difference was unclear but possibly related to the presence of Ca, Mg and Mn in S$_{CS,STP-2}$ that reacted with oxalic acid competitively with Fe and inhibited the directional growth of β-FeC$_2$O$_4$·2H$_2$O.
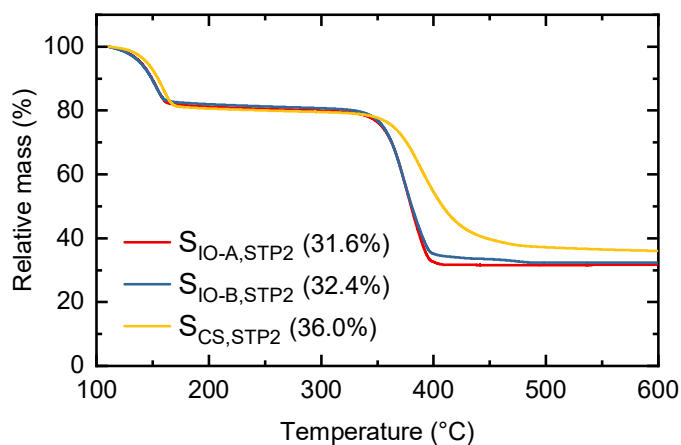
Figure 5-7. Pyrolytic reduction of solid product from photochemical reduction (S$_{STP2}$) in TGA: sample 3 mg, heating rate 5 °C/min, and H$_2$/N$_2$ (50%) 300 mL/min. The percentage in parenthesis shows the relative mass at 600 °C. *Reprinted with permission from Santawaja et al. 2020. Copyright 2020 American Chemical Society.*

Nevertheless, all the S$_{STP2}$ samples showed similar pyrolytic characteristics as shown in **Figure 5-7**. although S$_{CS,STP-2}$ needed higher temperatures to be reduced and showed a higher S$_{STP-3}$ yield (= the relative mass of 36.0% at 600°C) because of the high crystallinity and content of impurity metals. These characteristics of S$_{CS,STP2}$ resulted in incomplete conversion to α-Fe in the pyrolytic reduction (at 500°C) as the XRD pattern showed the presence of Fe$_{0.942}$O (**Figure 5- 3**). On the other hand, an interesting observation from the SEM images (**Figure 5-**

4) was the maintenance of morphology after pyrolytic reduction for all of the S_{STP2}, with only a small shrinkage. This was caused by reduction at the low temperatures, avoiding the agglomeration of particles.
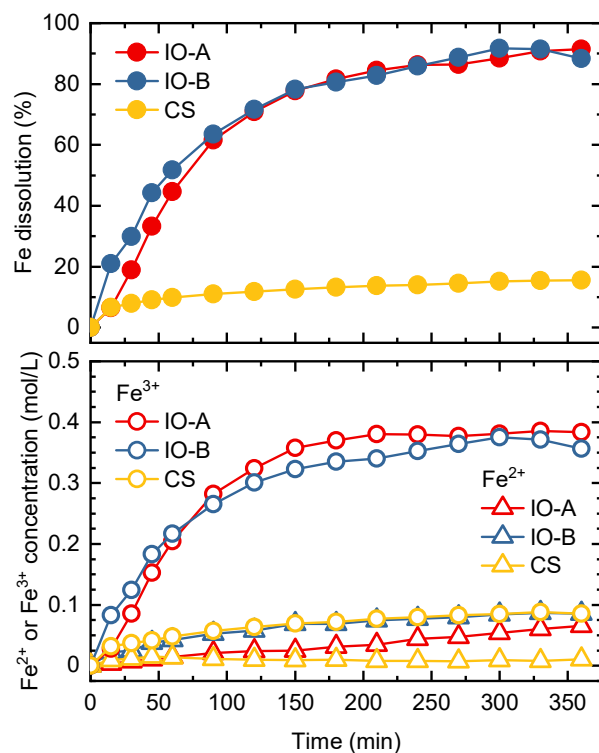
Figure 5-8. Iron dissolution: time-dependent change of Fe dissolution and Fe^{2+} or Fe^{3+} concentration. Feedstock 0.50 mol-Fe/L (0.62 mol-Fe/L for CS), Oxalic acid 1.0 mol/L, 92°C. *Reprinted with permission from Santawaja et al. 2020. Copyright 2020 American Chemical Society.*

The recovery (yield) of iron in S_{STP3} from the feedstock is important to the process. **Figure 5-5** shows the recovery of iron at each step of conversion. Because iron is not volatile, the recovery in pyrolytic reduction was 100%. As shown later, dissolved iron from the iron dissolution almost completely precipitated in the photochemical reduction. Therefore, the iron recovery of the overall process is determined by that during iron dissolution. The details of iron dissolution are presented in **Figure 5-8**. The rate of iron dissolution decreased with time, and the dissolution reached 91.5%, 88.3%, and 15.8% for IO-A, IO-B and CS, respectively, at 6 h.

CHAPTER 5

The low recovery of iron as dissolved iron from CS is explained by the shortage of oxalic acid that also reacted with other metals to form the oxalates, as discussed above.

To investigate the reasons for the incomplete iron recovery from IO-A and IO-B, dissolution tests were carried out with α-Fe_2O_3 and Fe_3O_4, which were their main components, respectively, and the results are plotted in **Figure 5-9.**

The iron dissolution from α-Fe_2O_3 was 97.1% at 6 h, but this did not mean incomplete dissolution because the remaining solid was Fe(II) oxalate that formed through dissolution. More importantly, α-Fe_2O_3 dissolved faster than IO-A. For example, the time needed to reach an iron dissolution above 80% was 60 and 150 min, respectively. The comparison indicated that α-Fe_2O_3 in the ore was less accessible to oxalic acid, compared to the pure one, by the presence of other metals. The small portion was considered to be protected by materials that were insoluble to oxalic acid, resulting in an incomplete dissolution of 91.5%. On the other hand, dissolution of Fe_3O_4 was the fastest among samples tested in the present study and showed the highest iron dissolution at 30 min. This was due to the quick release of Fe^{2+} and the resulting autocatalysis. However, as observed in the dissolution of α-Fe_2O_3, Fe^{2+} not only catalyzed the dissolution but also contributed to the formation of Fe(II) oxalate and its precipitation, resulting in a relatively low iron recovery of 76.1%. One of the reasons for the lower iron recovery from IO-B, compared to that from IO-A, was thus the precipitation of Fe(II) oxalate. This was confirmed by the XRD pattern of $S_{IO-B,STP1}$ (**Figure 5-6**). Due to the presence of excess oxalic acid, Fe(II) oxalate that precipitated during the iron dissolution was in the α-form. Considering the abundant formation of catalytic Fe^{2+}, the dissolution rate of IO-B should be fast, but it was not. The similarity of the dissolution profiles between IO-A and IO-B was likely to be coincidental, but it was apparent from these results that the physicochemical structure of iron ore hinders the intrinsic dissolution rates of iron oxides.
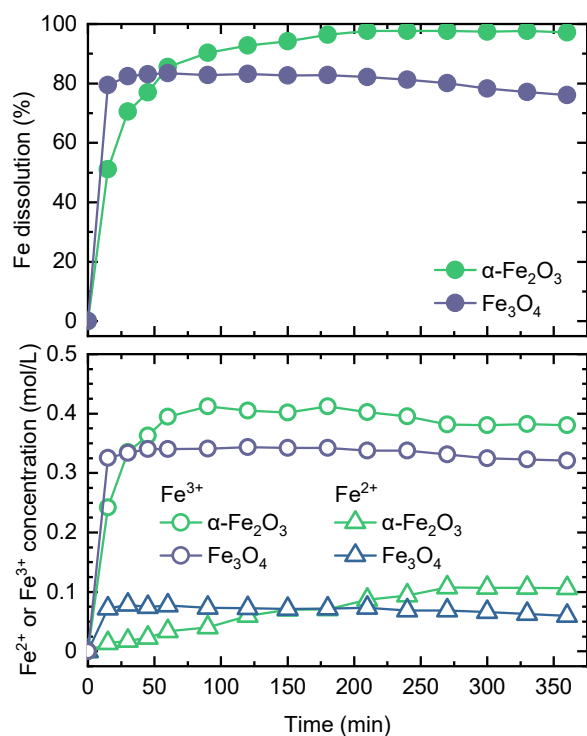
Figure 5-9. Iron dissolution with reagent grade iron oxides. Feedstock 0.50 mol-Fe/L, Oxalic acid 1.0 mol/L, and 92 °C. *Reprinted with permission from Santawaja et al. 2020. Copyright 2020 American Chemical Society.*

The conversions of iron dissolved from different feedstocks during photochemical reduction are plotted in **Figure 5-10**. The iron was dissolved in the solution as Fe^{3+} or Fe^{2+} (**Figure 5-10** bottom). They presented mainly in the forms of Fe(III) and Fe(II) oxalates, respectively, and Fe^{2+} could be a free divalent cation because it is a stable ion in a highly acidic aqueous solution. [3] As seen in the changes in Fe^{2+} and Fe^{3+} concentrations with time, the dissolved iron was near-completely recovered from the solution as the precipitated Fe(II) oxalate after 6 h. The presence of Fe^{2+}, which was not involved in the photochemical reduction outlined in eq. 2, did not disturb the iron recovery.
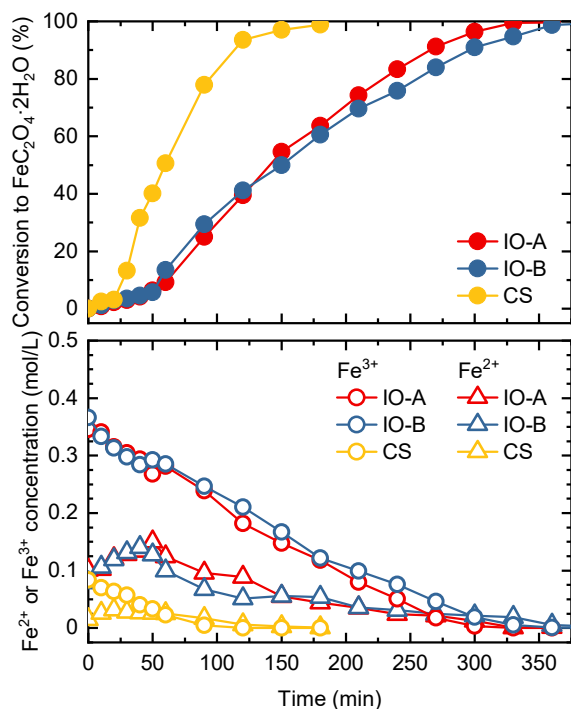
Figure 5-10. Photochemical reduction of dissolve iron with solar simulator at 180 klx and room temperature: time-dependent change of conversion to $FeC_2O_4 \cdot 2H_2O$ and Fe^{2+} or Fe^{3+} concentration. *Reprinted with permission from Santawaja et al. 2020. Copyright 2020 American Chemical Society.*

The conversion profile was separated into three stages. At the initial stage, Fe^{3+} was reduced to Fe^{2+}, but the precipitation of Fe(II) oxalate hardly occurred, rendering the rate of conversion slow. During the initial stage, the Fe^{3+}/Fe^{2+} ratio continued to decrease as shown in **Figure S5-2**. When the ratio reached around 2, the second stage, significant precipitation of Fe(II) oxalate, was initiated. The abundance of dissolved Fe^{2+} in the initial solution was, in this regard, rather beneficial because it contributed to shortening the duration of the initial stage. The rates of conversion at the second stage were in a narrow range of 0.14, 0.13, and 0.11 mol/min for the solutions from IO-A, IO-B and CS, respectively. These were close to the rate of 0.19 mol/min, which was calculated under the assumption that all photons radiating over the solution surface in the wavelength of 290–570 nm. [3-9] (1680 µmol/m²/s) were fully used for

the reaction in eq. 2 with quantum efficiency at unity. Thus, the reaction of concentrated iron solutions produced in this study basically followed the chemistry of photochemically reactive Fe(III) oxalate, where the reaction rate is proportional to the light intensity and improved by enlargement of the irradiation area. In the last stage of conversion, the solution was a dense slurry consisting of diluted Fe(III) oxalate aqueous solution and Fe(II) oxalate particles, and thereby the efficiency of light absorption was low, resulting in a decrease in the rate of conversion

5.4 Conclusions

A three-step iron-making process was proposed and investigated using different types of iron-containing materials. The experimental results showed promising performance as an iron-making method. The chemical selectivity of iron dissolution and photochemical reduction enabled the obtainment of product iron with a purity of 80.5–99.7 wt% (on a metal basis) from the feedstocks consisting of 33.9–93.3 wt% iron. The highest temperature used for completing the reduction to metallic iron was only 500 °C due to the pyrolysis characteristics of Fe(II) oxalate. On the other hand, the iron dissolution step determined primarily the overall yield and purity of the produced iron. Ca and Mg reacted with oxalic acid to form water-insoluble oxalates, causing its shortage for the iron dissolution. Transition metals such as Mn were inevitably included in the produced iron. As a result, iron recovery from CS, having high contents of these unwanted metals, was limited to 15.8%. The iron recoveries from IO-A and IO-B were 91.5 and 88.3%, respectively. The proposed method also allowed for the use of powdered ore, which has not been the feedstock in conventional iron-making except for the smelting reduction. The availability of diverse feedstocks will be a great advantage considering the decreasing quality of iron ore globally.
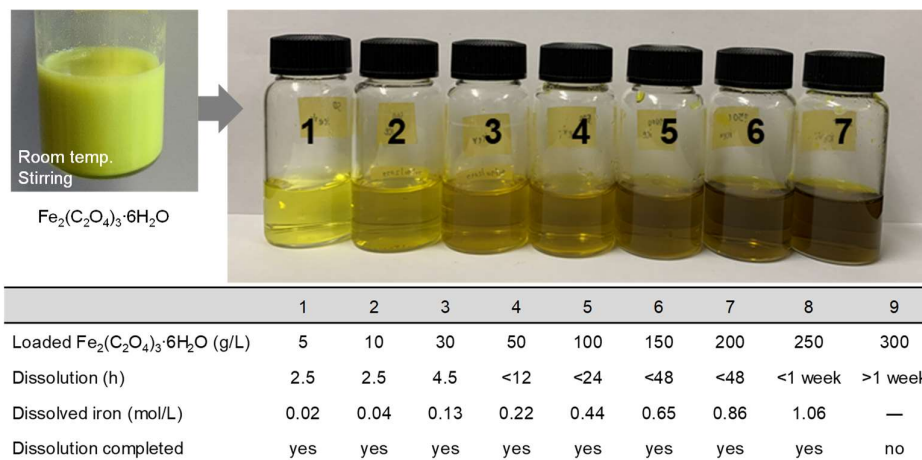
CHAPTER 5

5.5 References

[1] Verma, A.; Kore, R.; Corbin, D. R.; Shiflett, M. B. Metal Recovery Using Oxalate Chemistry: A Technical Review. Ind. Eng. Chem. Res. 2019, 58 (34), 15381–15393. https://doi.org/10.1021/acs.iecr.9b02598.

[2] Porter, G. B.; Doering, J. G. W.; Karanka, S. Photolysis of Transition Metal Oxalato Complex Ions. J. Am. Chem. Soc. 1962, 84 (21), 4027–4029. https://doi.org/10.1021/ja00880a010.

[3] Taxiarchou, M.; Panias, D.; Douni, I.; Paspaliaris, I.; Kontopoulos, A. Dissolution of Hematite in Acidic Oxalate Solutions. Hydrometallurgy 1997, 44 (3), 287–299. https://doi.org/10.1016/s0304-386x(96)00075-8.

[4] Parker, C. A.; Hatchard, C. G. Photodecomposition of Complex Oxalates. Some Preliminary Experiments by Flash Photolysis. J. Phys. Chem. 1959, 63 (1), 22–26. https://doi.org/10.1021/j150571a009.

[5] Dudeney, A. W. L.; Tarasova, I. I. Photochemical Decomposition of Trisoxalatoiron(III): A Hydrometallurgical Application of Daylight. Hydrometallurgy 1998, 47 (2–3), 243–257. https://doi.org/10.1016/s0304-386x(97)00049-2.

[6] Dong, Y.; Chen, J.; Li, C.; Zhu, H. Decoloration of Three Azo Dyes in Water by Photocatalysis of Fe (III)-Oxalate Complexes/H_2O_2 in the Presence of Inorganic Salts. Dye. Pigment. 2007, 73 (2), 261–268. https://doi.org/10.1016/j.dyepig.2005.12.007.

[7] Deng, N.; Wu, F.; Tian, S.; Fang, T. Photodegradation of Dyes in Aqueous Solutions Containing Fe(III)-oxalato Complexes. Chemosphere 1997, 35 (11), 2697–2706. https://doi.org/10.1016/S0045-6535(97)00327-5.

[8] Yuegang, Z.; Jürg, H. Formation of Hydrogen Peroxide and Depletion of Oxalic Acid in Atmospheric Water by Photolysis of Iron(III)-Oxalato Complexes. Environ. Sci. Technol. 1992, 26 (5), 1014–1022. https://doi.org/10.1021/es00029a022.

[9] Zhou, D.; Wu, F.; Deng, N. Fe(III)-Oxalate Complexes Induced Photooxidation of Diethylstilbestrol in Water. Chemosphere 2004, 57 (4), 283–291. https://doi.org/10.1016/j.chemosphere.2004.05.043.

5.6 Supporting information

	1	2	3	4	5	6	7	8	9
Loaded $Fe_2(C_2O_4)_3 \cdot 6H_2O$ (g/L)	5	10	30	50	100	150	200	250	300
Dissolution (h)	2.5	2.5	4.5	<12	<24	<48	<48	<1 week	>1 week
Dissolved iron (mol/L)	0.02	0.04	0.13	0.22	0.44	0.65	0.86	1.06	—
Dissolution completed	yes	yes	yes	yes	yes	yes	yes	yes	no

Figure S5-1. Dissolution of $Fe_2(C_2O_4)_3 \cdot 6H_2O$ (commercial reagent purchased from Sigma-Aldrich) in pure water. *Reprinted with permission from Santawaja et al. 2020. Copyright 2020 American Chemical Society.*
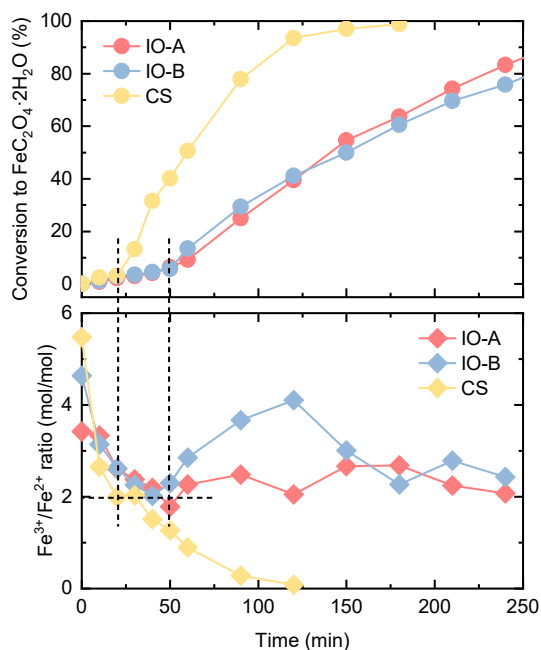
Figure S5-2. Time-dependent change of Fe^{3+}/Fe^{2+} ratio (bottom) in photochemical reduction.

Reprinted with permission from Santawaja et al. 2020. Copyright 2020 American Chemical Society.

CHAPTER 6

General Conclusions and Future Challenges

Global iron and steel production continue to expand. The iron-making industry is, however, one of the main contributors to global warming due to its reliance on fossil fuel-based high temperature processes. Therefore, alternative green approaches to iron-making are highly desired.

This research work proposed a novel iron-making process mediated by oxalic acid which consists of a sequence of known reactions: the dissolution of iron from iron ore using oxalic acid to obtain a Fe(III) oxalate aqueous solution, followed by the photochemical reduction of Fe(III) oxalate to Fe(II) oxalate as a solid precipitate, and the pyrolytic reduction of Fe(II) oxalate to metallic iron. By harnessing the chemical characteristics of oxalic acid and iron oxalates, the method is expected to produce high-quality iron at low temperatures. Moreover, the recovery of carbon oxides, generated during iron-making, for the synthesis of oxalic acid enables the iron-making without carbon in stoichiometry. This study aims to study the three key reactions of the proposed process for finding the optimum conditions in each process which could bring the proposed process to have high performance and examine the proposed process in a lab-scale experiment.

The dissolution of iron oxides with oxalic acid, the first step of the proposed iron-making process, is considered as an important step in the proposed process since it not only is used for serving the iron into the process but also determines the yield and purity of iron product. Moreover, in the case where the light source is fully available, it is the rate-determining step of the process. From the current results, it is possible to increase the dissolution iron concentration in iron(III) oxalate aqueous solution by simply increasing the molar

concentration of oxalic acid (OxA) together with an initial iron (Fe) in the iron oxide sample with the ratio of OxA/Fe more than 1.82. However, for developing a scaling-up process, there are two important factors that need to consider; one is the solubility of oxalic acid which is limited as about 1 mol/L at room temperature, whereas the other is the pulp density (liquid/solid ratio) because it directly affects the diffusion and accessibility of oxalic acid into iron samples. Moreover, the precipitation of iron(II) oxalate dihydrate during the dissolution should be avoided, especially when the iron sample contains Fe(II) lattices, such as Fe_3O_4 and FeO, because it causes the loss of iron precursor during the process. Although it was proved in this study that the precipitate can produce the metallic iron in pyrolytic reduction step, the complete separation from the solid residue might be difficult.

For the photochemical reduction, to produce iron (II) oxalate dihydrate precipitate, the results showed that, by using the simulated sunlight, the rate of conversion is approximately proportional to the of light intensity (PFD), whereas sources of iron used to produce iron (III) oxalate solution, and the depth of solution did not show a significant effect on the rate of conversion. When the LED lights were used, the results confirmed that light in the wavelength of 365-550 nm could induce photochemical reduction. Moreover, it reveals that apart from the light intensity, the wavelength of light also plays an important role in the rate of reaction: light near the UV-region provides a significantly higher rate of reduction. Natural sunlight could reduce the iron(III) oxalate aqueous solution, but it required more time to complete the reaction due to the weather condition dependency. The obtained Fe(II) oxalate precipitates in all conditions are indexed to be pure $FeC_2O_4 \cdot 2H_2O$, however, they are slightly different in terms of their structures, crystallinities, and crystal sizes, which probably results from the different rate of conversion.

For the pyrolytic reduction, the results show that the metallic iron could be produced from the obtained Fe(II) oxalate dihydrate precipitate from both photochemical reduction and dissolution at 500 °C under 50%H_2/N_2 atmosphere. However, CO and CO_2 are also generated during the reduction, which can produce non-metallic iron at high temperatures. Thus, to maintain the product from the pyrolytic reduction as only in the form of metallic iron, the updraft type moving bed reactor is recommended and shown in **Figure 6-1**.
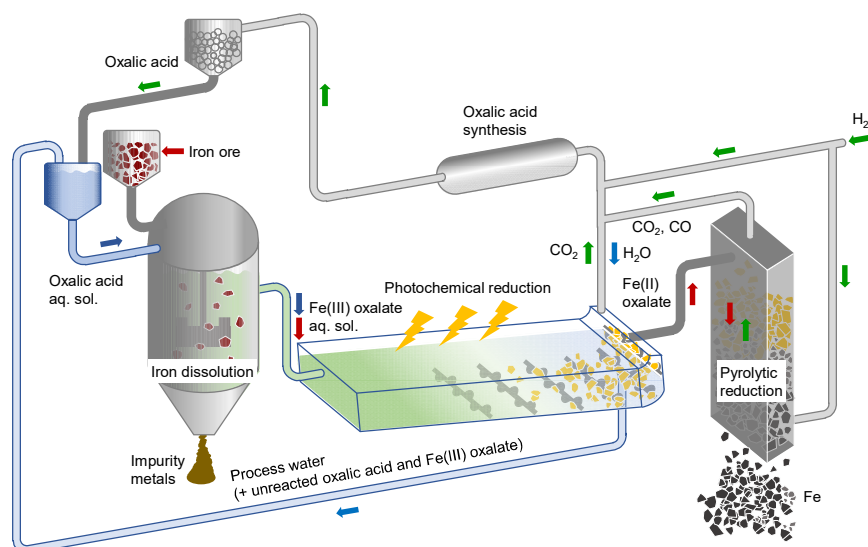
Figure 6-1. Outline of the process flow. *Reprinted with permission from Santawaja et al. 2020. Copyright 2020 American Chemical Society.*

It is worth mentioning that the proposed iron-making process requires much lower temperature for iron production compared to the production of direct reduction iron (DRI) from iron ore in the current alternative iron-making process. However, due to the solid-state reduction, the obtained metallic iron contains many pores inside its structure. These porous structures increase the surface area and provide a tendency to re-oxidization and ignition which requires the proper method for handling such as transportation under an inert atmosphere or converting it into a Hot Briquetted Iron (HBI), same as DRI

GENERAL CONCLUSIONS AND FUTURE CHALLENGES

According to the proof of the proposed process results, the process seems to be a promising iron-making process as three different iron sources were successfully converted into metallic iron. The yield and quality (purity) of iron product depended on the metallic composition of the feedstock. In the absence of impurity metals, near-complete recovery of pure iron was possible. Alkaline earth and transition metals were identified as impurities that affected process performance and product quality. The iron dissolution needed a relatively long reaction time to achieve sufficient conversion under the conditions employed in this study, rendering it a rate-determining step that influenced overall iron productivity. The photochemical reduction needed 6 h to reach full conversion, with the area fraction of solution surface exposed to light being 17%. Because the area percentage of the photolysis pool projected in the process (**Figure 6-1**) is to be close to 50%, the reaction rate can be more than double at least. The rate of pyrolytic reduction is basically very fast. Therefore, the rate-determining step of the process is identified to be iron dissolution in an ideal case where solar light is fully available. **Figure 6-2** shows the iron productivity as functions of reaction time and iron concentration. For achieving as high productivity as that of BF (ca. 2 ton-Fe/day/m^3), further technological development should be geared toward harnessing the bottom-light in the figure. The present experimental results regarding plateau iron dissolution indicated iron productivity well below 0.5 ton-Fe/day/m^3 (5–6 h and 0.4–0.5 mol-Fe/L). A straightforward way to improve productivity is to increase oxalic acid concentration, iron loading, and dissolution temperature. However, the application of temperatures above 100 °C necessitates the use of a pressure-tight reactor, which probably poses technical challenges considering the need to operate it under highly acidic conditions. Alternative strategies may involve the addition of chemicals to activate the dissolution, but it is imperative they are less costly and have no negative influence on the product iron for the purposes of iron-making.
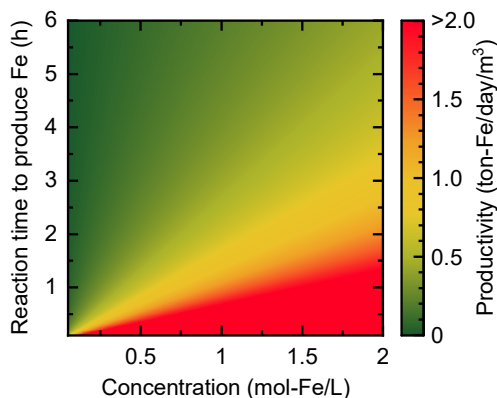
Figure 6-2. Iron productivity as functions of reaction time and iron concentration in a batch operation. *Reprinted with permission from Santawaja et al. 2020. Copyright 2020 American Chemical Society.*

The synthesis of oxalic acid from CO_2 is vital to process sustainability. Direct synthesis is an emerging area of research but has a long way to go to become an industrial technology. Indirect synthesis via CO or biomass is a realistic option if a conversion system with economic and energetic rationality is found. It is also important to confirm the generation of CO_2 and CO from iron-making, according to the proposed stoichiometry, and to design reactors that enable their recovery along with reactions in each step of conversion. Even with the successful development of technologies for iron-making and oxalic acid synthesis, the process cannot be operated stand alone because of the lack of H_2 and a heat source. Renewable H_2 and heat sources are preferable to accomplish the goal of net-zero emissions. For example, a thermally integrated biomass gasification–fuel cell system has the potential to supply H_2 and electricity (used as Joule heat) in a carbon-neutral or -negative manner. These technologies, however, have not yet reached an industrial scale that meets the requirements of iron-making. From a short- or middle-term viewpoint, integration with conventional iron-making processes is a feasible strategy moving forward. H_2 is available from coke oven gas, and the conventional processes waste huge amounts of heat within a variety of temperature ranges, below 500°C in

particular. This process integration is also beneficial for receiving the feedstock (e.g., waste powdered iron ore from the sintering process) and transferring the produced crude iron to downstream processes.

It is to be noted that the proposed process is location-dependent because the intensity and duration of daylight quantitatively determine performance. A process design (e.g., additional photolysis pools for the storage of iron oxalate solution) and an operating system are necessary for coping with the instability of natural light sources. On the other hand, by concerning the simulated light source instead of using natural sunlight which can eliminate the factor of weather and location dependency, the LED which can generate the light in the near UV-region is an interesting choice since it provides a high rate of photochemical reduction of iron(III) oxalate aqueous solution as confirmed in this study. However, the cost of production will be another important factor that needed to be considered.

Finally, although our proposed iron-making process is studied in the infant stage and has not been performed as a continuous process yet, this study is firmly believed to be a pinpoint of further development of iron-making industries. It also can serve as an idea for other industries which require the development in a greener or more environmental-friendly alternative process.

APPENDIX I

To determine and distinguish the amount of Fe^{3+} and Fe^{2+} in dissolution solution, the colorimetric method (spectraanalysis) was used. The colorimetric method is a simple and selective technique that used for identification and determination the concentrations of the colored compounds in solution. However, the dissolved Fe solution cannot directly measure by this method due to the light sensitive property, therefore, the complexing agent such as 1,10-phenanthroline which can provide the stable complex is necessary.

$$3(phen) + Fe^{2+} \qquad (phen)_3Fe(II)$$
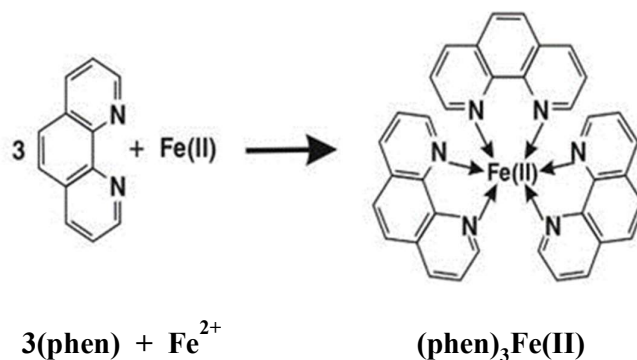
In this study, 1,10-phenanthroline (phen) was used as a complexing agent which can form a specific complex with Fe^{2+} and produce a red colored complex of $Fe(phen)_3^{2+}$ with a maximum absorbance at 510 nm. For the concentration of Fe^{3+}, this method was modified by adding a reducing agent to reduce Fe^{3+} to Fe^{2+} which can form $Fe(phen)_3^{2+}$ complex.

1,10-phenanthroline, NH_4CH_3COO (ammonium acetate) and $NH_2OH.HCl$ (hydroxylamine) were used as the complexing agent, buffer solution and reducing agent, respectively. The Fe (II) standards, Fe of $(NH_4)_2Fe(SO_4)_2 .6H_2O$, were prepared in the range of 0-6 ppm in order to create calibration curve as shown in **Table A1**.

APPENDIX

**Table A1** The preparation of standard curve for determining dissolved Fe.

Reagent (ml)	Concentration (ppm)						
	0	1	2	3	4	5	6
100 ppm Fe(II)	0	1	2	3	4	5	6
5% $NH_2OH.HCl$	4						
0.20% 1,10-phenanthroline	10						
0.50M $NH_4(CH_3COO)$	10						
pH	5-6						

Into seven 100 ml volumetric flasks, pipet 0, 1, 2, 3, 4, 5 and 6 mL portion of standard Fe(II) solution. Then, to each flask, add 4 ml of 5% $NH_2OH.HCl$, 10 ml of 0.20% 1,10-phenanthroline and 10 ml of 0.5M $NH_4(CH_3COO)$. Subsequently, the volume was adjusted to 100 mL using deionized water. The Fe standards were measured absorbance by using a UV-Vis spectrophotometer at 510 nm to obtain standard calibration curve as shown in **Figure A1**. Then, the concentration of dissolved Fe in solutions will be determined by comparing the absorbance at 510 nm of their solution with the standard curve.
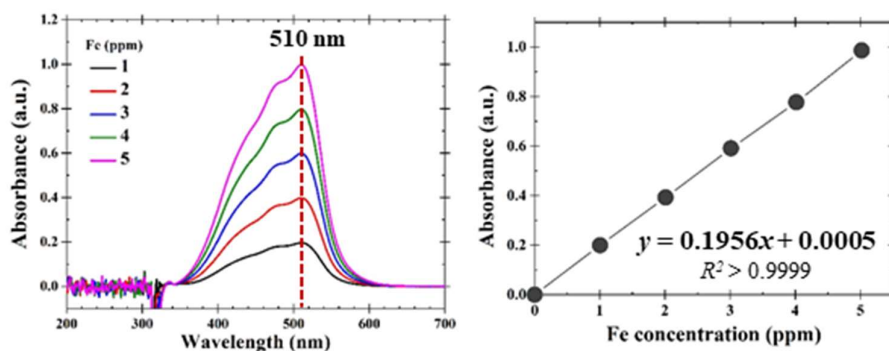
Figure A1. The UV spectra (left) and standard curve of $Fe(phen)_3^{2+}$ complex (right)

The concentrations of dissolved Fe in dissolution samples were determined in the same process as described above, excepted, using 0.015 ml of dissolved Fe solution instead of Fe (II) standard, the procedure is shown in **Figure A2.**

APPENDIX
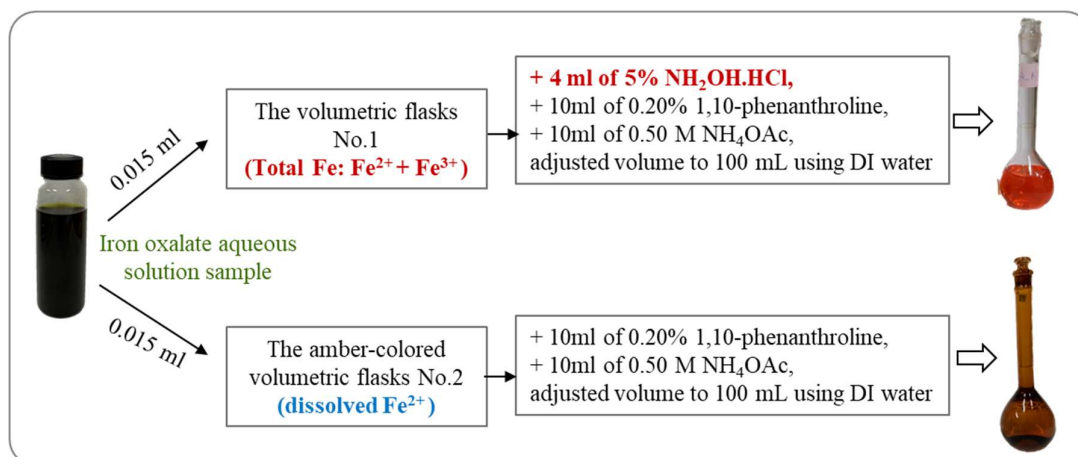
Figure A2. The procedure of determination dissolved Fe using colorimetric method.

For the concentration of dissolved Fe^{2+}, the 4 ml of 5% $NH_2OH.HCl$ was not used. Then, the concentration of dissolved Fe in solutions will be directly determined by comparing the absorbance at 510 nm of their solution with the standard curve producing from Fe standard.

However, in case of dissolved Fe^{3+} concentration, the reducing agent was used to reduce Fe^{3+} to Fe^{2+}, which can form complex with 1,10-phenanthroline and reported as the total iron. Therefore; [dissolved Fe^{3+}] = [dissolved total Fe] - [dissolved Fe^{2+}]

APPENDIX II

Copyright 2020 American Chemical Society